

# Modelling CO<sub>2</sub> weather – why horizontal resolution matters

Anna Agustí-Panareda<sup>1</sup>, Michail Diamantakis<sup>1</sup>, Sébastien Massart<sup>1</sup>, Frédéric Chevallier<sup>2</sup>, Joaquín Muñoz-Sabater<sup>1</sup>, Jérôme Barré<sup>1</sup>, Roger Curcoll<sup>3</sup>, Richard Engelen<sup>1</sup>, Bavo Langerock<sup>4</sup>, Rachel Law<sup>5</sup>, Zoë Loh<sup>5</sup>, Josep Anton Morgui<sup>3</sup>, Mark Parrington<sup>1</sup>, Vincent-Henri Peuch<sup>1</sup>, Michel Ramonet<sup>2</sup>, Coleen Roehl<sup>6</sup>, Alex T. Vermeulen<sup>7</sup>, Thorsten Warneke<sup>8</sup>, and Debra Wunch<sup>9</sup>

<sup>1</sup>European Centre for Medium-range Weather Forecasts, Shinfield Park, Reading, RG2 9AX, United Kingdom

<sup>2</sup>Laboratoire des Sciences du Climat et de l'Environnement, LSCE/IPSL, CEA-CNRS-UVSQ, Université Paris-Saclay, F-91198 Gif-sur-Yvette, France

<sup>3</sup>Environmental Science and Technology Institute, Universitat Autònoma de Barcelona, ICTA-UAB, Bellaterra, Spain

<sup>4</sup>Royal Belgian Institute for Space Aeronomy (BIRA-IASB), Brussels, Belgium

<sup>5</sup>CSIRO Oceans and Atmosphere, PMB 1, Aspendale, Victoria 3195, Australia

<sup>6</sup>California Institute of Technology, Pasadena, California, USA

<sup>7</sup>ICOS ERIC- Carbon Portal, Sölvegatan 12, 22362 Lund, Sweden

<sup>8</sup>University of Bremen, Institute of Environmental Physics, Otto-Hahn-Allee 1, 28359 Bremen, Germany

<sup>9</sup>University of Toronto, Department of Physics, Toronto, Ontario, Canada

**Correspondence:** Anna Agusti-Panareda (Anna.Agusti-Panareda@ecmwf.int)

**Abstract.** Climate change mitigation efforts require information on the current greenhouse gas atmospheric concentrations and their sources and sinks. Carbon dioxide (CO<sub>2</sub>) is the most abundant anthropogenic greenhouse gas. Its variability in the atmosphere is modulated by the synergy between weather and CO<sub>2</sub> surface fluxes, often referred to as CO<sub>2</sub> weather. It is interpreted with the help of global or regional numerical transport models, with horizontal resolutions ranging from a few hundreds of km to a few km. Changes in the model horizontal resolution affect not only atmospheric transport, but also the representation of topography and surface CO<sub>2</sub> fluxes. This paper assesses the impact of horizontal resolution on the simulated atmospheric CO<sub>2</sub> variability with a numerical weather prediction model. The simulations are performed using the Copernicus Atmosphere Monitoring Service (CAMS) CO<sub>2</sub> forecasting system at different resolutions from 9 km to 80 km and are evaluated using in situ atmospheric surface measurements and atmospheric column-mean observations of CO<sub>2</sub>, as well as radiosonde and SYNOP observations of the winds.

The results indicate that both diurnal and day-to-day variability of atmospheric CO<sub>2</sub> are generally better represented at high resolution, as shown by a reduction in the errors in simulated wind and CO<sub>2</sub>. Mountain stations display the largest improvements at high resolution as they directly benefit from the more realistic orography. In addition, the CO<sub>2</sub> spatial gradients are generally improved with increasing resolution for both stations near the surface and those observing the total column, as the overall inter-station error is also reduced in magnitude. However, close to emission hotspots, the high resolution can also lead to a deterioration of the simulation skill, highlighting uncertainties in the high resolution fluxes that are more diffuse at lower resolutions.

We conclude that increasing horizontal resolution matters for modelling CO<sub>2</sub> weather because it has the potential to bring together improvements in the surface representation of both winds and CO<sub>2</sub> fluxes, as well as an expected reduction in numer-

ical errors of transport. Modelling applications like atmospheric inversion systems to estimate surface fluxes will only be able to benefit fully from upgrades in horizontal resolution if the topography, winds and prior flux distribution are also upgraded accordingly. It is clear from the results that an additional increase in resolution might reduce errors even further. However, the horizontal resolution sensitivity tests indicate that the change in the CO<sub>2</sub> and wind modelling error with resolution is not linear, making it difficult to **quantify** the **improvement** beyond the tested resolutions.

Finally, we show that the high resolution simulations are useful for the assessment of the small-scale variability of CO<sub>2</sub> which cannot be represented in coarser resolution models. These representativeness errors need to be considered when assimilating in situ data and high resolution satellite data such as Greenhouse gases Observing Satellite (GOSAT), Orbiting Carbon Observatory-2 (OCO-2), the Chinese Carbon Dioxide Observation Satellite Mission (TanSat) and future missions such as the Geostationary Carbon Observatory (GeoCarb) and the Sentinel satellite constellation for CO<sub>2</sub>. For these reasons, the high resolution CO<sub>2</sub> simulations provided by the CAMS in real-time can be useful to estimate such small-scale variability in real time, as well as providing boundary conditions for regional modelling studies and supporting field experiments.

## 1 Introduction

Over synoptic weather time scales of hours to days and spatial scales less than 1000 km, the assumption that atmospheric CO<sub>2</sub> is well-mixed into a homogeneous background does not hold, as shown by the observed variability at baseline in situ stations (e.g. Halter et al., 1983). CO<sub>2</sub> weather is defined here as the atmospheric CO<sub>2</sub> variability at timescales and spatial scales of weather systems (Parazoo et al., 2011) as depicted in Fig. 1. It reflects a complex combination of anthropogenic and natural CO<sub>2</sub> fluxes near the Earth's surface and transport by weather systems in the atmosphere (Geels et al., 2004; Patra et al., 2008). This synergy of CO<sub>2</sub> fluxes and weather results in intricate atmospheric CO<sub>2</sub> patterns of positive and negative anomalies, collocated with weather variations on top of the well-mixed CO<sub>2</sub> background that varies slowly on timescales of weeks to annual timescales (Keeling et al., 1976).

Modelling the synoptic-scale transport that modulates the CO<sub>2</sub> weather is crucial for interpreting the variability of surface CO<sub>2</sub> concentrations from in situ observations (Law et al., 2010) and column-averaged CO<sub>2</sub> from satellite and ground-based observations (Corbin et al., 2008), and for forecasting CO<sub>2</sub> from 1 to 10 days ahead (Agustí-Panareda et al., 2014; Tang et al., 2018) in order to examine the predictive skill of the models. Tracer transport models use the numerical schemes and meteorological information of Numerical Weather Prediction (NWP) to simulate the tracer variability in the atmosphere. Increasing the horizontal resolution **associated with the grid spacing** of tracer transport models has the benefit of reducing the numerical errors in tracer simulations, leading to convergence of the transport solution from different transport schemes (Prather et al., 2008). NWP models for weather forecast have been doubling the global horizontal resolution approximately every 8 years (Wedi, 2014) in order to improve the forecast skill. But until now, global tracer transport models generally use lower resolution than NWP models, as chemical transport models including chemistry and/or long window data assimilation cannot afford such computational expense.

Observations of atmospheric CO<sub>2</sub> are used in data assimilation systems based on tracer transport models to produce optimal estimates of atmospheric CO<sub>2</sub> concentrations (e.g. Massart et al., 2016) or model parameters and CO<sub>2</sub> fluxes in atmospheric inversion systems (e.g. Rayner et al., 2005; Chevallier et al., 2010). If tracer transport models cannot represent the synoptic variability accurately, then the resulting errors when comparing the tracer from the model with observations will prevent these observations to be used effectively in the data assimilation systems (e.g. Brooks et al., 2012). The model-observation mismatch caused by differences in the resolution of the tracer transport model – including both the resolution of the meteorological fields and the resolution of the fluxes on the model grid – and the resolution of the observation footprint is also known as representativeness error. Failure to properly account for representativeness errors in data assimilation will lead to errors in the optimized parameters, **whether** atmospheric concentrations, model parameters or surface fluxes.

Several studies have investigated the spatial representativeness errors of CO<sub>2</sub> (Miller et al., 2007; van der Molen and Dolman, 2007; Corbin et al., 2008; Tolk et al., 2008) by analysing the CO<sub>2</sub> distribution within model grid cells, based on nested high resolution simulations on limited domains over Europe, North America and South America for certain months or by statistical parameterization of CO<sub>2</sub> covariances based on lower resolution simulations (Alkhaled et al., 2008). The importance of high resolution over complex terrain has also been demonstrated on regional scales, e.g. in Europe (van der Molen and Dolman, 2007; Ahmadov et al., 2009; Pillai et al., 2011) and in North America (Lin et al., 2017; Hedelius et al., 2017) using very high resolution simulations (down to 1 km). However, other studies with coarser global tracer transport models have compared CO<sub>2</sub> simulations with a range of resolutions from a few degrees down to 0.5 degree without finding significant improvements with respect to observations (Lin et al., 2018; Remaud et al., 2018).

The full impact of horizontal resolution on the simulated tracer variability depends on the resolution of transport and emissions/biogenic fluxes (e.g. Vogel et al., 2013) as well as the resolution of the topography and the winds (e.g. Sekiyama et al., 2015) in the model. In this study the full sensitivity of CO<sub>2</sub> synoptic variability to the model horizontal resolution (including all the aspects mentioned above) is investigated by quantifying the change in model error with horizontal resolution at observing stations. Three main questions are addressed:

1. What is the sensitivity of the modelled atmospheric CO<sub>2</sub> variability at diurnal and synoptic timescales to horizontal resolution?
2. How is horizontal resolution affecting the medium-range (1-10 day) forecast error growth of atmospheric CO<sub>2</sub>?
3. What are the typical CO<sub>2</sub> representativeness errors in models with horizontal resolutions of 1 degree x 1 degree, currently considered as high resolution in tracer transport models; and where and when are these representativeness errors largest?

The model simulations use the operational Copernicus Atmosphere Monitoring Service (CAMS) global CO<sub>2</sub> forecasting system (Agustí-Panareda et al., 2014; Massart et al., 2016) which is based on the Integrated Forecasting System (IFS) model of the European Centre for Medium Range Weather Forecasts (ECMWF). They are performed over a range of resolutions currently used operationally in NWP from 9 to 80 km. A detailed description of the simulations, observations and tools used to assess the importance of horizontal resolution for simulating atmospheric CO<sub>2</sub> variability related to weather is presented

in section 2. Section 3 shows the impact of horizontal resolution on the error of simulated horizontal winds (section 3.1) and atmospheric CO<sub>2</sub> (sections 3.2 and 3.3). The results of the sensitivity to horizontal resolution are explained in the context of the small-scale variability in section 3.4. The diagnostics of small-scale variability provide an estimate of the expected representativeness errors for CO<sub>2</sub> simulations with coarser horizontal resolutions. Finally, an example of an urban site is shown in section 3.5, where the impact of horizontal resolution is positive in January and negative in July. The implications of the results for CO<sub>2</sub> forecasting and atmospheric inversion systems are discussed in section 4 with a summary of the main findings on why and where horizontal resolution matters.

## 2 Methodology

### 2.1 Observations

Continuous in situ observations near the surface and column-average observations from the Total Carbon Column Observing Network (TCCON) provide the reference for atmospheric CO<sub>2</sub> variability. Figure 2 shows the spatial distribution of the CO<sub>2</sub> observing stations used in this study. Hourly near-surface CO<sub>2</sub> observations are provided by 51 in situ stations operated by various organizations throughout the period of the simulations: data from 44 stations are taken from the cooperative GLOBALVIEWplus ObsPack (2015) data set, and additional data has been obtained from 3 additional stations from CSIRO in Australia and Antarctica, and 4 stations from the ClimaDat network (Morgu  et al., 2013, 2017) over the Iberian peninsula. The cooperative GLOBALVIEWplus ObsPack (2015) data set is coordinated by NOAA and it comprises data collected by various institutions and laboratories including AEMET, AGH, CSIRO, ECCC, ECN, EMPA, FMI, HMS, LSCE, NCAR, NOAA, JMA, NIWA, SAWS, TU, UBA-SCHAU, UEA, UHEI-IUP and UR (see Tables A1 and A2 for full list of stations with their organisations and associated references). No selection criteria are applied to the stations from the GLOBALVIEWplus ObsPack (2015), CSIRO and ClimaDat datasets, other than availability of hourly data for January and July 2014.

Most stations are on the World Meteorological Organization (WMO) CO<sub>2</sub> scale, although the inter-calibration of standard gases is not critical for this study because the focus is on the relative difference between the high and low resolution simulations to quantify the sensitivity of modelled CO<sub>2</sub> to horizontal resolution in the model. The distribution of the stations is not homogeneous over the globe. However, there is a wide variety of locations that sample synoptic variability on various types of terrain including many coastal, mountain, continental and oceanic sites over different continents on both hemispheres. Wind observations from around 400 radiosondes stations and all the operational 10-m SYNOP stations around the globe are used to evaluate the sensitivity of wind errors to the model horizontal resolution at different atmospheric levels in the troposphere.

Total column observations from 18 TCCON Fourier Transform Spectrometer (FTS) network (Wunch et al., 2011) available in January 2014 and July 2014 – shown as red triangles in Fig. 2 – are also used to evaluate the variability of the column-averaged dry-air mole fraction of CO<sub>2</sub> – hereafter referred to as XCO<sub>2</sub> – (Tab. A3). These TCCON observations are retrieved from direct solar near-infrared spectra ([www.tcon.caltech.edu](http://www.tcon.caltech.edu)) and they provide a ground reference to the GOSAT (Kuze et al., 2009), OCO-2 (Crisp et al., 2017) and TanSat (Yang et al., 2018) satellite observations (e.g. Inoue et al., 2016; Wunch et al., 2017). Total column averages are less sensitive to the uncertainties associated with vertical mixing than the CO<sub>2</sub> abundances

near the surface. However, the temporal coverage of TCCON observations is limited to clear sky and sunny conditions, which means there are generally more gaps in the TCCON data than in near-surface in situ data.

## 2.2 Global atmospheric CO<sub>2</sub> model

The model used in this study is the Integrated Forecasting System (IFS), the same model used in NWP at ECMWF and in the CAMS atmospheric composition analysis and forecasting system to issue 5-day CO<sub>2</sub> and CH<sub>4</sub> forecasts (<https://atmosphere.copernicus.eu/maps/global-carbon-dioxide-forecast>), as well as reactive gases and aerosol forecasts relevant for air quality (Flemming et al., 2015; Morcrette et al., 2009). The IFS model version is CY43r1, the operational weather forecast model at ECMWF from 22 November 2016 to 10 July 2017. A full evaluation of this model cycle can be found in Haiden et al. (2017). The high horizontal resolution is based on a cubic octahedral reduced Gaussian – called hereafter octahedral – grid (Holm et al., 2016). The implementation of the octahedral grid has allowed a substantial increase in the grid point resolution from 16 km to approximately 9 km, without having to increase the spectral resolution of the model (Malardel et al., 2016). The 9 km simulation comprises up to 904 million model grid points, 137 levels and a time step of 7.5 minutes.

The tracer transport is modelled by three different numerical schemes to represent (i) the resolved advection of CO<sub>2</sub> by the winds, and the sub-grid scale (ii) convection and (ii) turbulent mixing processes that need to be parametrized. The tracer advection is computed by a semi-implicit semi-Lagrangian scheme (Temperton et al., 2001; Diamantakis and Magnusson, 2016) which is an unconditionally stable method for the integration of the transport equations and for the fast terms associated with gravity waves. Semi-Lagrangian advection schemes have small dispersion and phase speed errors despite using long timesteps (Staniforth and Côté, 1991). In practice, these properties mean that the timestep is limited only by the local truncation error and not by numerical stability bounds. The semi-Lagrangian advection scheme in the IFS is not mass conserving. Thus, a mass fixer is required to ensure mass conservation at every time step (Agustí-Panareda et al., 2017; Diamantakis and Agustí-Panareda, 2017). The turbulent mixing scheme is described in Beljaars and Viterbo (1998); Koehler et al. (2011); Sandu et al. (2013). The convection scheme is based on Tiedtke (1989) (see Bechtold et al., 2008, 2014, for further details ). Full documentation of the IFS can be found in <https://www.ecmwf.int/en/forecasts/documentation-and-support/changes-ecmwf-model/ifs-documentation>.

The CO<sub>2</sub> surface fluxes from the ocean, biomass burning and anthropogenic emissions are prescribed using inventories or climatologies, while the biogenic fluxes over land are modelled on-line (see Table 1). The anthropogenic CO<sub>2</sub> emissions come from the EDGAR v4.2FT2010 inventory for 2012 (last year with gridded emissions). They are extrapolated in time to the year of the simulation with country trends provided by the EDGAR database (<http://edgar.jrc.ec.europa.eu>). The biogenic CO<sub>2</sub> emissions from land vegetation are modelled with the A-gs photosynthesis scheme and an empirical model to simulate the ecosystem respiration fluxes which are integrated in the CHTESSEL land surface model of the IFS (Boussetta et al., 2013). The fluxes have been evaluated with FLUXNET data and compared to different models (e.g. CASA and ORCHIDEE) showing a comparable performance on synoptic to seasonal scales (Balzarolo et al., 2014). An on-line bias correction scheme (Agustí-Panareda et al., 2016) is applied to the modelled Gross Primary Production (GPP) and ecosystem respiration (Reco) fluxes to

correct for biases in the NEE budget on a time-scale of 10 days compared to a climatology of optimized fluxes (Chevallier et al., 2010). **Figure S1 shows the monthly mean NEE for the highest and lowest resolutions.**

The atmospheric tracer transport and CO<sub>2</sub> biogenic fluxes are two of the largest contributors to the synoptic variability of atmospheric CO<sub>2</sub> globally (Geels et al., 2004; Agustí-Panareda et al., 2014). Thus, the modelling of these two components  
5 on-line in the IFS allows us to investigate the full impact of the resolution coming from the winds, the tracer transport, as well as the fluxes.

### 2.3 Global atmospheric CO<sub>2</sub> simulations

A set of global simulations are performed at several resolutions from 9 km to 80 km (Table 2) to investigate the impact of horizontal resolution on the modelled CO<sub>2</sub> variability at diurnal and synoptic scales. These are the resolutions that are currently  
10 used operationally in global meteorological re-analysis – e.g. ERA-Interim at 80 km (Dee et al., 2011) - widely used in tracer transport models, and the typically higher resolutions of operational weather forecasts models. For instance, the deterministic weather forecast at ECMWF currently runs at 9 km resolution, and it was the global forecasting system with the highest resolution in the world when it was introduced on 8 March 2016 (Holm et al., 2016).

The octahedral grid is used for all simulations, except for the lowest resolution simulation at 80 km which uses a reduced  
15 linear Gaussian grid as in the ERA-Interim and CAMS re-analysis (Inness et al., 2018). The time steps are also dependent on the horizontal resolution and range from 7.5 minutes to 45 minutes. As described in section 2.2, the semi-Implicit semi-Lagrangian method used in the IFS is free from stability restrictions. Thus, the model uses the longest possible timestep that provides the most accurate result for each spatial resolution. This is selected through experimentation and validation, but a rule of thumb is that as the horizontal resolution increases, the timestep decreases to keep the mean Courant–Friedrichs–Lewy (CFL)  
20 number constant. This typically leads to much longer timesteps than Eulerian models for which their timestep is restricted by the typical CFL stability limit (i.e. the maximum CFL number being less than 1).

All the simulation experiments are conducted for a winter and a summer month, in January 2014 and July 2014, as we expect that winter and summer periods will show markedly different variability patterns in CO<sub>2</sub>. Figure 3 shows the configuration of the simulations. A 10-day forecast is performed at 00 UTC each day of the month. The meteorological initial conditions of  
25 each forecast come from the ECMWF operational NWP analysis (Rabier et al., 2000); whereas the atmospheric CO<sub>2</sub> tracer is initialised with the previous 1-day forecast, which means CO<sub>2</sub> is essentially free running, as in Agustí-Panareda et al. (2014). The first initial conditions for CO<sub>2</sub> on 1 January 2014 and 1 July 2014 are extracted from the CAMS CO<sub>2</sub> analysis (Massart et al., 2016). NWP analysis of meteorological fields is one of the main elements determining the quality of the tracer transport (Locatelli et al., 2013; Polavarapu et al., 2016). Keeping the meteorological fields close to the analysis by having a sequence  
30 of 1-day forecasts ensures the tracer transport is as realistic as possible. Therefore, the sequence of 1-day forecasts is used as the standard (cyclic forecast) configuration for the simulations at different resolutions.

The extension to the 10-day forecasts allows us to assess the impact of errors in the meteorological fields – which grow during the forecast – on the CO<sub>2</sub> simulations. There are 10 realisations of CO<sub>2</sub> for each day, one for each forecast lead time (Fig. 3). Each forecast lead time is evaluated separately in order to estimate the error growth during the forecast. For consistency

in the evaluation of the different forecast lead times, the periods from 10 January to 10 February and 10 July to 10 August are used in the validation diagnostics.

The simulations also include an additional CO<sub>2</sub> tracer which is only transported (i.e. does not respond to CO<sub>2</sub> surface fluxes) during the forecast. We refer to this tracer as *NFX*. This tracer is still initialised with the standard CO<sub>2</sub> at the beginning of each forecast. The difference between the *NFX* CO<sub>2</sub> and the standard CO<sub>2</sub> tracers can provide insight on the sensitivity to local flux at different horizontal resolutions. Similarly, the change in the error of the simulation with resolution for both the standard and the *NFX* tracers can be used as an indicator of transport versus local flux influence in the assessment of the impact of horizontal resolution.

## 2.4 Diagnostics for model evaluation

The focus of this paper is on assessing the skill of the model in simulating CO<sub>2</sub> weather with short-term variability over a period of a month. For this purpose, the Root Mean Square Error

$$RMSE = \sqrt{\frac{1}{N} \sum_{i=1}^N (m_i - o_i)^2}, \quad (1)$$

the systematic error or bias

$$\mu = \frac{1}{N} \sum_{i=1}^N (m_i - o_i) \quad (2)$$

and the random error

$$STDE = \sqrt{\frac{1}{N} \sum_{i=1}^N (m_i - o_i - \mu)^2} \quad (3)$$

of the modelled CO<sub>2</sub> dry molar fraction ( $m$ ) are computed with respect to  $N$  hourly observations ( $o$ ) at each observing site. The standard deviation of the site error – also known as inter-station error – is used as an indicator of the spatial variability of the error  $e$  (e.g. RMSE,  $\mu$ ) between the  $M$  observing sites:

$$\sigma_e = \sqrt{\frac{1}{M-1} \sum_{s=1}^M (e_s - \bar{e})^2}, \quad (4)$$

where  $\bar{e}$  is the mean error of all sites. It reflects the skill of the model in representing spatial gradients between the sites. The Pearson's correlation coefficient is also used to assess the skill of the model in simulating the diurnal and synoptic variability at the sites.

The model is sampled in the horizontal by taking the nearest grid point to the station over land. This approach is widely used in model evaluation (Patra et. al, 2008) as it allows assessment of the model directly at grid point scale. At coastal locations, coarse resolution models can find a better fit to observations by sampling the nearest ocean grid point as land grid points tend to overestimate the diurnal cycle (Law et al., 2010). For this reason, the sampling protocol for observations in atmospheric

inversion system move some stations offshore (Gurney et al., 2003). However, coastal sites can have both ocean and land influence which means that they will have contrasting periods sampling baseline air associated with low variability and periods with land and local influences associated with high CO<sub>2</sub> variability (Patra et. al, 2008). In this study we have chosen to sample consistently the nearest land point over land because we are interested in assessing the capabilities of the model to represent  
 5 both baseline and local influences. The temporal sampling is performed with a linear interpolation from the 3-hourly archived model fields to the observation time as in Agustí-Panareda et al. (2014).

At the surface stations, the model is also interpolated to the altitude of the sampling height above the ground level (AGL). This ensures the same model levels are used for the different horizontal resolutions. The model has hybrid coordinates that follow the terrain close to the surface. Selecting the model level at the station height above mean sea level (ASL) would imply  
 10 using different model levels for different resolutions when the orographic height varies between the horizontal resolutions. It would therefore lead to comparisons of CO<sub>2</sub> in the planetary boundary layer and free troposphere at mountain sites where the low resolution model underestimates the orographic height. Lin et al. (2017) tested both approaches at several mountain sites. They found that the sampling at ASL greatly underestimates the amplitude of the diurnal cycle, as the sensitivity to local fluxes is reduced at higher levels above the ground. Since most low resolution models used in atmospheric inversions tend to  
 15 use the model sampling ASL at mountain sites (e.g. Wang et al., 2018), a comparison of the two approaches (AGL and ASL) is provided in the supplement. At the TCCON stations, the model profile is processed with the TCCON averaging kernel and prior, as described in Appendix A of Massart et al. (2016).

Atmospheric CO<sub>2</sub> variability is subject to local or small-scale influences (< 100 km) associated with complex topography, coastal boundaries, local fluxes and mesoscale atmospheric flow (Lin, 2007). Most models used in carbon cycle studies are  
 20 unable to represent such local variability. The resulting representativeness errors reflect the sub-grid scale variability associated with the coarse resolution of the models (e.g. Tolk et al., 2008). At high resolution it is possible to estimate part of this sub-grid scale variability of coarser models. In order to do that, the 9 km simulation is interpolated onto a 0.1x0.1 degree regular lat/lon grid and subsequently it is sampled for each time zone (computed hourly along longitude) at 13:00 +/- 0.5 hours local time. This temporal sampling at 13:00 is consistent with the GOSAT (<http://www.gosat.nies.go.jp/en/> and OCO-2  
 25 (<http://oco.jpl.nasa.gov/mission>) overpass time. Thus, it provides a more relevant estimate of the potential representativeness error for lower resolution inversion systems, which use daytime surface in situ data and satellite data (e.g. Chevallier et al., 2010, 2014). The representativeness error is estimated by computing the standard deviation of the CO<sub>2</sub> dry molar fraction at 0.1 degree resolution within the coarser grid boxes of 1 degree x 1 degree over the whole globe:

$$\sigma_{CO_2} = \sqrt{\frac{1}{n-1} \sum_{j=1}^n (m_j - \bar{m})^2} \quad (5)$$

30 where  $\bar{m} = \frac{1}{n} \sum_{j=1}^n m_j$ ;  $n$  is the number of 0.1 degree resolution grid cells within the coarser grid cell of 1 degree x 1 degree;  $m$  is the CO<sub>2</sub> dry molar fraction at 0.1 degree resolution; and  $\bar{m}$  is the average within the coarser grid cell.

### 3 Results

#### 3.1 Impact of horizontal resolution on winds

The accuracy of the winds is a crucial aspect of the CO<sub>2</sub> transport quality, as winds drive the advection of CO<sub>2</sub> across the resolved gradients in the model. In this section we investigate the benefit of increasing the resolution from 80 km to 9 km on RMSE of the zonal and meridional components of the wind. We investigate the changes in the global wind error with model resolution based on 12-hourly radiosonde observations which measure the horizontal wind components throughout the troposphere. Figure 4 shows there is a consistent and significant RMSE reduction of the vector wind RMSE for the 1-day forecast with resolution. The impact of resolution – quantified here by the difference in RMSE between the 80km and 9km simulations – is largest near the surface at 850 hPa and 1000hPa with a RMSE reduction ranging between 0.2 m/s and 0.6 m/s. This is equivalent to a reduction in RMSE of around 15% near the surface. In the mid and upper troposphere (500 hPa and 200 hPa) there is a consistent but smaller RMSE reduction, ranging between 0.1 m/s and 0.2 m/s.

The RMSE reduction extends throughout the 10-day forecast for the two components of the wind between 1000 and 850 hPa with values around 0.4 m/s and it is consistent in both northern/southern hemispheres and tropics (not shown). The results are also in agreement with the RMSE with respect to 10m wind speed from SYNOP observations with a mean RMSE reduction over the global domain of 0.34 m/s. The reduction of the mean error is smaller than the RMSE (< 0.2 m/s) throughout the troposphere, which means the largest component of the wind error is random.

#### 3.2 Impact of horizontal resolution on CO<sub>2</sub> diurnal and synoptic variability

The sensitivity of the model skill at hourly and daily time scales to the horizontal resolution of the model is assessed with the error of the CO<sub>2</sub> simulations with respect to hourly mean observations. The change in the RMSE with horizontal resolution based on the surface CO<sub>2</sub> and XCO<sub>2</sub> observations (see section 2.1) is shown in Figures 5 to 7.

At the surface there is an overall substantial reduction of RMSE between 80 km and 9 km (i.e. between 1.8 ppm and 3.5 ppm for hourly data) which is clearly not linear (Figs 5a and 5b). The RMSE difference between the 80 km and 40 km simulations or the 40 km and 25 km simulations is not as large as the difference between the higher resolution simulations (e.g. 25 km and the 16 km or the 16 km and the 9 km). This is particularly pronounced for the daily maximum CO<sub>2</sub> occurring usually at nighttime, which is generally controlled by local fluxes and small-scale transport of tracers and therefore it is more sensitive to resolution. The daily maximum values are generally much better captured at 9 km resolution compared to 80 km with a reduction in the RMSE of around 2.5 ppm in January and 6 ppm in July. Indeed, there are large differences between the RMSE of the daily maximum and minimum CO<sub>2</sub> values. As expected, daily minimum values that emerge during daytime have smaller RMSE. This is because during daytime the minimum CO<sub>2</sub> values are influenced by the larger-scale fluxes and tracer transport which are less sensitive to high resolution. The reduction in RMSE of the daily minimum CO<sub>2</sub> is therefore smaller than for the daily maximum, but it is still considerable with an RMSE decrease of around 0.75 ppm from 80 km to 9 km resolutions in both January and July. These differences reflect the ability of the model to represent the diurnal cycle. The 9 km simulation clearly shows a general improvement in the CO<sub>2</sub> diurnal cycle near the surface, with smaller differences in the RMSE of the two daily

extremes. The largest RMSE reduction comes from mountain sites (over 1000 m above mean sea level), ranging between 6 and 10 ppm for hourly CO<sub>2</sub> (Figs 6a and 6b) compared to the lowland sites which can see improvements between 0.5 to 2 ppm for hourly CO<sub>2</sub> RMSE near the surface (Figs 6c and 6d).

In general there is also a notable reduction in the spread of the RMSE at the different sites with resolution, as shown by the  $\sigma$  RMSE values below the panels in Fig 5 and 6. This implies that the spatial gradients between stations are better represented at higher resolutions. The global mean correlation coefficient also increases with resolution from 0.47 to 0.56 in January and 0.51 to 0.59 in July for the hourly CO<sub>2</sub>, with consistently higher correlations for the daily mean, minimum and maximum CO<sub>2</sub> at higher resolution.

As expected, the sensitivity to the strategy of sampling the model level at observing stations is generally small over lowlands but large over mountains, particularly at low resolution (Fig. S2). At mountain sites, the model level at the real station height above mean sea level is predominantly in the free troposphere and therefore it has a small sensitivity to the local fluxes/flow; whereas taking the model level with respect to the model ground generally exhibits larger errors associated with local influences in the boundary layer. The difference between the two sampling strategies on the RMSE and correlation coefficients becomes smaller at high resolution (Fig. S3). This reflects an improvement in the capability of the model to represent the flow and fluxes around complex topography at higher horizontal resolution.

The XCO<sub>2</sub> RMSE at the TCCON sites **during daytime** also displays a general decrease with resolution (Fig. 7), with differences of the order of 0.1 ppm from 80 km to 9 km resolutions and increases in the correlation coefficients ( $r$ ) of up to 0.05. **In boreal summer, the XCO<sub>2</sub> daily minimum has the largest/smallest RMSE/ $r$  because it reflects the uncertainty associated with modelled photosynthesis and negative XCO<sub>2</sub> anomalies; whereas in boreal winter, the XCO<sub>2</sub> daily maximum has the largest RMSE because ecosystem respiration associated with positive XCO<sub>2</sub> anomalies is the dominant process at most TCCON sites.** It is likely that the larger footprint of XCO<sub>2</sub> (Belikov et al., 2017) at most TCCON stations – associated with its sensitivity to large-scale flux patterns – (Keppel-Aleks et al., 2011, 2012) is causing most TCCON sites to be less sensitive to horizontal resolution. However, there is a large variation in RMSE between sites (see  $\sigma$  RMSE in Fig. 7 and Fig S9) which is reduced at high resolution. In particular, the TCCON site at Pasadena (California, USA) located near the anthropogenic emission hotspot of the Los Angeles megacity stands out (Fig. S9). The improvement associated with high resolution at Pasadena is indeed remarkable in January (i.e. approximately 2 ppm RMSE reduction). A more detailed study for Pasadena is provided in section 3.5.

The change of RMSE with resolution is partly associated with the improvement in the transport and also the representation of the local fluxes at higher resolutions. Figure 8 shows that when the fluxes are switched off during the 1-day forecast, there is still an improvement with resolution at most sites, but the magnitude of the error reduction is smaller (see symbols to the right of the dash line). This is very clear for a large number of mountain sites and TCCON sites affected by anthropogenic emissions such as Pasadena (USA) in January and Saga (Japan) in July. However, there are also some sites and months in which the impact of resolution is better without fluxes than with fluxes (e.g. Pasadena in July). This would indicate that in this case the errors in the fluxes are the main cause of the deterioration in RMSE with resolution.

The overall global error statistics of the 9 km and 80 km simulations including the systematic (or bias) error and the standard (or random) error are shown in Table 3. The reduction in RMSE at 9 km is associated with a decrease in the magnitude of the CO<sub>2</sub> biases on average of 1.5 to 2 ppm near the surface and up to 0.2 ppm for XCO<sub>2</sub> and a general reduction in the CO<sub>2</sub> random error of 1 to 1.5 ppm near the surface and 0.1 ppm for XCO<sub>2</sub> (Figs S4 and S5). The biases depend largely on the bias of the CO<sub>2</sub> initial conditions, as well as the biases of the fluxes and tracer transport. What is important in this sensitivity study is that the standard deviation of the bias at each station – i.e. the inter-station bias – is reduced at 9 km with respect to 80 km, as shown by the shaded area in Figs S4 and S5. The largest decrease in the inter-station bias between 80 km 9 km occurs in January, when it is almost halved near the surface. The errors at the individual observing stations are listed in Tables S1, S2, S3, S4.

### 10 3.3 Impact of horizontal resolution on CO<sub>2</sub> forecast error growth

In 10 days the global mean RMSE of CO<sub>2</sub> forecast at the in situ surface stations grows by around 1.4 ppm in January and around 1 ppm in July (Fig. 9). It is worth noting that this error growth is smaller in magnitude than the impact of increasing horizontal resolution from 80 km to 9 km. Namely, the 10-day forecast at 9 km is better than the 1-day forecast at 80 km near the surface. At the TCCON sites the XCO<sub>2</sub> RMSE grows on average between 0.2 and 0.5 ppm in 10 days (Fig. 10). The forecast RMSE growth for near-surface CO<sub>2</sub> and XCO<sub>2</sub> does not appear to be linear, with a slow growth until day-4, and faster increase from day 5 onwards. The CO<sub>2</sub> RMSE growth at 80 km is slightly faster than at 9 km. In summary, the gain in skill from horizontal resolution is maintained throughout the 10-day forecast. Thus, the results suggests that the horizontal resolution has a small but positive impact on the short and medium-range forecast skill for CO<sub>2</sub> and XCO<sub>2</sub>.

As expected, the RMSE in July is largest because of the high uncertainty associated with the modelled biogenic fluxes at synoptic scales which influence the variability at continental sites (Agustí-Panareda et al., 2014). There is also a larger uncertainty in the meteorology driving the tracer transport during summer compared to winter (Haiden et al., 2017). The fact that the forecast RMSE at day-1 is larger than at day-2 in July is associated with a sporadic overestimation of daily maximum CO<sub>2</sub> peaks at sites influenced by strong local fluxes. There are several potential causes of the overestimation (e.g. biogenic fluxes responding to rapid adjustments in meteorology after analysis re-initialisation at 00 UTC or issues with the tracer transport associated with short spin up period), but these are beyond the scope of this study.

The near-surface CO<sub>2</sub> RMSE increase during the forecast appears to come mostly from an increase in random error in January and from both mean and random error in July (Fig. S4); whereas for XCO<sub>2</sub>, both mean and random errors contribute equally to the forecast RMSE growth in January and July (Fig. S5). This is probably linked to the distribution of the stations, as most in situ stations are located in the northern hemisphere; whereas TCCON stations are more equally distributed in both hemispheres, and thus, the mean error at all stations does not show differences between summer and winter conditions.

### 3.4 Impact of horizontal resolution on CO<sub>2</sub> small-scale variability

The sensitivity of the RMSE to resolution is generally associated with regions that are affected by small-scale variability that cannot be properly represented by typical global tracer transport models (Law et al., 2008; Patra et. al, 2008). Figure 11 shows

that the mean small-scale variability, given by the standard deviation within 1 degree x 1 degree grid box, can be as large as 10 ppm near emission hotspots at the surface during daytime. **The representation of the CO<sub>2</sub> small-scale variability at the surface in the 9km-EXP compared to the 80km-EXP is also illustrated in Fig. S6.** Larger values than 10 ppm can be found over most land areas at nighttime (Fig 12). These values are likely to be underestimated, since we expect horizontal gradients to become steeper as the resolution increases, the point sources associated with anthropogenic activities become stronger at the grid cell scale and part of the sub-grid scale flow is resolved.

Coastal sites and mountain sites have a typical sub-grid scale variability of around 5 ppm during daytime. This variability varies from January to July, depending on meteorological conditions (e.g. stagnant or windy conditions) and the magnitude/sign of fluxes (e.g. biogenic activity shifting northwards in northern hemisphere summer). Over land, the patterns of sub-grid scale variability of surface and total column are consistent (Figs 11 and 13), as both are subject to surface heterogeneity in terms of topography and fluxes. However, there is a difference in magnitude because the variability of the total column average is much smaller than the variability at the surface.

XCO<sub>2</sub> has a maximum standard deviation of 1 ppm near surface flux hotspots and typically less than 0.5 ppm in most regions (Fig. 13), which is consistent with other estimates from regional studies (Corbin et al., 2008; Pillai et al., 2010) (**see also Fig. S7 for a visual illustration**). The differences in the small-scale XCO<sub>2</sub> variability between day and night appear to be small. Interestingly, the small-scale variability of XCO<sub>2</sub> is much larger in summer than in winter (both in northern and southern hemispheres). During the growing season, negative CO<sub>2</sub> anomalies associated with plant photosynthesis and positive anomalies associated with ecosystem respiration and anthropogenic emissions combine to create steeper gradients throughout the troposphere – as illustrated in Fig. 1b – that contribute to the enhanced sub-grid scale variability in summer compared to winter. Over the ocean, the small-scale variability of XCO<sub>2</sub> ranges between 0.1 and 0.3 ppm, with lower values in the winter and higher values in the summer. In the northern hemisphere summer, the values over the ocean and over the land are comparable. Whereas near the surface, the mean sub-grid scale variability is an order of magnitude smaller over the ocean than over land. This is because over land the surface fluxes dominate the gradients resulting in the steepest gradients being near the surface; while over the ocean, the transport associated with the weather systems creates steep CO<sub>2</sub> gradients in the free troposphere. Therefore, column averaged CO<sub>2</sub> is much more likely to be influenced by sub-grid scale variability associated with weather systems than by surface CO<sub>2</sub> fluxes over the ocean.

### 3.5 Example of horizontal resolution impact at an urban site

Although the winds, the topography and the spatial heterogeneity of the fluxes are generally better represented at high horizontal resolution, there can still be a deterioration in the RMSE scores at sites where the local influence is strong and the emissions/biogenic fluxes have large errors in the model. In this section we present an example of such a case at the Caltech TCCON site in Pasadena (California, USA, see Tab A3) with XCO<sub>2</sub> under clear-sky and daylight conditions. The variability of the simulated XCO<sub>2</sub> exhibits a substantial improvement with high resolution in winter and an equally considerable deterioration in summer (Fig. 15). Thus, it illustrates some of the challenges associated with urban regions.

Pasadena is located 14 km north-east of the megacity of Los Angeles (LA) with a large local anthropogenic emission influence (Wunch et al., 2009; Newman et al., 2016). The XCO<sub>2</sub> variability in the model is also mainly explained by the local anthropogenic emissions (Figs S10 and S11) producing very large CO<sub>2</sub> enhancements in the Planetary Boundary Layer (PBL) (Fig. S12) and therefore in XCO<sub>2</sub>. The CO<sub>2</sub> budget of the anthropogenic emissions used at 9 km and 80 km is the same. However, the instantaneous values of the emissions per square meter are much higher at 9 km than at 80 km, representing some of the steep gradients and heterogeneous distribution of fossil fuel emissions within the LA basin, with higher emissions in downtown LA and lower emissions in Pasadena (e.g. Feng et al., 2016). At 80 km, Pasadena and downtown LA are in the same model grid box, which means this gradient cannot be represented. In addition to the influence of anthropogenic emissions, the seasonal variation of the winds is very pronounced in Pasadena, with a large contrast in the origin or air masses between winter and summer (Verhulst et al., 2017).

In winter, air masses originate from various directions: from the prevailing westerly and southerly winds bringing and accumulating polluted air from the LA megacity, to northerly and easterly flow characterised by cleaner air with lower CO<sub>2</sub> values from the surrounding desert and mountains (Newman et al., 2016). Persistent low wind conditions lead to a large accumulation of CO<sub>2</sub> in the LA basin as it remains trapped by the mountains. These episodes result in large enhancements in XCO<sub>2</sub> (Hedelius et al., 2017) coinciding with the high CO<sub>2</sub> anomalies over periods of a few days (e.g. 26 to 30 January in Fig. 15a). In those stagnant conditions, the 9 km simulation is in much closer agreement with the observed XCO<sub>2</sub> peaks than 80 km simulation, which overestimates the XCO<sub>2</sub> anomalies. This is because at 80 km resolution there is an effectively uniform emission for the whole LA basin. Note that the CO<sub>2</sub> and XCO<sub>2</sub> small-scale variability around LA appears to be larger in winter than in summer (Figs 11 and 14). Without preserving the sharp gradient in emissions between Pasadena and downtown LA, the CO<sub>2</sub> accumulation is overestimated in Pasadena.

The atmospheric circulation in summer is mainly controlled by the sea-mountain breeze (Lu and Turco, 1994). Daytime advection of anthropogenic CO<sub>2</sub>-rich air from LA city results in XCO<sub>2</sub> peaking in the afternoon before it is vented over the mountains (Newman et al., 2013, 2016). The overestimation in the summer XCO<sub>2</sub> peaks at 9 km is likely reflecting an overestimation of the emissions in downtown LA. The enhancement of CO<sub>2</sub> from anthropogenic emissions is larger at 9 km than at 80 km (Fig. S11). This suggests an overestimation of the hotspot emissions over the LA basin in the temporally-extrapolated EDGAR inventory, which is smoothed and less noticeable at lower resolution. There are many reasons why the anthropogenic emissions used in the model can be overestimated, including the temporal extrapolation based on country-scale scaling factors and the use of annual constant emissions in EDGAR4.2FT2010 instead of seasonally varying emissions (Corbin et al., 2010).

Differences in the sampling location (centre of grid is 3 km and 34 km from station location at 9 km and 80 km respectively), orography (15 m below and 46 m below the station height at 9 km and 80 km respectively) as well as differences in flow and local biogenic fluxes can also play a role in explaining the differences between the simulations at 80 km and 9 km resolutions. The results are consistent with previous studies by Feng et al. (2016) and Hedelius et al. (2017). They found that uncertainties in the fluxes and their high resolution representation in the LA basin are as important as the atmospheric tracer transport in the representation of the CO<sub>2</sub> enhancement and its variability in Pasadena.

This example at Pasadena highlights the importance of horizontal resolution to represent local gradients of CO<sub>2</sub> fluxes in order to reduce the atmospheric CO<sub>2</sub> representativeness error. It emphasizes that the impact of increasing horizontal resolution is not only to reduce the error of atmospheric CO<sub>2</sub> simulations, but to enhance the sensitivity of the modelled atmospheric CO<sub>2</sub> variability to the CO<sub>2</sub> fluxes in urban regions characterised by emission hotspots. Therefore horizontal resolution is crucial for atmospheric inversion systems that aim to estimate anthropogenic emissions.

#### 4 Discussion and conclusions

This paper addresses the importance of horizontal resolution in the representation of CO<sub>2</sub> variability at diurnal and synoptic scales, referred to here as CO<sub>2</sub> weather. The CO<sub>2</sub> simulations performed with the ECMWF IFS model allow to quantify the combined impact of horizontal resolution associated with (i) the on-line modelling of the winds, (ii) the numerical tracer transport model and (iii) the spatial/temporal distribution of CO<sub>2</sub> fluxes over land. The assessment is done by comparing the model errors at various horizontal resolutions with respect to a wide range of observations with hourly resolution and distributed around the globe. The horizontal resolution of the model ranges from 9 km – as in current operational high resolution weather and CO<sub>2</sub> forecasts at ECMWF – and 80 km, which corresponds to the ERA-Interim re-analysis resolution, widely used by many off-line tracer transport models. The conclusions to the three main questions addressed in the paper are summarised below:

##### 1. What is the sensitivity of the modelled atmospheric CO<sub>2</sub> variability at diurnal and synoptic timescales to horizontal resolution?

The high horizontal resolution of 9 km leads to a general improvement in the simulated variability of hourly near-surface and column-averaged atmospheric CO<sub>2</sub> compared to the resolution of 80 km. This is shown by a reduction in the mean RMSE of around 1.8 ppm in winter and 3.5 ppm in summer (equivalent to 33% error reduction) and 0.1 ppm (i.e. around 10% error reduction) at in situ and TCCON sites respectively, which is associated with a reduction of both the mean and random errors in the model. The inter-station variability is also generally improved in the 9 km simulation for near-surface and column-averaged CO<sub>2</sub> in January and July, with the standard deviation of station biases reduced up to 50% compared to the 80 km simulation in January for near surface CO<sub>2</sub>.

Column-averaged CO<sub>2</sub> is not as sensitive to horizontal resolution as near-surface CO<sub>2</sub> because it has a larger footprint or area of flux influence, except for sites like Pasadena which are close to CO<sub>2</sub> emission hotspots. Similarly, minimum daily values of atmospheric CO<sub>2</sub> are less sensitive to the horizontal resolution than maximum daily values because their footprint tends to be larger in size.

This study also shows that the RMSE reduction of error with horizontal resolution is not linear. This implies that results from sensitivity studies exploring the impact of resolution based on coarse simulations which show small sensitivity to horizontal resolution cannot be extrapolated to higher horizontal resolutions. These results are consistent with the findings of the Lin et al. (2017) study based on wider range of model resolutions from ~ 100 km down to 1 km and

observations at three mountain sites. The reduction in model error associated with the increase of horizontal resolution to 9 km emanates from four different well-known and connected aspects, namely:

- (a) Better accuracy of the horizontal winds. The strength of the winds determines the observed CO<sub>2</sub> variability – i.e. the detected CO<sub>2</sub> enhancement – close to emission hotspots like in urban regions (Newman et al., 2013; Xueref-Remy et al., 2018). Therefore, the error in the wind will affect the value of the enhanced CO<sub>2</sub> as much as the error in the fluxes. In this context, for example, a wind speed error reduction of 0.5 ms<sup>-1</sup> – as shown in section 3.1 – across a gradient of 10 ppm/1 degree – typical of urban areas as shown in section 3.4 – throughout a 6-hour period can result in a CO<sub>2</sub> error reduction of around 1 ppm. Uncertainty in the winds has been shown to be one of the largest contributors to the uncertainty in the estimated fluxes over urban areas (e.g. Hedelius et al., 2017).
- (b) An overall reduction of the numerical error associated with lower spatial and temporal truncation errors, leading to a reduction in tracer advection errors (Prather et al., 2008).
- (c) A general improvement in the horizontal and vertical sampling at the station locations in the model associated with a more realistic representation of orography and coastal boundaries.
- (d) More realistic representation of CO<sub>2</sub> flux distribution at the surface. High resolution gives an increased capability to represent small-scale sharp gradients associated with complex topographical boundaries at coastal and mountainous terrain sites, as well as the presence of strong local surface fluxes of CO<sub>2</sub> such as anthropogenic emission hotspots.

## 2. How is the horizontal resolution affecting the forecast error growth of atmospheric CO<sub>2</sub>?

The horizontal resolution has a consistent positive impact on the error reduction at all forecast lead times, from day 1 to day 10, implying a long-lived improvement in the prediction skill. The RMSE growth is small from days 1 to 4, namely less than 0.5 ppm near the surface CO<sub>2</sub> and less than 0.05 ppm for XCO<sub>2</sub>. Over the 10 days there is an increase in RMSE of 1 to 1.5 ppm at the surface and 0.1 to 0.5 ppm for the total column. This error growth is not linear. For example, in July the error of the 1-day forecast is worse than the 2-day forecast, with a slower error increase during the 2 to 4 day forecast and a generally faster error increase from day 5 to day 10 in the forecast. This incoherent change in the error evolution at the beginning of the forecast is likely linked to the strong influence of the biogenic surface fluxes, which respond very fast to changes in temperature, moisture and radiation forcing in the model. Inconsistencies between the analysis as initial condition and the model forecast can cause spin up adjustments which may lead to a degradation of the 1-day forecast.

Generally, the improvement of forecast skill with increased horizontal resolution is most pronounced in January, when at 9 km resolution the skill of the 10-day forecast is better or equal to the accuracy of the 1-day forecast at 80 km both near the surface and for the column average CO<sub>2</sub>. It is likely that the skill of the 10-day forecast to represent variability of CO<sub>2</sub> during summer conditions is hampered by the growing errors in the surface biogenic fluxes during the forecast, as they can be an important contributor to synoptic variability in the summer (Agustí-Panareda et al., 2014).

### 3. Where and when are the typical representativeness errors associated with unresolved small-scale variability largest?

During daytime, the CO<sub>2</sub> small-scale variability of the 9 km-resolution forecast ranges from 1 ppm to 10 ppm at the surface and an order of magnitude smaller (0.1 ppm to 1 ppm) for the total column average. It points to the areas associated with small-scale gradients where horizontal resolution matters: coastal boundaries and mountain regions have typical values of 5 ppm/degree and CO<sub>2</sub> flux hotspots have the highest variability of up to 10 ppm/degree. During nighttime, the small-scale variability tends to be larger than 10 ppm over most areas over near the surface; whereas that of column-average CO<sub>2</sub> shows small differences between day and night.

The high horizontal resolution gives us an insight on the areas with high sensitivity to uncertainty associated with both local tracer transport and fluxes. It is in these areas where improvements in the tracer transport and increased understanding of the heterogeneity and complexity of the surface will be crucial in the future model developments. Since these areas are close to emission hotspots, it is clear that in order to monitor CO<sub>2</sub> emissions, particularly from cities and power stations such as in the new Carbon Human Emission project ([www.che-project.eu](http://www.che-project.eu)), it is paramount to invest in high horizontal resolution models.

Interesting differences are found between surface and column-averaged variability. Near the surface the variability is most pronounced close to emission hotspots and complex terrain. For column-averaged CO<sub>2</sub> the sub-grid scale variability is also substantial over the ocean downstream from emissions. This emphasizes the importance of the transport influence on XCO<sub>2</sub> variability. Small-scale variability is also found to be more pronounced in summer than in winter, as biogenic CO<sub>2</sub> fluxes of opposite sign in summer enhance the CO<sub>2</sub> gradients in the atmosphere.

In summary, this paper has shown that model simulations using the CAMS CO<sub>2</sub> forecasting system at 9 km resolution can provide a more accurate representation of tracer transport and the local influences of surface fluxes than at lower resolutions ranging from 80 km to 16 km, resulting in an overall better representation of the atmospheric CO<sub>2</sub> variability at diurnal and synoptic time scales. However, at higher horizontal resolution there is also higher sensitivity of atmospheric CO<sub>2</sub> to CO<sub>2</sub> flux errors, as emissions and biogenic flux hotspots are not diffused over large areas like in lower resolution models. Thus, higher resolution models also risk the deterioration in the forecast RMSE, e.g. near emission hotspots associated with larger errors. With the enhancement of the model uncertainty at high resolution, the prospect of further increasing the horizontal resolution needs to be carefully balanced with improvements in the most uncertain model processes.

The impact of horizontal resolution on the accuracy of the winds highlights that errors in the wind need to be considered as an important source of uncertainty both in the atmospheric CO<sub>2</sub> analysis/forecast as well as in the inversion systems (Polavarapu et al., 2016). The findings in this study also suggest that increasing horizontal resolution up to kilometric scales in atmospheric data assimilation and inversion systems would allow the use of more in situ and high resolution satellite observations close to strong sources/sinks and over complex terrain. Lin et al. (2017) found that a **minimum** horizontal resolution of 4 km is required to simulate a realistic diurnal cycle of CO<sub>2</sub> at mountain sites.

Currently, the precision of XCO<sub>2</sub> from satellite observations is around 1.0 to 1.5 ppm for ACOS-GOSAT data (O'Dell et al., 2012) and OCO-2 data (Wunch et al., 2017). However, if tracer transport models cannot represent their variability accurately in space and time, all the efforts to reduce the errors from the satellite retrievals of CO<sub>2</sub> will not be fruitful in their attempt to reduce the uncertainty in the estimation of surface fluxes. This is because relatively small differences in atmospheric mixing ratios are associated with significant differences in surface fluxes (Houweling et al., 2010; Ott et al., 2015). The benefits of high resolution in inversion systems will also need to be balanced with the costs of running a model at such high resolution.

Finally, the CAMS high resolution forecast running currently at 9 km resolution can provide benchmarks for other simulations using coarser grids or off-line meteorology (Yu et al., 2018). Both CAMS analysis and high resolution forecasts are freely available to users (<https://atmosphere.copernicus.eu>). Potential applications include the estimation of representativeness errors and data selection screening of observations from satellites and in situ stations in data assimilation systems, spatial collocation of XCO<sub>2</sub> from satellite and TCCON data for validation purposes (e.g. Guerlet et al., 2013) or as boundary conditions for high resolution simulations and/or inversions at regional scales.

*Data availability.* The data is accessible by contacting the corresponding author (Anna.Agusti-Panareda@ecmwf.int).

**Table 1.** Datasets and models of CO<sub>2</sub> fluxes used in simulations listed in Tab. 2.

<b>Flux type</b>	<b>Source</b>	<b>Temporal resolution</b>	<b>Resolution (lat x lon ) [degrees<sup>2</sup>]</b>	<b>Reference</b>
Anthropogenic	EDGARv4.2FT2010	Annual mean	0.1x0.1	Olivier and Janssens-Maenhout (2015)
Biomass burning	GFAS	Daily mean	0.1x0.1	Kaiser et al. (2012)
Ocean	Takahashi climatology	Monthly mean	4.0x5.0	Takahashi et al. (2009)
NEE	CHTESSEL	Adapted to model time step	Adapted to model resolution	Boussetta et al. (2013), Agustí-Panareda et al. (2016)

**Table 2.** List of simulations with different resolutions given by different model grids. All simulations use 137 vertical model levels. All the experiments have been performed in January and July 2014 using the same CO<sub>2</sub> surface fluxes (see Table 1).

<b>Experiment</b>	<b>Model resolution</b>	<b>Model grid</b>	<b>Model time step</b>
9km-EXP	9 km	Tco1279	7.5 min
16km-EXP	16 km	Tco639	12 min
25km-EXP	25 km	Tco399	15 min
40km-EXP	40 km	Tco255	20 min
80km-EXP	80 km	Tl255	45 min

**Table 3.** Surface CO<sub>2</sub> and XCO<sub>2</sub> mean statistics for bias, standard error and RMSE of all stations and the standard deviation of inter-station statistics (in brackets and bold phase) from the highest and lowest resolution simulations, i.e. 9km-EXP and 80km-EXP respectively. All the SFC CO<sub>2</sub> stations used in January and July are listed in Tabs S1 and S2; the TCCON stations used in the XCO<sub>2</sub> statistics are listed in Tabs S3 and S4.

Data	Period	Temporal Resolution	Bias		STDerror		RMSE	
			9km-EXP	80km-EXP	9km-EXP	80km-EXP	9km-EXP	80km-EXP
SFC CO <sub>2</sub>	January	Hourly mean	-0.09 ( <b>2.25</b> )	1.73 ( <b>4.70</b> )	2.70 ( <b>2.25</b> )	3.78 ( <b>3.28</b> )	3.21 ( <b>2.66</b> )	4.96 ( <b>5.04</b> )
		Daily mean	-0.06 ( <b>2.35</b> )	1.76 ( <b>4.71</b> )	1.76 ( <b>1.43</b> )	2.59 ( <b>2.21</b> )	2.43 ( <b>2.17</b> )	4.08 ( <b>4.48</b> )
		Daily min	-0.30 ( <b>1.48</b> )	0.62 ( <b>2.44</b> )	1.41 ( <b>1.09</b> )	1.82 ( <b>1.38</b> )	1.87 ( <b>1.39</b> )	2.59 ( <b>2.18</b> )
		Daily max	0.02 ( <b>4.43</b> )	2.66 ( <b>7.82</b> )	3.68 ( <b>4.00</b> )	4.73 ( <b>4.56</b> )	4.77 ( <b>5.12</b> )	7.12 ( <b>7.76</b> )
SFC CO <sub>2</sub>	July	Hourly mean	0.96 ( <b>5.76</b> )	2.67 ( <b>9.64</b> )	6.70 ( <b>6.94</b> )	9.64 ( <b>11.93</b> )	7.90 ( <b>8.02</b> )	11.56 ( <b>14.18</b> )
		Daily mean	1.14 ( <b>6.55</b> )	2.84 ( <b>9.80</b> )	4.08 ( <b>5.46</b> )	5.52 ( <b>8.30</b> )	5.91 ( <b>7.44</b> )	8.55 ( <b>11.38</b> )
		Daly min	1.48 ( <b>4.17</b> )	0.86 ( <b>4.82</b> )	3.70 ( <b>4.40</b> )	4.11 ( <b>3.74</b> )	4.87 ( <b>5.36</b> )	5.59 ( <b>4.83</b> )
		Daily max	-0.44 ( <b>14.09</b> )	5.07 ( <b>23.05</b> )	9.10 ( <b>11.91</b> )	12.20 ( <b>19.57</b> )	13.22 ( <b>15.71</b> )	19.63 ( <b>26.44</b> )
XCO <sub>2</sub>	January	Hourly mean	-0.49 ( <b>0.74</b> )	-0.38 ( <b>0.92</b> )	0.58 ( <b>0.26</b> )	0.69 ( <b>0.54</b> )	1.02 ( <b>0.37</b> )	1.12 ( <b>0.68</b> )
		Daily mean	-0.51 ( <b>0.77</b> )	-0.38 ( <b>0.99</b> )	0.47 ( <b>0.23</b> )	0.58 ( <b>0.48</b> )	0.97 ( <b>0.40</b> )	1.09 ( <b>0.68</b> )
		Daily min	0.60 ( <b>1.09</b> )	0.75 ( <b>1.18</b> )	0.92 ( <b>0.51</b> )	1.03 ( <b>0.60</b> )	1.36 ( <b>0.87</b> )	1.53 ( <b>1.0</b> )
		Daily max	-1.60 ( <b>1.01</b> )	-1.49 ( <b>1.23</b> )	1.00 ( <b>0.77</b> )	1.13 ( <b>0.91</b> )	1.99 ( <b>1.1</b> )	2.11 ( <b>1.15</b> )
XCO <sub>2</sub>	July	Hourly mean	1.01 ( <b>0.74</b> )	1.04 ( <b>0.92</b> )	0.71 ( <b>0.32</b> )	0.74 ( <b>0.29</b> )	1.28 ( <b>0.57</b> )	1.35 ( <b>0.63</b> )
		Daily mean	0.99 ( <b>0.77</b> )	1.03 ( <b>0.99</b> )	0.56 ( <b>0.28</b> )	0.59 ( <b>0.27</b> )	1.18 ( <b>0.56</b> )	1.25 ( <b>0.61</b> )
		Daily min	2.09 ( <b>1.09</b> )	2.18 ( <b>1.18</b> )	1.05 ( <b>0.67</b> )	1.07 ( <b>0.69</b> )	2.37 ( <b>1.00</b> )	2.46 ( <b>1.06</b> )
		Daily max	-0.01 ( <b>1.01</b> )	-0.07 ( <b>1.23</b> )	0.92 ( <b>0.48</b> )	0.87 ( <b>0.45</b> )	1.21 ( <b>0.56</b> )	1.15 ( <b>0.46</b> )

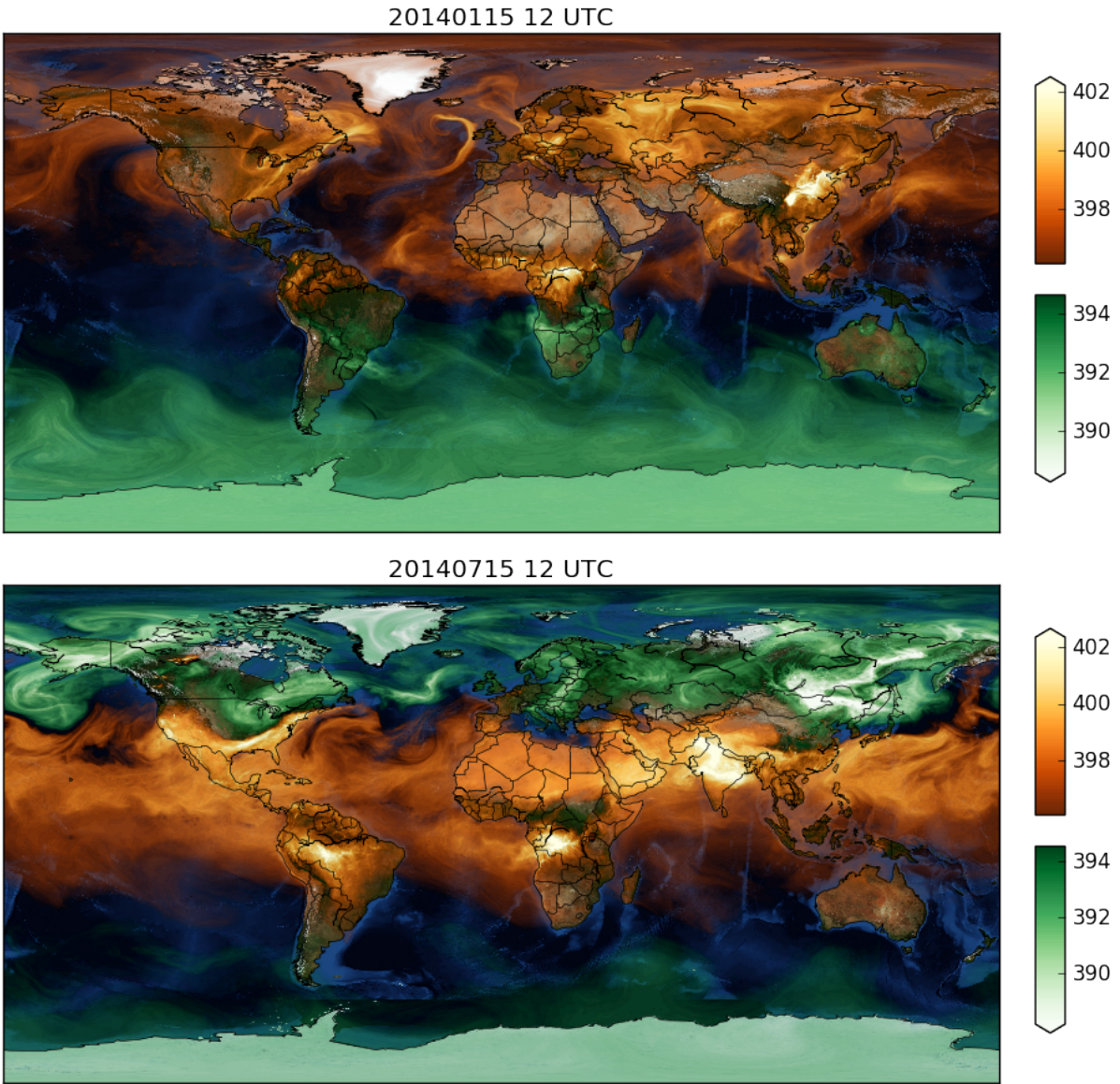


**Figure 1.** Snapshots of averaged-column CO<sub>2</sub> (XCO<sub>2</sub>) [ppm] above (in reds) and below (in greens) the global mean on 15 January (upper panel) and 15 July (lower panel) at 12 UTC from the Copernicus Atmosphere Monitoring Service global CO<sub>2</sub> forecast **at high horizontal resolution (~ 9 km).**

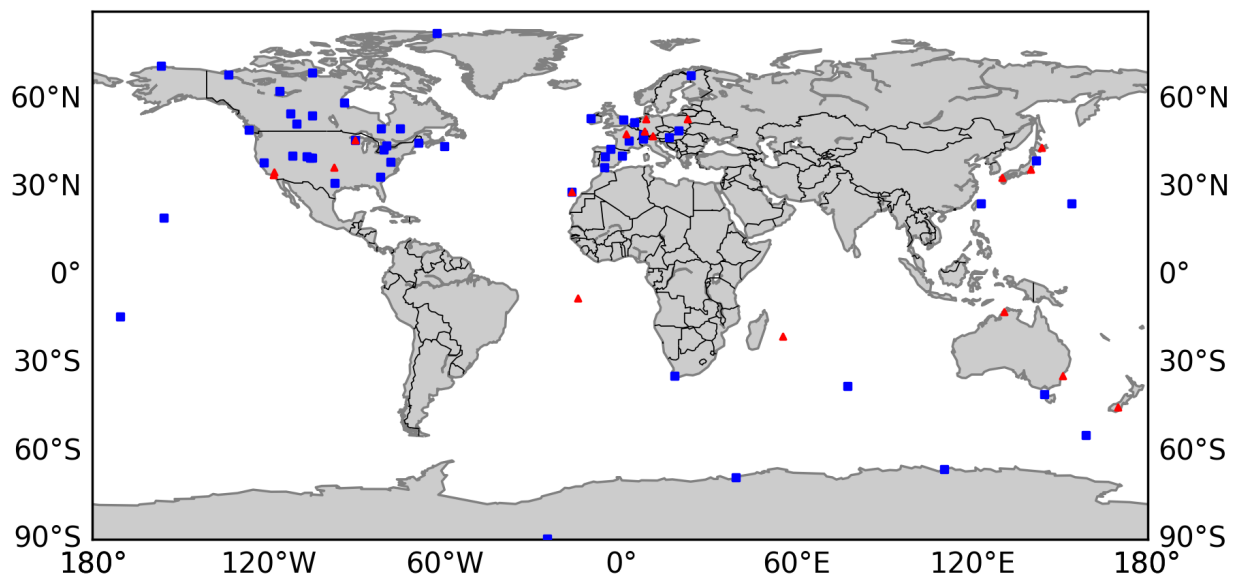


**Figure 2.** Map of in situ (blue squares) and TCCON (red triangles) stations. Detailed information on each station is provided in Tabs. A1 and A3.

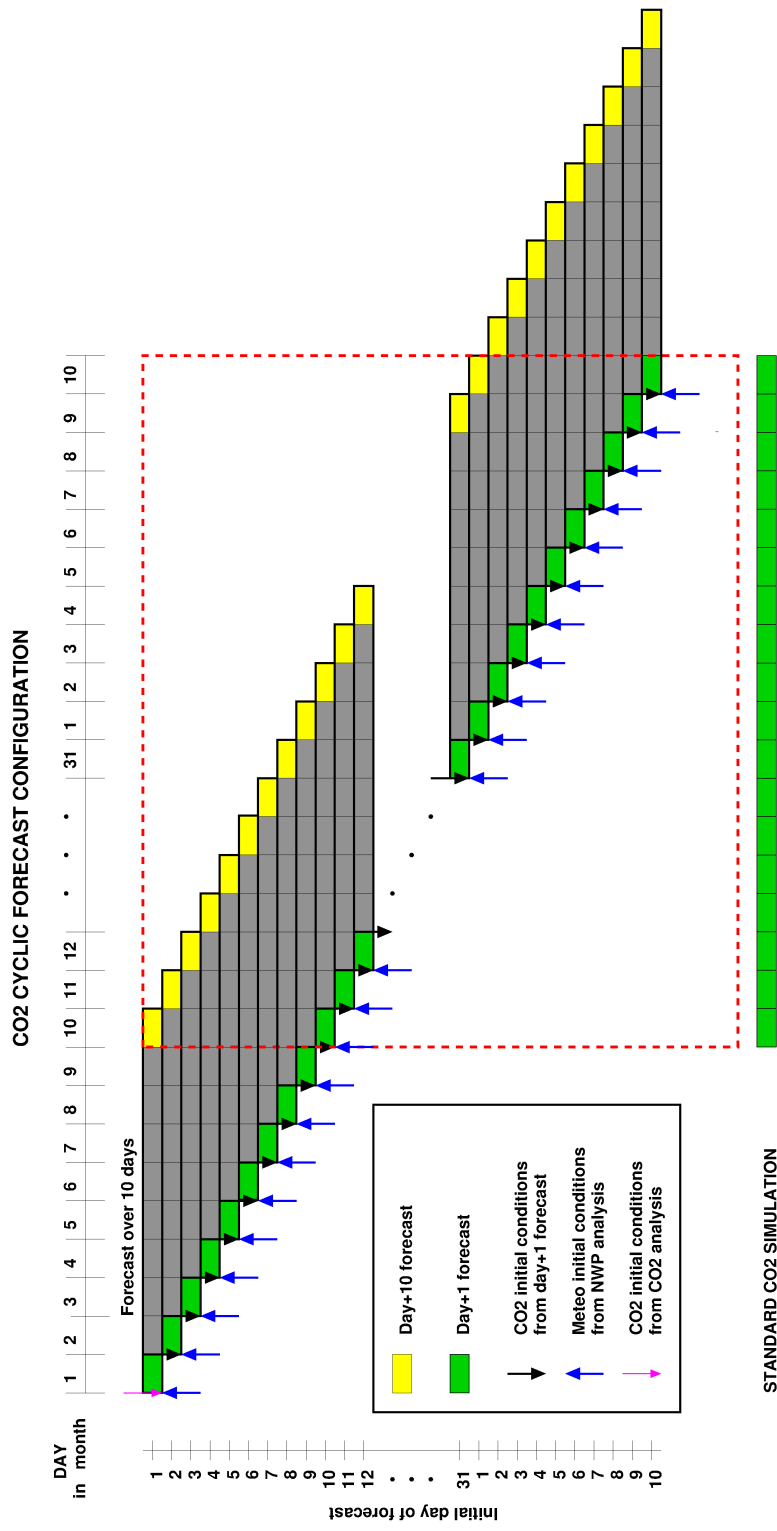


**Figure 3.** Schematic of CO<sub>2</sub> simulations with cyclic forecast configuration with 10-day forecasts initialised every day from 1st of the month to the 10th day of the following month. Initial conditions are depicted by arrows (see legend) and period of evaluation in which several forecast lead times can be compared is delimited by the red dashed line. The standard CO<sub>2</sub> simulations are composed by a series of 1-day forecasts as shown by the green rectangles.

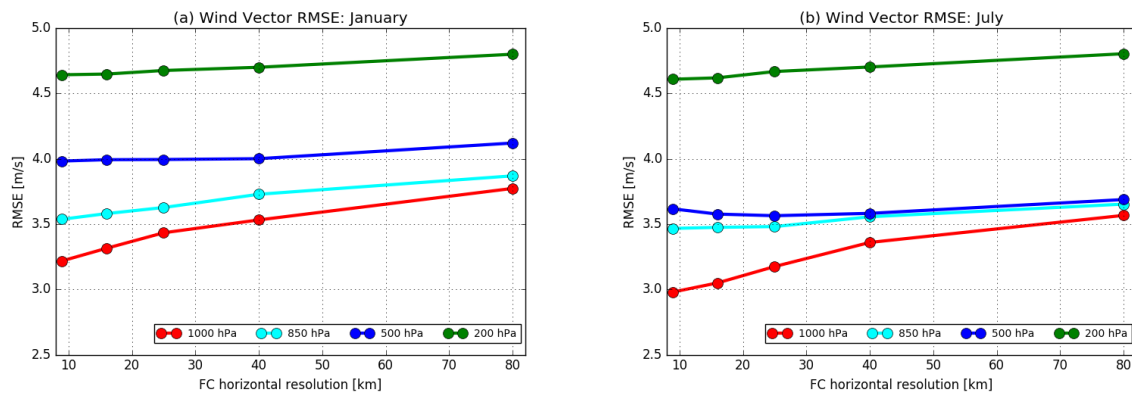


**Figure 4.** Mean RMSE of vector wind [m/s] at different model resolutions in (a) January and in (b) July for around 400 radiosonde stations over the globe. Different colours represent different pressure levels (see legend). All the model simulations are based on the standard 1-day forecast configuration shown in Fig. 3. **Note that the number of data at the 1000-hPa level might be slightly smaller than at the other pressure levels, as the observations at 1000 hPa are not available when the surface pressure is lower than 1000 hPa.**

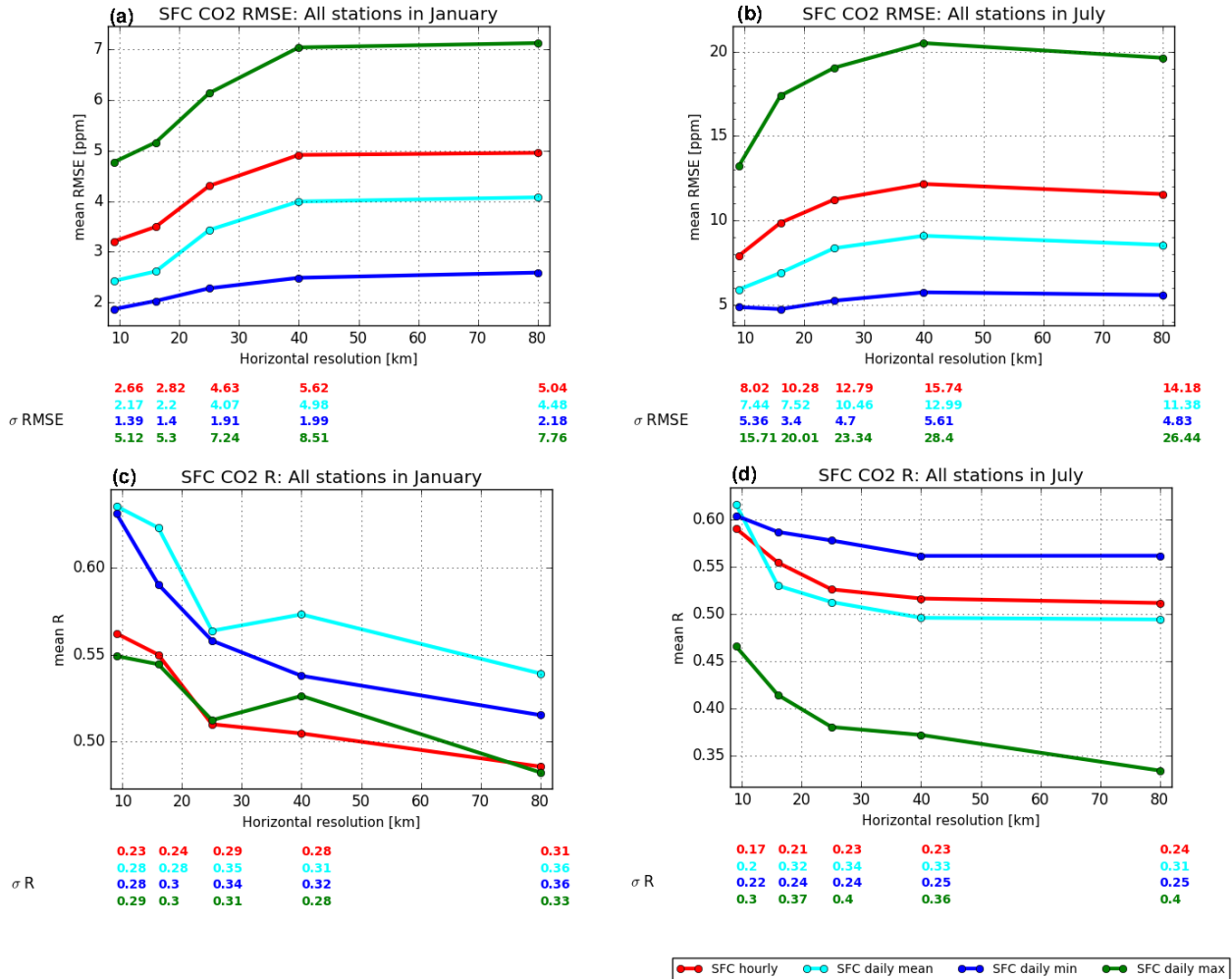


**Figure 5.** Mean RMSE of near-surface CO<sub>2</sub> [ppm] (a,b) and Pearson's correlation coefficient R (c,d) at different model resolutions in January (left panels) and July (right panels) for all 51 stations (see Tab. A1). The standard deviation of the plotted variable from each station is shown by the numbers below the horizontal resolution for each temporal resolution (hourly, daily mean, daily min and daily max). All the model simulations are based on the 1-day forecast. Note that different scales are used in each panel.

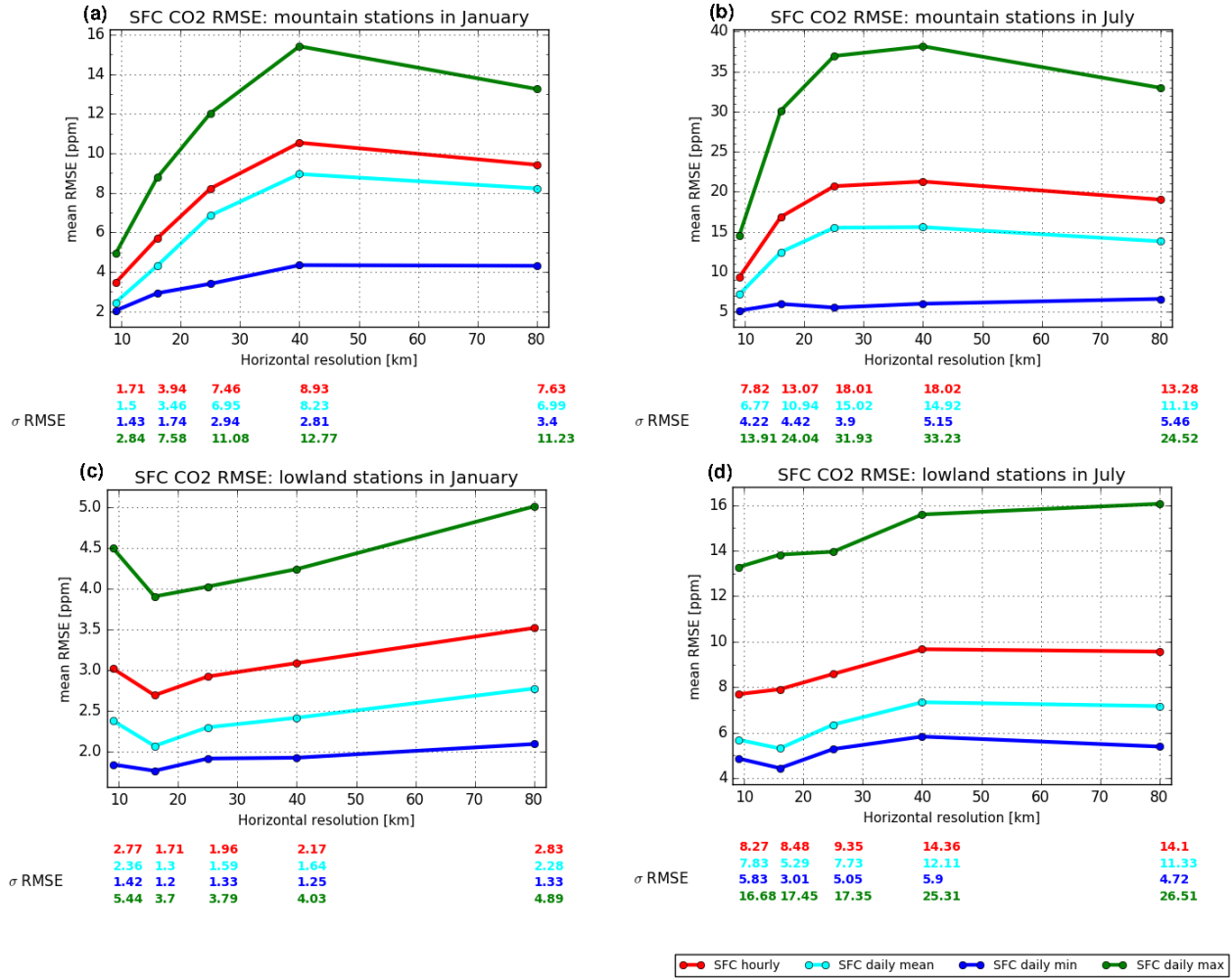


**Figure 6.** Mean RMSE of near-surface CO<sub>2</sub> [ppm] at different model resolutions in January (left panels) and July (right panels) for (a,b) 37 lowland stations (below 1000 m above sea level) (c,d) 12 mountain stations (1000 m above sea level and higher, excluding bao and spo, as listed in Tab. A1). The standard deviation of the plotted variable from each station is shown by the numbers below the horizontal resolution for each temporal resolution (hourly, daily mean, daily min and daily max). All the model simulations are based on the 1-day forecast. Note that different scales are used in each panel.

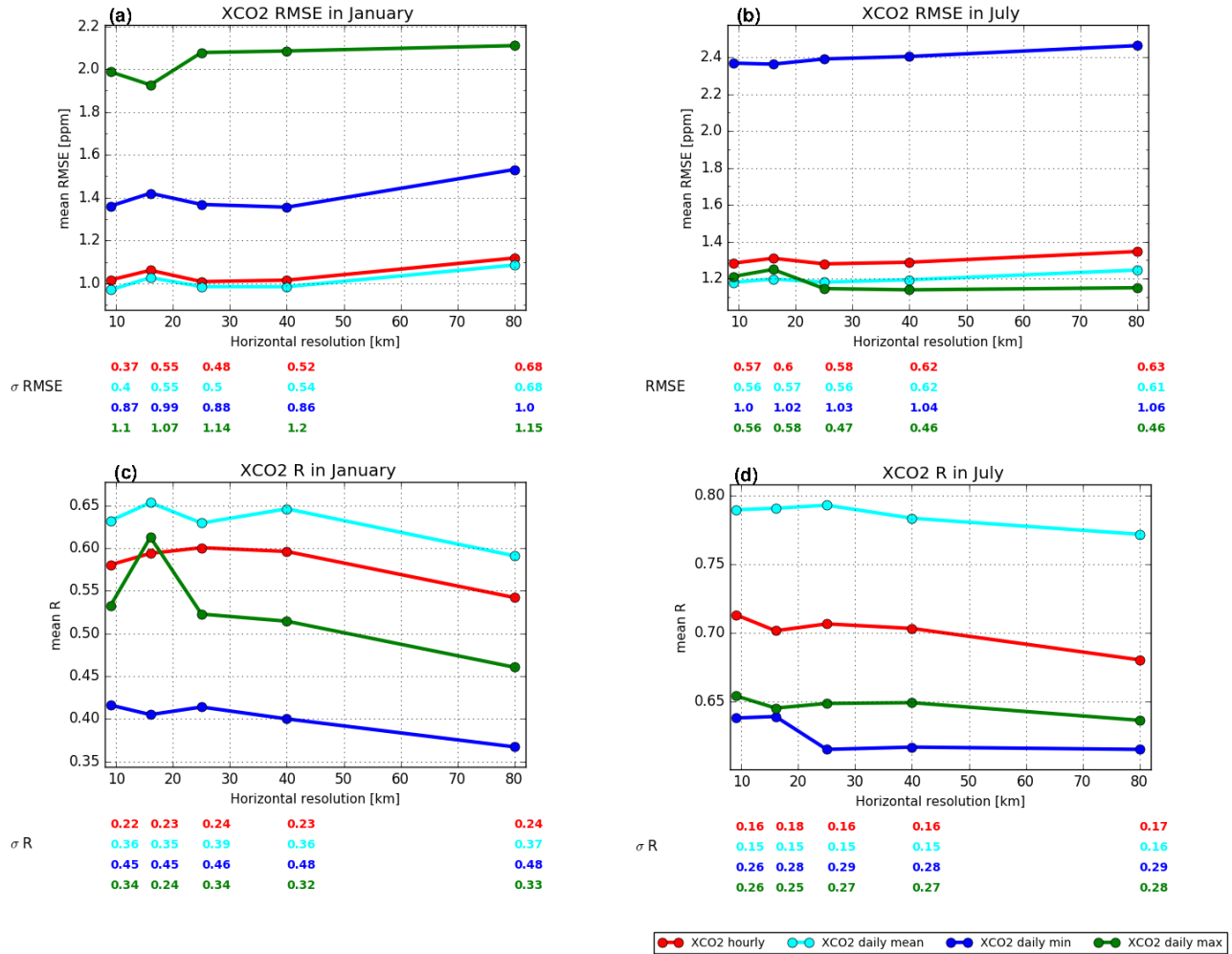


**Figure 7.** Mean RMSE of XCO<sub>2</sub> [ppm] and Pearson's correlation coefficient R with respect to observations from 18 TCCON stations (see Tab. A3) at different model resolutions in (a) January and (b) July. The standard deviation of the plotted variable from each station is shown by the numbers below the horizontal resolution for each temporal resolution (hourly, daily mean, daily min and daily max). All the model simulations are based on the 1-day forecast. Note that different scales are used in each panel.

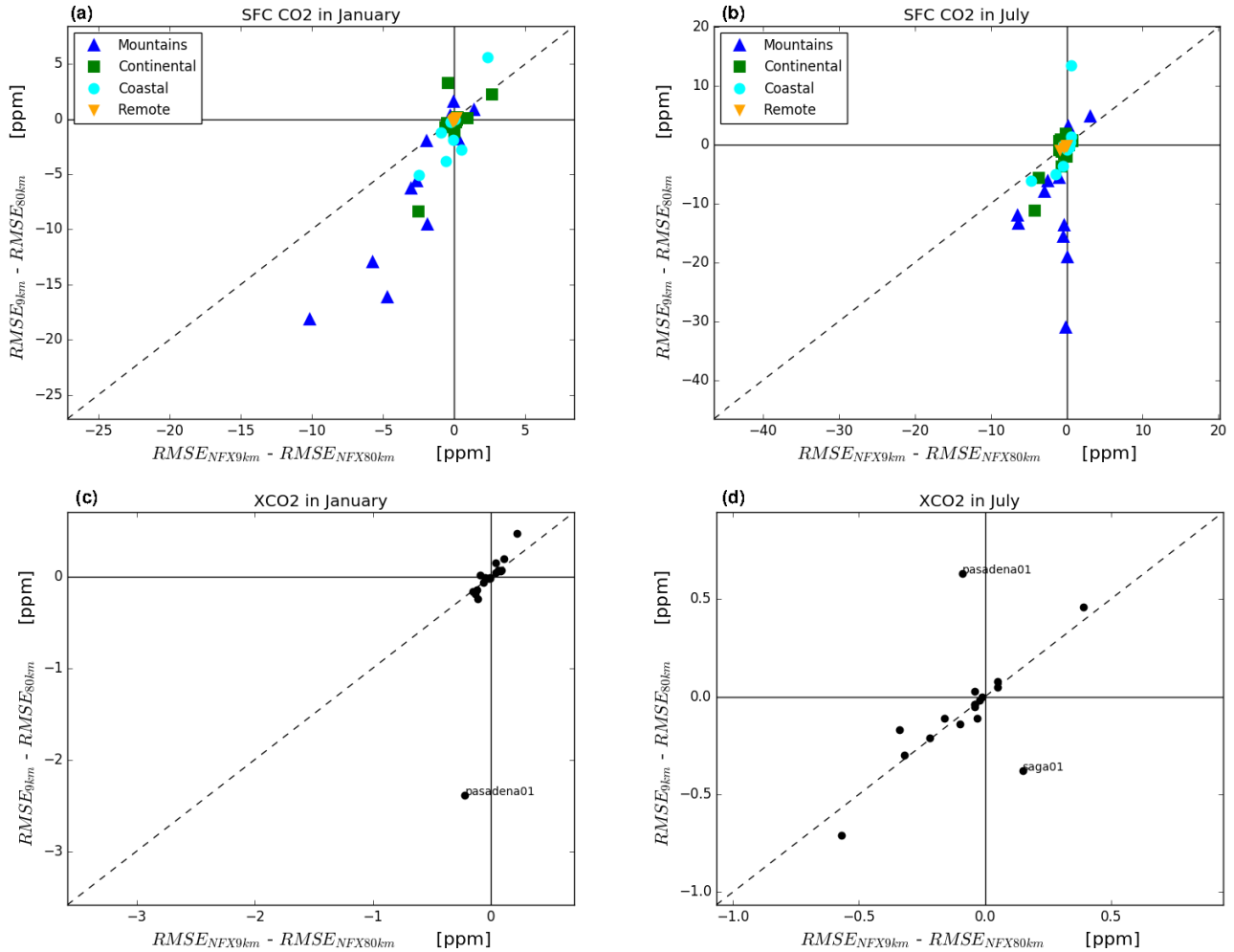


**Figure 8.** Sensitivity of horizontal resolution impact to surface CO<sub>2</sub> fluxes at (a,b) surface stations and (c,d) TCCON stations in January and July, as shown by the difference in RMSE between different CO<sub>2</sub> tracer, i.e. the standard tracer ( $RMSE_{9km} - RMSE_{80km}$ ) and the CO<sub>2</sub> tracer with just transport ( $RMSE_{NFX_{9km}} - RMSE_{NFX_{80km}}$ ) in y-axis and x-axis respectively. The symbols that are close to the dash line correspond to stations that have a small sensitivity to local fluxes; while at the stations associated with symbols that are located above/below the dash line there is a negative/positive contribution of the local fluxes at high resolution. The further from the dash line, the larger the contribution of the local fluxes. The stations located on top of the y-axis are mainly impacted by local fluxes. The surface stations in (a,b) are depicted with different symbols depending on whether they are classified as mountain, continental, coastal or remote (see Table A1), while TCCON stations that are strongly influenced by fluxes are labelled with station name. Note that different scales are used in each panel.

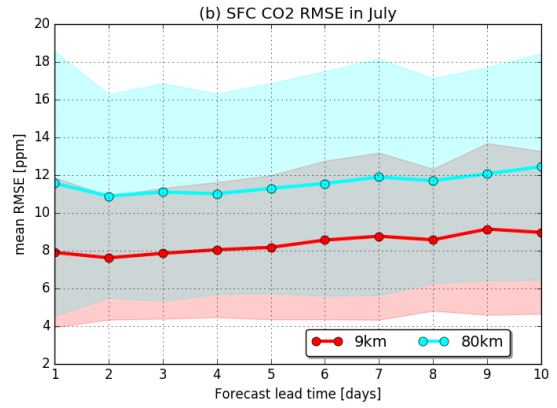
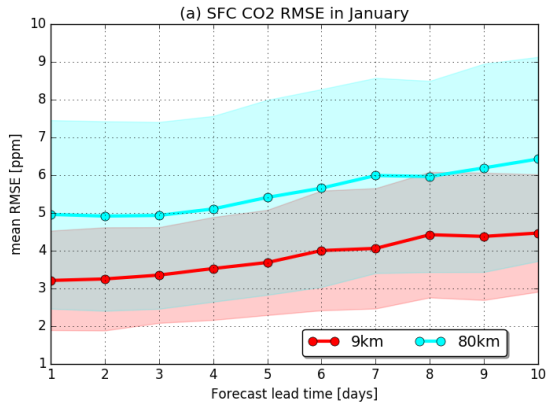


**Figure 9.** Mean RMSE of near-surface CO<sub>2</sub> [ppm] at different forecast lead times for the 9km-EXP (red) and 80km-EXP (blue) in (a) January and (b) July. The errors are computed with respect to hourly continuous in situ surface measurements from 51 stations (see Tab A1). The error standard deviation between the different stations is shown with the shaded area: red for 9 km, blue for 80 km and grey for overlap. Note that different scales are used in each panel.

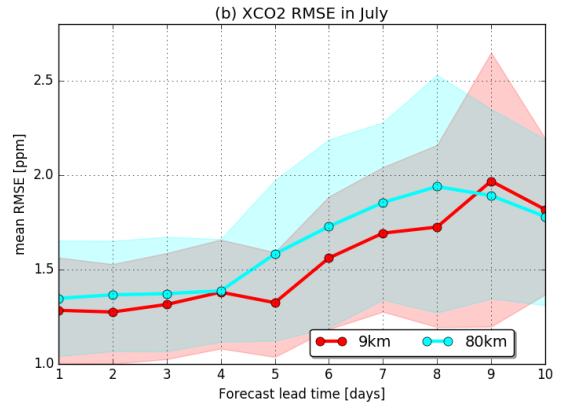
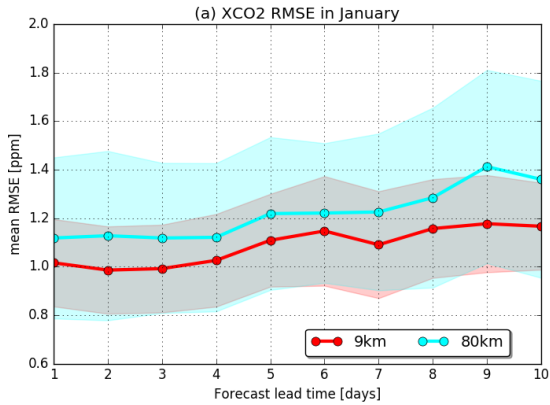


**Figure 10.** Same as 9 but for XCO<sub>2</sub> [ppm]. The errors are computed with respect to hourly TCCON observations from 18 TCCON stations (see Tab. A3).

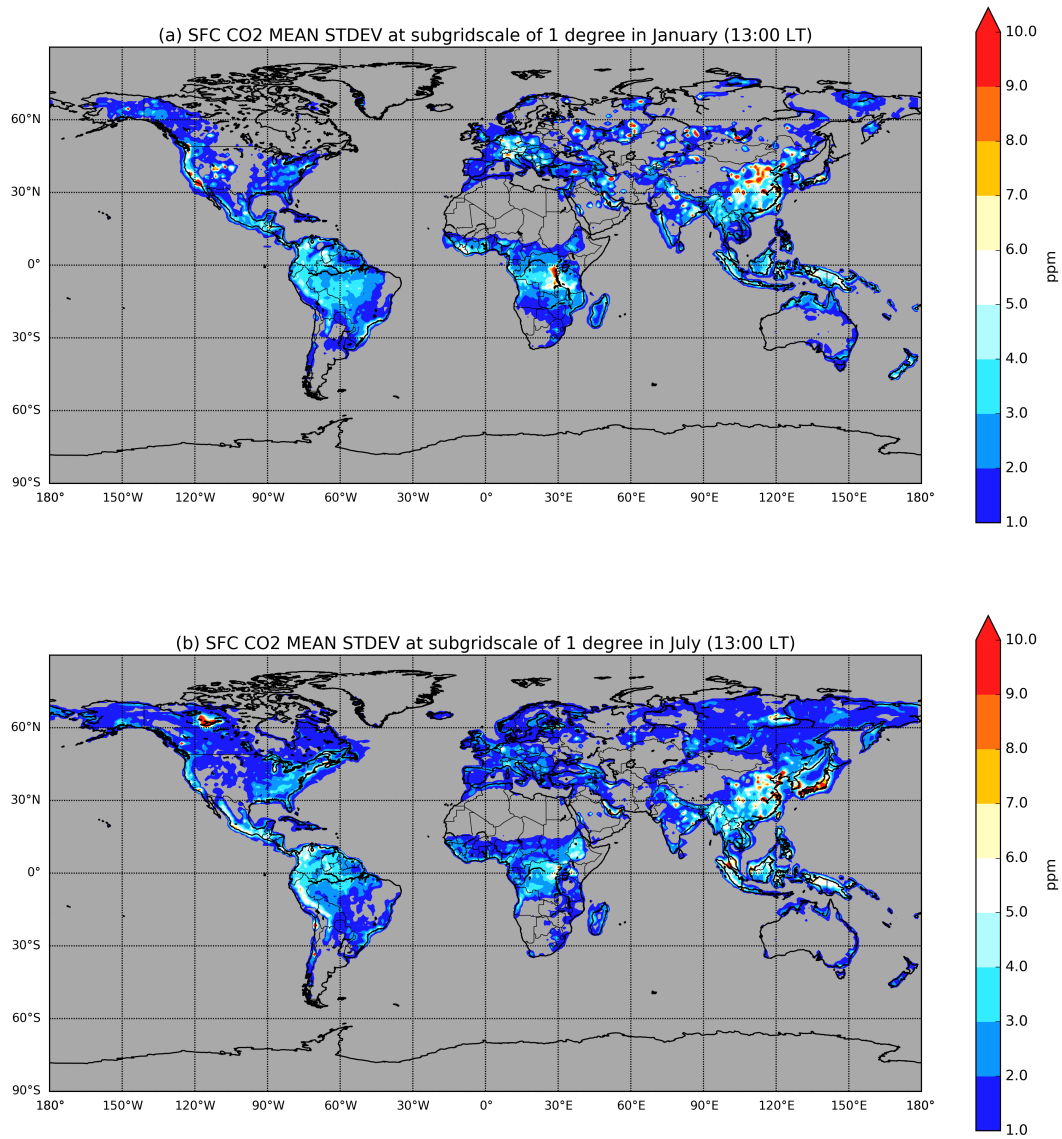


**Figure 11.** Monthly mean surface CO<sub>2</sub> small-scale variability ( $\sigma$ ) within 1 degree x 1 degree grid boxes [ppm] at 13:00 local time in (a) January and (b) July. **Grey shading denotes  $\sigma < 1.0$ .**

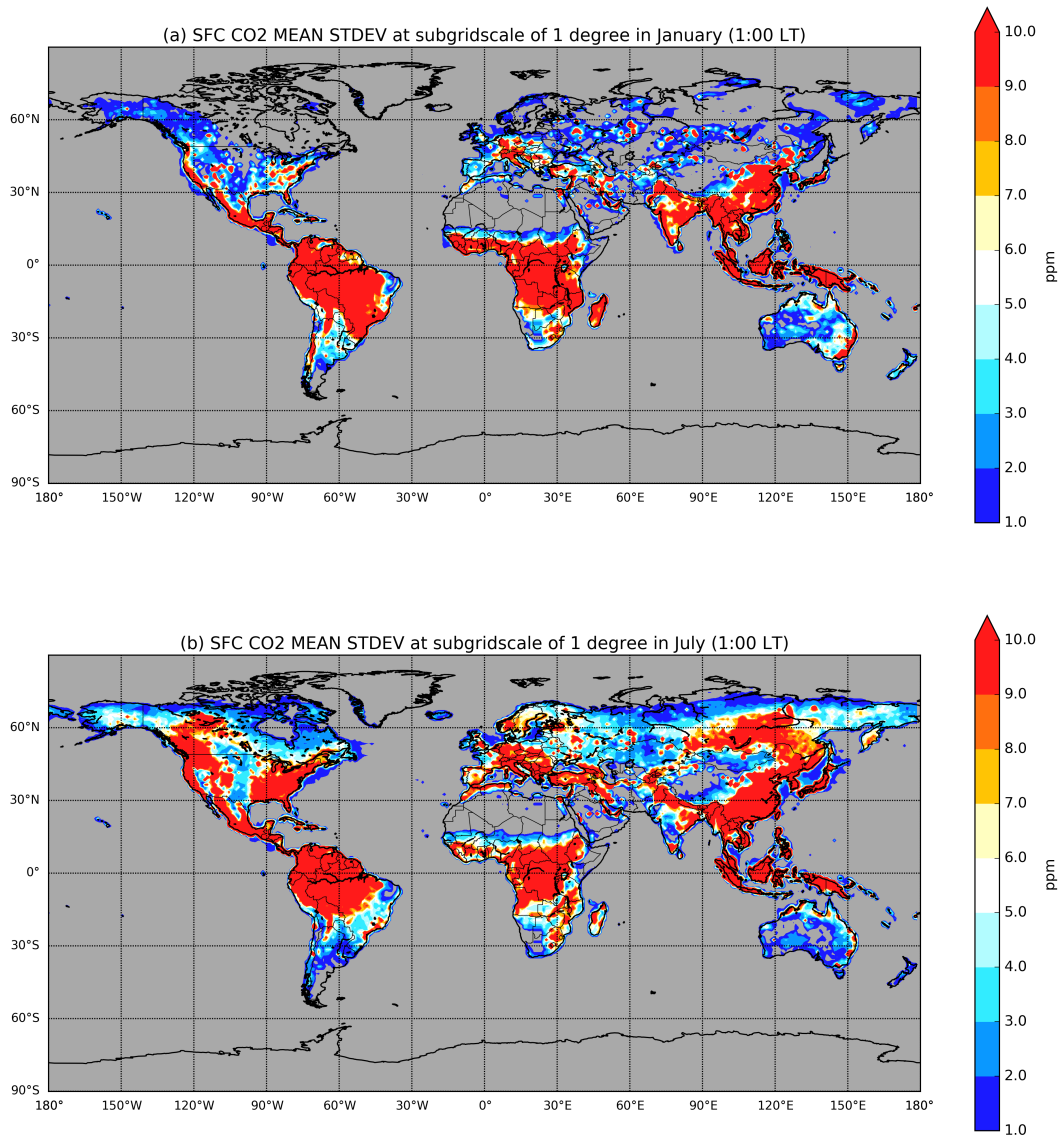


**Figure 12.** Monthly mean surface CO<sub>2</sub> small-scale variability ( $\sigma$ ) within 1 degree x 1 degree grid boxes [ppm] at 01:00 local time in (a) January and (b) July. **Grey shading denotes  $\sigma < 1.0$ .**

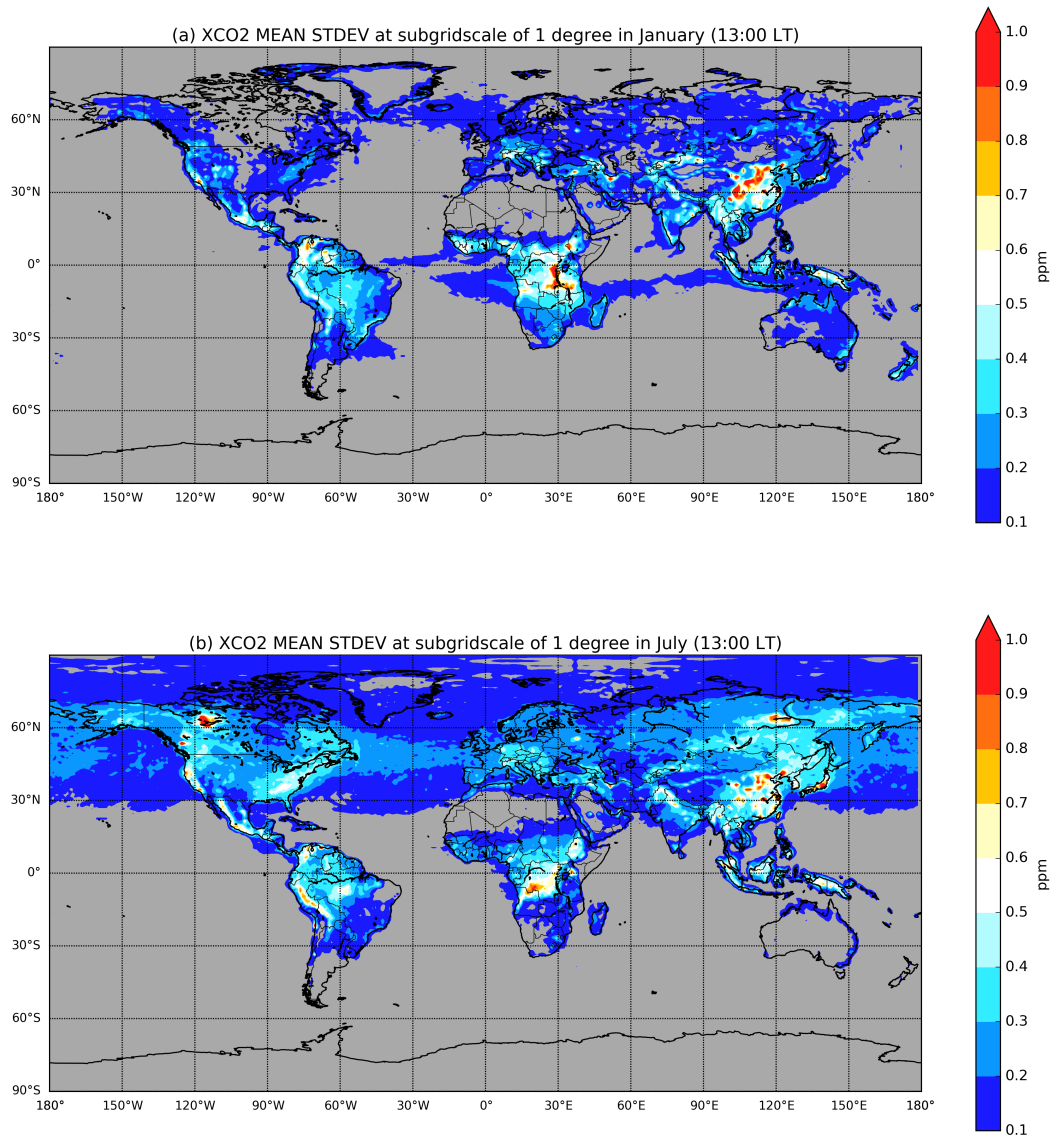


**Figure 13.** Monthly mean XCO<sub>2</sub> small-scale variability ( $\sigma$ ) within 1 degree x 1 degree grid boxes [ppm] at 13:00 local time in (a) January and (b) July. **Grey shading denotes  $\sigma < 0.1$ .**

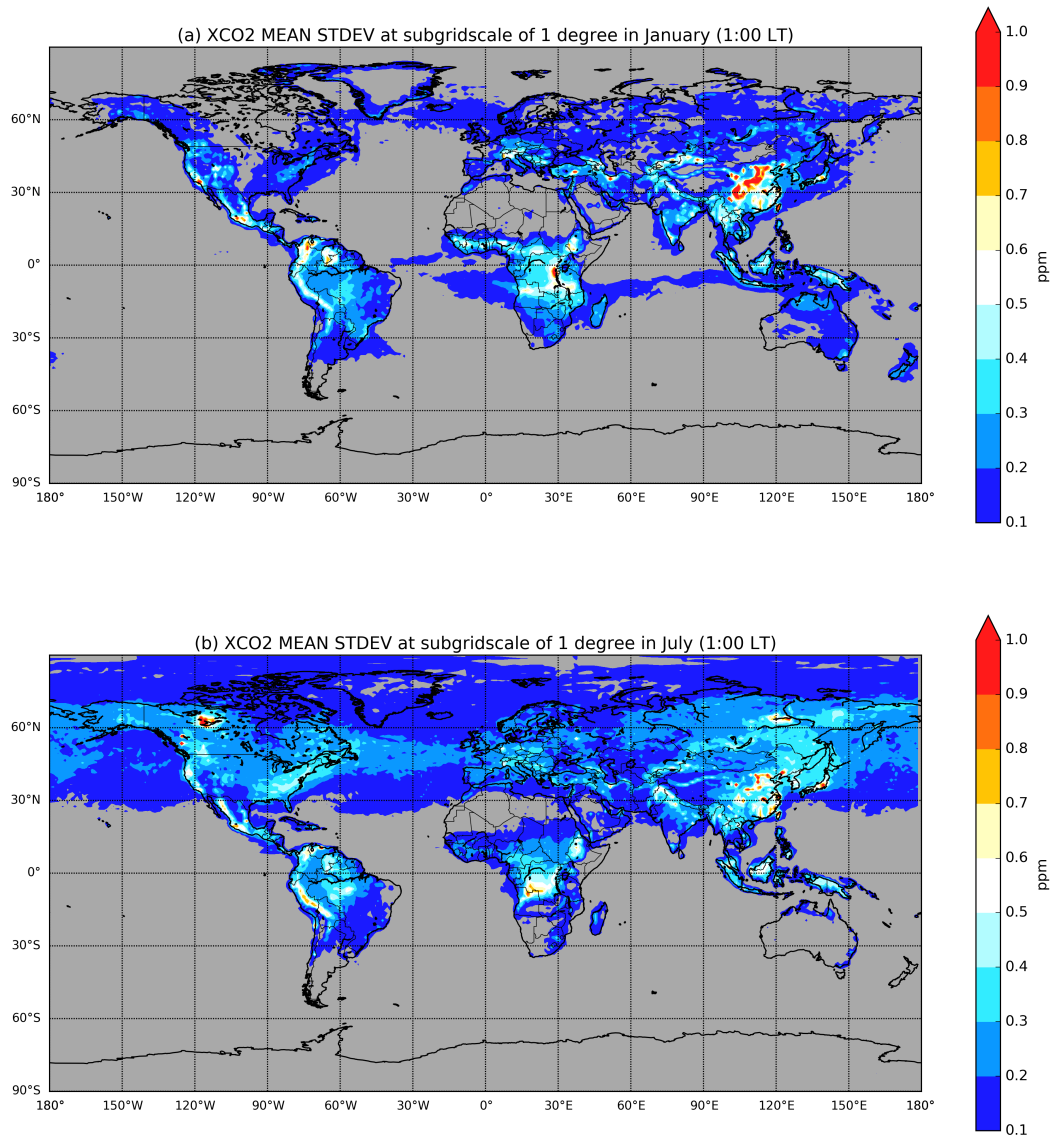


**Figure 14.** Monthly mean XCO<sub>2</sub> small-scale variability ( $\sigma$ ) within 1 degree x 1 degree grid boxes [ppm] at 1:00 local time in (a) January and (b) July. **Grey shading denotes  $\sigma < 0.1$ .**

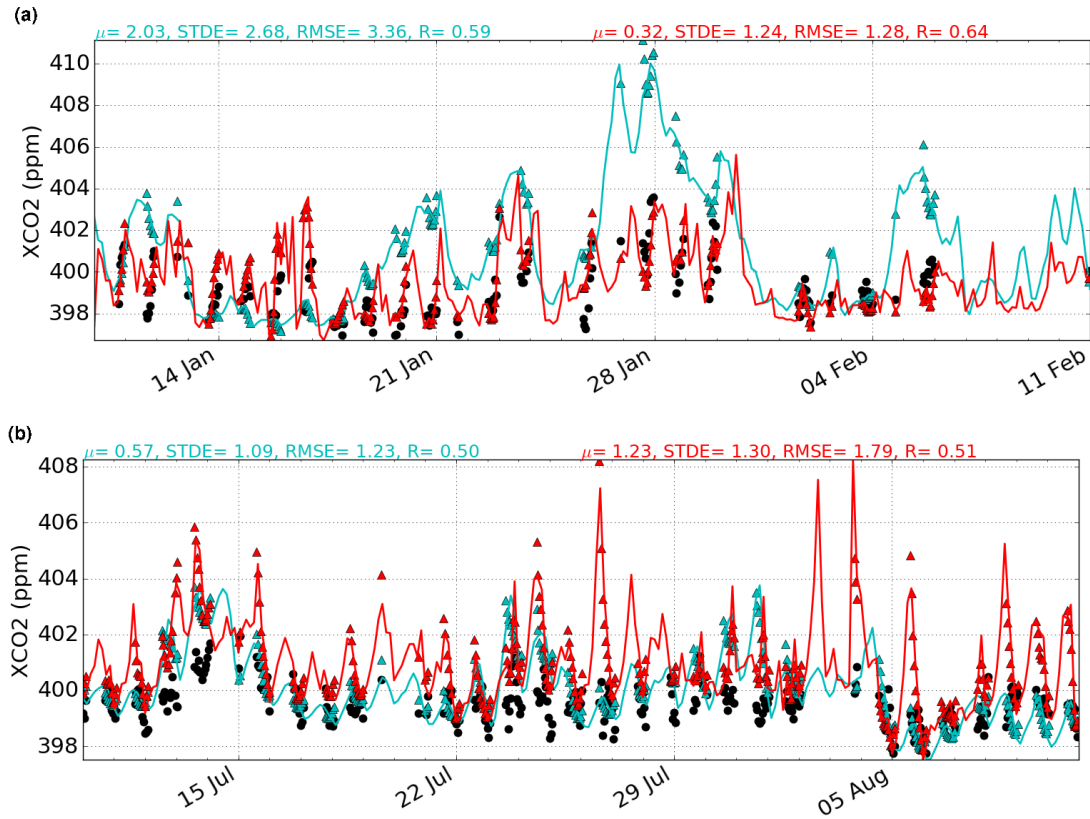


**Figure 15.** Hourly XCO<sub>2</sub> [ppm] at TCCON site of Pasadena (CA, USA) in (a) January and (b) July from 80km-EXP (blue) and 9km-EXP (red) and simulations. Hourly observations are shown black circles. Triangles represent the model XCO<sub>2</sub> after smoothing with TCCON averaging kernel and prior. The bias ( $\mu$ ), standard error (*STDE*) and Pearson correlation coefficient (*R*) from 80km-EXP (blue) and 9km-EXP (red) are shown at the top of each panel.

Table A1: Continuous in situ stations (surface and tower) used to evaluate synoptic variability. N/A denotes reference not available. The full names for the abbreviations of the network organizations are provided in Tab. A2.

<b>Station ID</b>	<b>Lat/Lon [degree]</b>	<b>Altitude [masl]</b>	<b>Intake height [magl]</b>	<b>Network</b>	<b>Reference</b>	<b>Type</b>
alt	82.45N/62.51W	200	10	ECCC	Worthy et al. (2003)	remote
brw	71.32N/-156.61	11	16	NOAA	Peterson et al. (1986)	coastal
cby	69.01N/105.05W	35	12	ECCC	N/A	continental
inu	68.32N/133.53W	113	10	ECCC	Worthy et al. (2003)	continental
pal	67.97N/24.12E	560	5	FMI	Hatakka et al. (2003)	continental
bck	62.80N/116.05W	179	60	ECCC	N/A	continental
chl	58.75N/94.07W	29	60	ECCC	Worthy et al. (2003)	coastal
llb	54.95N/112.45W	540	10	ECCC	Worthy et al. (2003)	continental
etl	54.35N/104.98W	492	105	ECCC	Worthy et al. (2003)	continental
mhd	53.33N/9.90W	5	24	LSCE	Ramonet et al. (2010)	coastal
wao	52.95N/1.12E	20	10	UEA	Wilson (2013)	coastal
ces	51.97N/4.93E	-1	200	ECN	Vermeulen et al. (2011)	continental
est	51.66N/110.21W	707	3	ECCC	Worthy et al. (2003)	continental
fsd	49.88N/81.57W	210	40	ECCC	Worthy et al. (2003)	continental
cps	49.82N/74.98W	381	8	ECCC	Worthy et al. (2003)	continental
esp	49.38N/126.54W	7	40	ECCC	Worthy et al. (2003)	coastal
kas	49.23N/19.98E	1989	5	AGH	Rozanski et al. (2003, 2014)	mountain
ssl	47.92N/7.92E	1205	12	UBA-SCHAU	Schmidt et al. (2003)	mountain
hun	46.95N/16.65E	248	115	HMS	Haszpra et al. (2001)	continental
jfj	46.55N/7.99E	3570	10	EMPA	Schibig et al. (2015)	mountain
lef	45.95N/90.27W	472	396	NOAA	Andrews et al. (2014)	continental
puy	45.77N/2.97E	1465	10	LSCE	Lopez et al. (2015)	mountain
amt	45.03N/68.68W	53	107	NOAA	Andrews et al. (2014)	continental
egb	44.23N/79.78W	251	3	ECCC	Worthy et al. (2003)	continental
wsa	43.93N/60.02W	5	25	ECCC	Worthy et al. (2003)	remote
vac	42.88N/3.21W	1086	20	ClimaDat	Morgu et al. (2013)	mountain
tpd	42.62N/80.55W	231	35	ECCC	Worthy et al. (2003)	continental

Continued on next page

**Table A1 – continued from previous page**

<b>Station ID</b>	<b>Lat/Lon [deg]</b>	<b>Altitude [masl]</b>	<b>Intake height [masl]</b>	<b>Network</b>	<b>Reference</b>	<b>Type</b>
dec	40.74N/0.79E	1	10	ClimaDat	Morguí et al. (2013)	coastal
hdp	40.56N/111.65W	3351	17.7	NCAR	Stephens et al. (2011)	mountain
spl	40.45N/106.73W	3210	9.1	NCAR	Stephens et al. (2011)	mountain
gic	40.35N/5.18W	1436	20	ClimaDat	Morguí et al. (2013)	mountain
nwr	40.05N/105.59W	3523	3.5	NCAR	Stephens et al. (2011)	mountain
bao	40.05N/105.0W	1584	300	NOAA	Andrews et al. (2014)	continental
ryo	39.03N/141.82E	260	20	JMA	Tsutsumi et al. (2005)	coastal
snp	38.62N/78.35W	1008	17	NOAA	Andrews et al. (2014)	mountain
wgc	38.27N/121.49W	0	483	NOAA	Andrews et al. (2014)	coastal
sgc	36.70N/5.38W	850	20	ClimaDat	Morguí et al. (2013)	continental
sct	33.41N/81.83W	115	305	NOAA	Andrews et al. (2014)	continental
wkt	31.31N/97.33W	251	457	NOAA	Andrews et al. (2014)	continental
izo	28.31N/16.50W	2373	13	AEMET	Gomez-Pelaez and Ramos (2011)	mountain
yon	24.47N/123.02E	30	20	JMA	Tsutsumi et al. (2005)	coastal
mnm	24.28N/153.98E	8	20	JMA	Tsutsumi et al. (2005)	remote
mlo	19.54N/-155.58	3397	40	NOAA	Thoning et al. (1989)	mountain
smo	14.25S/-170.56	42	10	NOAA	Halter et al. (1988)	remote
cpt	34.35S/18.49E	230	30	SAWS	Brunke et al. (2004)	coastal
ams	37.80S/77.54E	55	20	LSCE	Gaudry et al. (1991)	remote
cgo	40.68S/144.69E	94	70	CSIRO	Francey et al. (2003)	coastal
mqa	54.50S/158.94E	6	10	CSIRO	Stavert et al. (2018)	remote
cya	66.28S/110.52E	47	7	CSIRO	Loh et al. (2017)	remote
syo	69.01S/39.59E	14	8	TU	N/A	remote
spo	89.98S/-24.80	2810	10	NOAA	Conway and Thoning (1990)	remote

**Table A2.** Organizations associated with observing stations.

<b>Abbreviation</b>	<b>Organization</b>
AEMET	Izana Atmospheric Research Center, Meteorological State Agency of Spain
AGH	AGH University of Science and Technology, Krakzów, Poland
BIRA-IASB	Royal Belgian Institute for Space Aeronomy, Brussels, Belgium
Caltech	California Institute of Technology
ClimaDat	Land, atmosphere and Oceans Laboratory at the Institut Català de Ciències del Clima (2010-2016); at Institut de Ciència i Tecnologia Ambientals, Universitat Autònoma de Barcelona (since 2017)
CSIRO	Commonwealth Scientific and Industrial Research Organization, Oceans & Atmosphere
ECCC	Environment and Climate Change Canada
ECN	Energy Research Centre of the Netherlands
EMPA	Swiss Federal Laboratories for Materials Science and Technology
FMI	Finish Meteorological Institute
HMS	Hungarian Meteorological Service
KIT	Karlsruhe Institute of Technology
LSCE	Laboratoire des Sciences du Climat et de l'Environnement
MPI-BGC	Max Planck Institute for Biogeochemistry
NASA	National Aeronautics and Space Administration
JAXA	Japan Aerospace Exploration Agency
JMA	Japan Meteorological Agency
NIES	National Institute for Environmental Studies
NIWA	National Institute of Water and Atmospheric
NCAR	National Center For Atmospheric Research
NOAA	NOAA Global Monitoring Division
SAWS	South African Weather Service
TU	Tohoku University
UBA-SCHAU	Umweltbundesamt, Station Schauinsland
UBremen-IUP	Institute of Environmental Physics, Universität Bremen
UEA	University of East Anglia
UHEI-IUP	University of Heidelberg, Institut fuer Umweltphysik
UOW	University of Wollongong
UR	Université de La Réunion

**Table A3.** TCCON stations

<b>Station ID</b>	<b>Latitude/ Longitude [deg]</b>	<b>Altitude [m]</b>	<b>N data Jan</b>	<b>N data Jul</b>	<b>Organization</b>	<b>Reference</b>
bialystok01	53.23°N/23.02°E	180	15	68	UBremen-IUP	Deutscher et al. (2014)
bremen01	53.10°N/8.85°E	27	8	44	UBremen-IUP	Notholt et al. (2014a)
Karlsruhe	49.10°N/8.44°E	116	33	90	KIT	Hase et al. (2014)
orleans01	47.97°N/2.11°E	130	67	16	UBremen-IUP	Warneke et al. (2014)
garmisch01	47.48°N/11.06°E	740	33	90	KIT	Sussmann and Rettinger (2014)
parkfalls01	45.94°N/90.27°W	440	28	168	Caltech	Wennberg et al. (2014b)
rikubetsu01	43.46°N/143.77°E	30	21	9	NIES	Morino et al. (2017a)
lamont01	36.60°N/97.49°W	320	129	299	Caltech	Wennberg et al. (2016a)
tsukuba02	36.05°N/140.12°E	30	111	120	NIES	Morino et al. (2014b)
edwards01	34.96°N/117.88°W	699	191	316	NASA	Iraci et al. (2016)
pasadena01	34.14°N/118.13°W	230	160	302	Caltech	Wennberg et al. (2014c)
saga01	33.24°N/130.29°E	7	30	30	JAXA	Shiomi et al. (2014)
izana01	28.30°N/16.48°W	2370	43	18	AEMET/KIT	Blumenstock et al. (2014)
ascension01	7.92°S/14.33°W	10	153	158	MPI-BGC	Feist et al. (2014)
darwin01	12.43°S/130.89°E	30	34	264	UOW	Griffith et al. (2014a)
reunion01	20.90°S/55.49°E	87	150	136	BIRA-IASB/UR	De Mazière et al. (2014)
wollongong01	34.41°S/150.88°E	30	157	96	UOW	Griffith et al. (2014b)
lauder02	45.04°S/169.68°E	370	104	86	NIWA	Sherlock et al. (2014)

*Author contributions.* The simulations were performed by A. Agustí-Panareda; the coding of the mass fixer required for the high resolution transport in the IFS was done by M. Diamantakis; the concept and ideas to design the high resolution simulations were devised by F. Chevallier, A. Agustí-Panareda, M. Diamantakis, S. Massart, J. Muñoz-Sabater in discussion with R. Engelen and V.-H. Peuch; R. Law, Z. Loh, J.A. Morguí, R. Curcoll provided additional observations at crucial sites and guidance on the evaluation of the simulations; C. Roehl and D. Wunch provided data and input on the interpretation of the model evaluation at the TCCON site of Pasadena; the CO<sub>2</sub> validation tools have been developed by S. Massart and A. Agustí-Panareda; the manuscript was prepared by A. Agustí-Panareda with input and feedback from M. Diamantakis, S. Massart, F. Chevallier, J. Muñoz-Sabater, J. Barré, R. Engelen, B. Langerock, R. Law, Z. Loh, J.A. Morguí, M. Parrington, V.-H. Peuch, M. Ramonet, C. Roehl, A.T. Vermeulen, T. Warneke and D. Wunch.

*Competing interests.* The authors declare that they have no conflict of interest.

*Acknowledgements.* This research was generated using Copernicus Atmosphere Monitoring Service Information [2018]. Anna Agustí-Panareda has been partly funded by the CHE project. The CHE project has received funding from the European Union's Horizon 2020 research and innovation programme under grant agreement No 776186. Frédéric Chevallier received funding from the Copernicus Atmosphere Monitoring Service, implemented by the European Centre for Medium-Range Weather Forecasts (ECMWF) on behalf of the European Commission. Thanks to all the station PIs from the numerous individual stations and networks like NOAA, ICOS, AEMET, AGH, CSIRO, ECCC, ECN, EMPA, FMI, HMS, LSCE, NCAR, JMA, MPI-BGC, NIWA, SAWS, TU, UBA-SCHAU, UEA, UHEI-IUP, UR, UBremen-IUP, BIRA-IASB, Caltech, KIT, NASA, JAXA, NIES, UOW that contributed their CO<sub>2</sub> observations to the cooperative GLOBALVIEWplus ObsPack (2015) product and TCCON which are fundamental for the evaluation of the model simulations. The ClimaDat Network has received funding from "la Caixa" Foundation, under agreement 2010-002624. We are grateful to many colleagues at ECMWF for their support and fruitful discussions, particularly to Gabor Radnoti, Thomas Haiden and Martin Janousek for their technical support in the evaluation of the winds, Johannes Flemming and Zak Kipling for their support in the implementation of the additional CO<sub>2</sub> tracers in the IFS model, Sylvie Malardel for her support and discussions on the general aspects of atmospheric tracer modelling in the IFS, Gianpaolo Balsamo, Souhail Boussetta, Zak Kipling and Johannes Flemming for their technical support on the implementation of a bug fix in the CTESSEL model of biogenic emissions, and Miha Razinger for his technical support in the production of figure 1. Many thanks to Paul Wennberg (Caltech) for his advice on the use of the TCCON data, Martin Krol (Wageningen University) for his suggestions on the evaluation of the daily maximum CO<sub>2</sub> and Britton Stephens (NCAR) for his comments on the mountain site evaluation which helped improve the description of the vertical sampling strategy and to emphasize the importance of high resolution at mountain sites.

## References

- Agustí-Panareda, A., Massart, S., Chevallier, F., Boussetta, S., Balsamo, G., Beljaars, A., Ciais, P., Deutscher, N., Engelen, R., Jones, L., Kivi, R., Paris, J.-D., Peuch, V.-H., Sherlock, V., Vermeulen, A., Wennberg, P., and Wunch, D.: Forecasting global atmospheric CO<sub>2</sub>, *Atmos. Chem. Phys.*, 14, 11 959–11 983, <https://doi.org/10.5194/acp-14-11959-2014>, 2014.
- 5 Agustí-Panareda, A., Massart, S., Chevallier, F., Balsamo, G., Boussetta, S., Dutra, E., and Beljaars, A.: A biogenic CO<sub>2</sub> flux adjustment scheme for the mitigation of large-scale biases in global atmospheric CO<sub>2</sub> analyses and forecasts, *ACPD*, 2016, 1–45, <https://doi.org/10.5194/acp-2015-987>, 2016.
- Agustí-Panareda, A., Diamantakis, M., Bayona, V., Klappenbach, F., and Butz, A.: Improving the inter-hemispheric gradient of total column atmospheric CO<sub>2</sub> and CH<sub>4</sub> in simulations with the ECMWF semi-Lagrangian atmospheric global model, *Geosci. Model Dev.*, 10, 1–18, <https://doi.org/10.5194/gmd-10-1-2017>, 2017.
- 10 Ahmadov, R., Gerbig, C., Kretschmer, R., Körner, S., Rödenbeck, C., Bousquet, P., and Ramonet, M.: Comparing high resolution WRF-VPRM simulations and two global CO<sub>2</sub> transport models with coastal tower measurements of CO<sub>2</sub>, *Biogeosciences*, 6, 807-817, <https://doi.org/10.5194/bg-6-807-2009>, 2009.
- Alkhaled, A. A., Michalak, A.M., and Kawa, S.R.: Using CO<sub>2</sub> spatial variability to quantify representation errors of satellite CO<sub>2</sub> retrievals, *Geophys. Res. Lett.*, 35, L16813, <https://doi.org/10.1029/2008GL034528>, 2008.
- 15 Andrews, A. E., J. D. Kofler, M. E. Trudeau, J. C. Williams, D. H. Neff, K. A. Masarie, D. Y. Chao, D. R. Kitzis, P. C. Novelli, C. L. Zhao, E. J. Dlugokencky, P. M. Lang, M. J. Croswell, M. L. Fischer, M. J. Parker, J. T. Lee, D. D. Baumann, A. R. Desai, C. O. Stanier, S. F. J. de Wekker, D. E. Wolfe, J. W. Munger and P. P. Tans. CO<sub>2</sub>, CO and CH<sub>4</sub> measurements from the NOAA Earth System Research Laboratory, *Atmospheric Measurement Techniques*, 7, 647-687, <https://doi.org/10.5194/amt-7-647-2014>, 2014.
- 20 Bechtold, P., Köhler, M., Jung, T., Doblas-Reyes, F., Leutbecher, M., Rodwell, M., Vitart, F., and Balsamo, G.: Advances in simulating atmospheric variability with the ECMWF model: From synoptic to decadal time-scales, *Q.J.R. Meteorol. Soc.*, 134, 1337–1351, 2008.
- Bechtold, P., Semane, N., Lopez, P., Chaboureau, J.-P., Beljaars, A., and Bormann, N.: Representing equilibrium and nonequilibrium convection in large-scale models, *J. Atmos. Sci.*, 71, 734–753, 2014.
- Belikov, D. A., Maksyutov, S., Ganshin, A., Zhuravlev, R., Deutscher, N. M., Wunch, D., Feist, D. G., Morino, I., Parker, R. J., Strong, K., 25 Yoshida, Y., Bril, A., Oshchepkov, S., Boesch, H., Dubey, M. K., Griffith, D., Hewson, W., Kivi, R., Mendonca, J., Notholt, J., Schneider, M., Sussmann, R., Velasco, V. A., and Aoki, S.: Study of the footprints of short-term variation in XCO<sub>2</sub> observed by TCCON sites using NIES and FLEXPART atmospheric transport models, *Atmos. Chem. Phys.*, 17, 143-157, <https://doi.org/10.5194/acp-17-143-2017>, 2017.
- Balzarolo, M., Boussetta, S., Balsamo, G., Beljaars, A., Maignan, F., Calvet, J.-C., Lafont, S., Barbu, A., Poulter, B., Chevallier, F., Szczypta, C., and Papale, D.: Evaluating the potential of large-scale simulations to predict carbon fluxes of terrestrial ecosystems over a European 30 Eddy Covariance network, *Biogeosciences*, 11, 2661–2678, <https://doi.org/10.5194/bg-11-2661-2014>, 2014.
- Beljaars, A. and Viterbo, P.: The role of the boundary layer in a numerical weather prediction model, in *Clear and cloudy boundary layers*, Royal Netherlands Academy of Arts and Sciences, North Holland Publishers, Amsterdam, 1998.
- Blumenstock, T., Hase, F., Schneider, M., García, O. E., and Sepúlveda, E.: TCCON data from Izana, Tenerife, Spain, Release GGG2014R1. TCCON data archive, hosted by CaltechDATA, California Institute of Technology, Pasadena, CA, U.S.A. 35 <https://doi.org/10.14291/tcon.ggg2014.izana01.R1>, 2014.

- Boussetta, S., Balsamo, G., Beljaars, A., Agustí-Panareda, A., Calvet, J.-C., Jacobs, C., van den Hurk, B., Viterbo, P., Lafont, S., Dutra, E., Jarlan, L., Balzarolo, M., Papale, D., and van der Werf, G.: Natural carbon dioxide exchanges in the ECMWF Integrated Forecasting System: Implementation and offline validation, *J. Geophys. Res: Atm.*, 118, 1–24, <https://doi.org/10.1002/jgrd.50488>, 2013.
- Brooks, B.-G. J., Desai, A. R., Stephens, B. B., Bowling, D. R., Burns, S. P., Watt, A. S., Heck, S. L., and Sweeney, C.: Assessing filtering of mountaintop CO<sub>2</sub> mole fractions for application to inverse models of biosphere-atmosphere carbon exchange, *Atmos. Chem. Phys.*, 12, 2099-2115, <https://doi.org/10.5194/acp-12-2099-2012>, 2012.
- Brunke, E.-G., Labuschagne, C., Parker, B., Scheel, H.E. and Whittlestone, S.: Baseline air mass selection at Cape Point, South Africa: Application of 222Rn and other filter criteria to CO<sub>2</sub>. *Atmospheric Environment* 38, 33, (Oct 04), 5693 - 5702, 2004.
- Chevallier, F., Ciais, P., Conway, T., Aalto, T., Anderson, B., Bousquet, P., Brunke, E., Ciattaglia, L., Esaki, Y., Fröhlich, M., Gomez, A., Gomez-Pelaez, A., Haszpra, L., Krummel, P., Langenfelds, R., Leuenberger, M., Machida, T., Maignan, F., Matsueda, H., Morguá, J., Mukai, H., Nakazawa, T., Peylin, P., Ramonet, M., Rivier, L., Sawa, Y., Schmidt, M., Steele, L., Vay, S., Vermeulen, A., Wofsy, S., and Worthy, D.: CO<sub>2</sub> surface fluxes at grid point scale estimated from a global 21 year reanalysis of atmospheric measurements, *J. Geophys. Res.*, 115, <https://doi.org/doi:10.1029/2010JD013887>, 2010.
- Chevallier, F., P. I. Palmer, L. Feng, H. Boesch, C. W. O'Dell, and P. Bousquet, Toward robust and consistent regional CO<sub>2</sub> flux estimates from in situ and spaceborne measurements of atmospheric CO<sub>2</sub>, *Geophys. Res. Lett.*, 41, 1065–1070, <https://doi.org/10.1002/2013GL058772>, 2014.
- Conway, T. J. and Thoning, K.W.: Short-term variations of atmospheric carbon dioxide at the South Pole, *Antarctic Journal of the United States*, 236-238, 1990.
- Corbin, K., Denning, A. S., Wang, J.-W., Lu, L. and Baker, I.T.: Possible representation errors in inversions of satellite CO<sub>2</sub> retrievals, *J. Geophys. Res.*, 113, D02301, <https://doi.org/10.1029/2007JD008716>, 2008.
- Corbin, K.D., Denning, A.S., Gurney, K.R: The space and time impacts on U.S. regional atmospheric CO<sub>2</sub> concentrations from a high resolution fossil fuel CO<sub>2</sub> emissions inventory. *Tellus B*, 62: 506-511, <https://doi.org/10.1111/j.1600-0889.2010.00480.x>, 2010.
- Crisp, D., Pollock, H. R., Rosenberg, R., Chapsky, L., Lee, R. A. M., Oyafuso, F. A., Frankenberg, C., O'Dell, C. W., Bruegge, C. J., Doran, G. B., Eldering, A., Fisher, B. M., Fu, D., Gunson, M. R., Mandrake, L., Osterman, G. B., Schwandner, F. M., Sun, K., Taylor, T. E., Wennberg, P. O., and Wunch, D.: The on-orbit performance of the Orbiting Carbon Observatory-2 (OCO-2) instrument and its radiometrically calibrated products, *Atmos. Meas. Tech.*, 10, 59-81, <https://doi.org/10.5194/amt-10-59-2017>, 2017.
- Staniforth, A. and J.Côté, Semi-Lagrangian integration schemes for atmospheric models - a review, *Mon.Wea.Rev.*, 119, 2206-2223, <https://doi.org/10.1175/1520-0493>, 1991.
- Dee, D. and Coauthors: The ERA-Interim re- analysis: Configuration and performance of the data assimilation system. *Quart. J. Roy. Meteor. Soc.*, 137, 553–597, <https://doi.org/10.1002/qj.828>, 2011.
- De Mazière, M., Sha, M. K., Desmet, F., Hermans, C., Scolas, F., Kumps, N., Metzger, J.-M., Dufлот, V., Cammas, J.-P.: TCCON data from Reunion Island (La Reunion), France, Release GGG2014R0. TCCON data archive, hosted by CaltechDATA, California Institute of Technology, Pasadena, CA, U.S.A. <https://doi.org/10.14291/tcon.ggg2014.reunion01.R0/1149288>, 2014.
- Deutscher, N., J. Notholt, J. Messerschmidt, C. Weinzierl, T. Warneke, C. Petri, P. Gripe, K. Katrynski. TCCON data from Bialystok, Poland, Release GGG2014R1. TCCON data archive, hosted by CaltechDATA, California Institute of Technology, Pasadena, CA, U.S.A. <https://doi.org/10.14291/tcon.ggg2014.bialystok01.R1/1183984>, 2014.
- Diamantakis M, Magnusson L.: Sensitivity of the ECMWF model to semi-Lagrangian departure point iterations, *Mon. Weather Rev.* 144, 3233 – 3250, <https://doi.org/10.1175/MWR-D-15-0432.1>, 2016.

- Diamantakis, M. and A. Agustí-Panareda: A positive definite tracer mass fixer for high resolution weather and atmospheric composition forecasts, ECMWF Technical Memorandum, No. 819, <https://www.ecmwf.int/en/elibrary/17914-positive-definite-tracer-mass-fixer-high-resolution-weather-and-atmospheric>, 2017.
- 5 Feist, D. G., S. G. Arnold, N. John, M. C. Geibel, M. Christoph. TCCON data from Ascension Island (SH), Release GGG2014R0, TCCON data archive, hosted by CaltechDATA, California Institute of Technology, Pasadena, CA, U.S.A. <https://doi.org/10.14291/tcon.ggg2014.ascension01.R0/1149285>, 2014.
- Feng, S., Lauvaux, T., Newman, S., Rao, P., Ahmadov, R., Deng, A., Díaz-Isaac, L. I., Duren, R. M., Fischer, M. L., Gerbig, C., Gurney, K. R., Huang, J., Jeong, S., Li, Z., Miller, C. E., O’Keeffe, D., Patarasuk, R., Sander, S. P., Song, Y., Wong, K. W., and Yung, Y. L.: Los Angeles megacity: a high-resolution land–atmosphere modelling system for urban CO<sub>2</sub> emissions, *Atmos. Chem. Phys.*, 16, 9019-9045, <https://doi.org/10.5194/acp-16-9019-2016>, 2016.
- 10 Flemming, J., Huijnen, V., Arteta, J., Bechtold, P., Beljaars, A., Blechschmidt, A.-M., Diamantakis, M., Engelen, R. J., Gaudel, A., Inness, A., Jones, L., Josse, B., Katragkou, E., Marecal, V., Peuch, V.-H., Richter, A., Schultz, M. G., Stein, O., and Tsikerdekis, A.: Tropospheric chemistry in the Integrated Forecasting System of ECMWF, *Geoscientific Model Development*, 8, 975–1003, <https://doi.org/10.5194/gmd-8-975-2015>, <http://www.geosci-model-dev.net/8/975/2015/>, 2015.
- 15 Francey, R.J., L.P. Steele, D.A. Spencer, R.L. Langenfelds, R.M. Law, P.B. Krummel, P.J. Fraser, D.M. Etheridge, N. Derek, S.A. Coram, L.N. Cooper, C.E. Allison, L. Porter and S. Baly, The CSIRO (Australia) measurement of greenhouse gases in the global atmosphere, report of the 11th WMO/IAEA Meeting of Experts on Carbon Dioxide Concentration and Related Tracer Measurement Techniques, Tokyo, Japan, September 2001, S.Toru and S. Kazuto (editors), World Meteorological Organization Global Atmosphere Watch, 97-111, 2003.
- 20 Gaudry, A., P. Monfray, G. Polian, G. Bonsang, B. Ardouin, A. Jegou, and G. Lambert. Non-seasonal variations of atmospheric CO<sub>2</sub> concentrations at Amsterdam Island. *Tellus* 43B, 136-143, 1991.
- Geels, C. , Doney, S. C., Dargaville, R. , Brandt, J. and Christensen, J. H.: Investigating the sources of synoptic variability in atmospheric CO<sub>2</sub> measurements over the Northern Hemisphere continents: a regional model study. *Tellus B*, 56: 35-50. <https://doi.org/10.1111/j.1600-0889.2004.00084.x>, 2004.
- 25 Gomez-Pelaez, A.J., Ramos, R., "Improvements in the Carbon Dioxide and Methane Continuous Measurement Programs at Izana Global GAW Station (Spain) during 2007-2009", in GAW report (No. 194) of the "15th WMO/IAEA Meeting of Experts on Carbon Dioxide, Other Greenhouse Gases, and Related Tracer Measurement Techniques (Jena, Germany; September 7-10, 2009)", edited by Willi A. Brand, World Meteorological Organization (TD No. 1553), 133-138, 2011.
- Griffith, D. W. T., N. Deutscher, V. A. Velasco, P. O. Wennberg, Y. Yavin, G. Keppel Aleks, R. Washenfelder, G. C. Toon, J.-F. Blavier, C. 30 Murphy, N. Jones, G. Kettlewell, B. Connor, R. Macatangay, C. Roehl, M. Ryzcek, J. Glowacki, T. Culgan, G. Bryant. TCCON data from Darwin, Australia, Release GGG2014R0. TCCON data archive, hosted by CaltechDATA, California Institute of Technology, Pasadena, CA, U.S.A. <https://doi.org/10.14291/tcon.ggg2014.darwin01.R0/1149290>, 2014.
- Griffith, D. W. T., V. A. Velasco, N. Deutscher, C. Murphy, N. Jones, S. Wilson, R. Macatangay, G. Kettlewell, R. R. Buchholz, M. Riggeng- 35 bach. TCCON data from Wollongong, Australia, Release GGG2014R0. TCCON data archive, hosted by CaltechDATA, California Institute of Technology, Pasadena, CA, U.S.A. <https://doi.org/10.14291/tcon.ggg2014.wollongong01.R0/1149291>, 2014.
- S. Guerlet, A. Butz, D. Schepers, S. Basu, O. P. Hasekamp, A. Kuze, T., Yokota, J.F. Blavier, N. M. Deutscher, D.W.T. Griffith, F. Hase, E. Kyro, I. Morino, V. Sherlock, R. Sussmann, A. Galli, I. Aben: Impact of aerosol and thin cirrus on retrieving and validating XCO<sub>2</sub> from GOSAT shortwave infrared measurements, *J. Geophys. Res. Atmos.*, 118, 4887–4905, <https://doi.org/10.1002/jgrd.50332>, 2013.

- Gurney, K. R., Law, R. M., Denning, A. S., Rayner, P. J., Baker, D., Bousquet, P., Bruhwiler, L., Chen, Y.-H., Ciais, P., Fan, S., Fung, I. Y., Gloor, M., Heimann, M., Higuchi, K., John, J., Kowal-czyk, E., Maki, T., Maksyutov, S., Peylin, P., Prather, M., Pak, B. C., Sarmiento, J., Taguchi, S., Takahashi, T., and Yuen, C.-W.: TransCom 3 inversion intercomparison: 1. Annual mean control results and sensitivity to transport and prior flux information, *Tellus*, 55B, 555–579, 2003.
- 5 Haiden, T., Janousek, M., Bidlot, J.-R., Ferranti, L., Prates, F., Vitart, F., Bauer, P., Richardson, D.: Evaluation of ECMWF forecasts, including 2016-2017 upgrades, ECMWF Technical Memorandum, No. 817, ECMWF, <https://www.ecmwf.int/en/elibrary/17913-evaluation-ecmwf-forecasts-including-2016-2017-upgrades>, 2017.
- Halter, B. and Harris, J. M.: On the variability of atmospheric carbon dioxide concentration at Barrow, Alaska, during winter, *Journal of Geophysical Research*, 88(C11), 6858-6864, 1983.
- 10 Halter, B.C., Harris, J.M., and Conway, T.J., Component signals in the record of atmospheric carbon dioxide concentration at American Samoa, *J. Geophys. Res.*, 93, 15914-15918, 1988.
- Hase, F., T. Blumenstock, S. Dohe, J. Groß, M. Kiel. 2017. TCCON data from Karlsruhe, Germany, Release GGG2014R1. TCCON data archive, hosted by CaltechDATA, California Institute of Technology, Pasadena, CA, U.S.A. <https://doi.org/10.14291/tcon.ggg2014.karlsruhe01.R1/1182416>, 2014.
- 15 Haszpra, L., Barcza, Z., Bakwin, P. S., Berger, B. W., Davis, K. J., Weidinger, T. Measuring system for the long-term monitoring of biosphere/atmosphere exchange of carbon dioxide. *J. of Geophysical Research* 106D, 3057-3070, 2001.
- Hatakka J., Aalto T., Aaltonen V., Aurela M., Hakola H., Komppula M., Laurila T., Lihavainen H., Paatero J., Salminen K. and Viisanen Y. Overview of the atmospheric research activities and results at Pallas GAW station. *Boreal Environment Research*, 8(4):365-384, 2003.
- Hedelius, J. K., Feng, S., Roehl, C. M., Wunch, D., Hillyard, P. W., Podolske, J. R., Iraci, L. T., Patarasuk, R., Rao, P., O’Keeffe, D., Gurney, K. R., Lauvaux, T. and Wennberg, P. O.: Emissions and topographic effects on column CO<sub>2</sub> (XCO<sub>2</sub>) variations, with a focus on the Southern California Megacity, *J. Geophys. Res. Atmos.*, 122(13), 7200–7215, <https://doi.org/10.1002/2017JD026455>, 2017.
- 20 Hedelius, J. K., Liu, J., Oda, T., Maksyutov, S., Roehl, C. M., Iraci, L. T., Podolske, J. R., Hillyard, P. W., Wunch, D., and Wennberg, P. O.: Southern California Megacity CO<sub>2</sub>, CH<sub>4</sub>, and CO flux estimates using remote sensing and a Lagrangian model, *Atmos. Chem. Phys. Discuss.*, <https://doi.org/10.5194/acp-2018-517>, in review, 2018.
- 25 Holm, E., Forbes, R., Lang, S., Magnusson, L., Malardel, S.: New model cycle brings higher resolution, ECMWF Newsletter, No 147, Spring 2016.
- Houweling, S., Aben, I., Breon, F.-M., Chevallier, F., Deutscher, N., Engelen, R., Gerbig, C., Griffith, D., Hungershofer, K., Macatangay, R., Marshall, J., Notholt, J., Peters, W., , and Serrar, S.: The importance of transport model uncertainties for the estimation of CO<sub>2</sub> sources and sinks using satellite measurements, *Atmos. Chem. Phys.*, 10, 9981–9992, <https://doi.org/10.5194/acp-10-9981-2010>, 2010.
- 30 Inness, A., Ades, M., Agustí-Panareda, A., Barré, J., Benedictow, A., Blechschmidt, A.-M., Dominguez, J. J., Engelen, R., Eskes, H., Flemming, J., Huijnen, V., Jones, L., Kipling, Z., Massart, S., Parrington, M., Peuch, V.-H., Razinger, M., Remy, S., Schulz, M., and Suttie, M.: The CAMS reanalysis of atmospheric composition, *Atmos. Chem. Phys. Discuss.*, <https://doi.org/10.5194/acp-2018-1078>, in review, 2018.
- Inoue, M., Morino, I., Uchino, O., Nakatsuru, T., Yoshida, Y., Yokota, T., Wunch, D., Wennberg, P. O., Roehl, C. M., Griffith, D. W. T., Velazco, V. A., Deutscher, N. M., Warneke, T., Notholt, J., Robinson, J., Sherlock, V., Hase, F., Blumenstock, T., Rettinger, M., Sussmann, R., Kyrö, E., Kivi, R., Shiomi, K., Kawakami, S., De Mazière, M., Arnold, S. G., Feist, D. G., Barrow, E. A., Barney, J., Dubey, M., Schneider, M., Iraci, L. T., Podolske, J. R., Hillyard, P. W., Machida, T., Sawa, Y., Tsuboi, K., Matsueda, H., Sweeney, C., Tans, P. P., Andrews, A. E., Biraud, S. C., Fukuyama, Y., Pittman, J. V., Kort, E. A., and Tanaka, T.: Bias corrections of GOSAT

- SWIR XCO<sub>2</sub> and XCH<sub>4</sub> with TCCON data and their evaluation using aircraft measurement data, *Atmos. Meas. Tech.*, 9, 3491-3512, <https://doi.org/10.5194/amt-9-3491-2016>, 2016.
- Iraci, L T and Podolske, J and Hillyard, P W and Roehl, C and Wennberg, P O and Blavier, J.-F. and Allen, N and Wunch, Debra and Osterman, Gregory B. and Albertson, R., TCCON data from Edwards (US), Release GGG2014R1, TCCON data archive, hosted by CaltechDATA, California Institute of Technology, Pasadena, CA, U.S.A. <https://doi.org/10.14291/tcon.ggg2014.edwards01.R1/1255068>, 2016.
- Kaiser, J., Heil, A., Andreae, M., Benedetti, A., Chubarova, N., Jones, L., Morcrette, J.-J., Razinger, M., and M. Suttie, M. S., and van der Werf, G.: Biomass burning emissions estimated with a global fire assimilation system based on observed fire radiative power, *Biogeosci.*, 9, 527–554, <https://doi.org/10.5194/bg-9-527-2012>, 2012.
- 10 Keeling, C. D., Bacastow, R. B., Bainbridge, A. E., Ekdahl, C. A., Guenther, P. R., Waterman, L. S. and Chin, J. F.: Atmospheric carbon dioxide variations at Mauna Loa Observatory, Hawaii. *Tellus*, 28: 538-551, <https://doi.org/10.1111/j.2153-3490.1976.tb00701.x>, 1976.
- Keppel-Aleks, G., Wennberg, P., and Schneider, T.: Sources of variations in total column carbon dioxide, *Atmos. Chem. Phys.*, 11, 3581–3593, <https://doi.org/10.5194/acp-11-3581-2011>, 2011.
- Keppel-Aleks, G., Wennberg, P. O., Washenfelder, R. A., Wunch, D., Schneider, T., Toon, G. C., Andres, R. J., Blavier, J.-F., Connor, B., 15 Davis, K. J., Desai, A. R., Messerschmidt, J., Notholt, J., Roehl, C. M., Sherlock, V., Stephens, B. B., Vay, S. A., and Wofsy, S. C.: The imprint of surface fluxes and transport on variations in total column carbon dioxide, *Biogeosciences*, 9, 875-891, <https://doi.org/10.5194/bg-9-875-2012>, 2012.
- Koehler, M., Ahlgrimm, M., and Beljaars, A.: Unified treatment of dry convective and stratocumulus-topped boundary layers in the ecmwf model, *Q.J.R. Meteorol. Soc.*, 137, 43–57, 2011.
- 20 Kuze, A., Suto, H., Nakajima, M. and Hamazaki, T.: Thermal and near infrared sensor for carbon observation Fourier-transform spectrometer on the Greenhouse Gases Observing Satellite for greenhouse gases monitoring, *Appl. Optics*, 48, 6716–6733, 2009.
- R.M. Law, L.P. Steele, P.B. Drummel, W. Zahorowski: Synoptic variations in atmospheric CO<sub>2</sub> at Cape Grim: a model intercomparison, *Tellus*, 62B, 810-820, 2010.
- R. M. Law, W. Peters, C. Rödenbeck, C. Aulagnier, I. Baker, D. J. Bergmann, P. Bousquet, J. Brandt, L. Bruhwiler, P. J. Cameron-Smith, 25 J. H. Christensen, F. Delage, A. S. Denning, S. Fan, C. Geels, S. Houweling, R. Imasu, U. Karstens, S. R. Kawa, J. Kleist, M. C. Krol, S.-J. Lin, R. Lokupitiya, T. Maki, S. Maksyutov, Y. Niwa, R. Onishi, N. Parazoo, P. K. Patra, G. Pieterse, L. Rivier, M. Satoh, S. Serrar, S. Taguchi, M. Takigawa, R. Vautard, A. T. Vermeulen, Z. Zhu: TransCom model simulations of hourly atmospheric CO<sub>2</sub>: Experimental overview and diurnal cycle results for 2002, *Global Biogeochem. Cycles*, 22, GB3009, <https://doi.org/10.1029/2007GB003050>, 2008.
- Lin, X., Ciais, P., Bousquet, P., Ramonet, M., Yin, Y., Balkanski, Y., Cozic, A., Delmotte, M., Evangeliou, N., Indira, N. K., Locatelli, R., Peng, S., Piao, S., Saunois, M., Swathi, P. S., Wang, R., Yver-Kwok, C., Tiwari, Y. K., and Zhou, L.: Simulating CH<sub>4</sub> and CO<sub>2</sub> over South and East Asia using the zoomed chemistry transport model LMDz-INCA, *Atmos. Chem. Phys.*, 18, 9475-9497, <https://doi.org/10.5194/acp-18-9475-2018>, 2018.
- 30 Lin, J. C., Mallia, D. V., Wu, D., and Stephens, B. B.: How can mountaintop CO<sub>2</sub> observations be used to constrain regional carbon fluxes?, *Atmos. Chem. Phys.*, 17, 5561-5581, <https://doi.org/10.5194/acp-17-5561-2017>, 2017.
- 35 Lin, Y.-L.: *Mesoscale Dynamics*. Cambridge University Press, Cambridge. <https://doi.org/10.1017/CBO9780511619649>, 2007.
- Locatelli, R., Bousquet, P., Chevallier, F., Fortems-Cheney, A., Szopa, S., Saunois, M., Agustí-Panareda, A., Bergmann, D., Bian, H., Cameron-Smith, P., Chipperfield, M., Gloor, E., Houweling, S., Kawa, S. R., Krol, M., Patra, P., Prinn, R., Rigby, M., Saito, R., and

- Wilson, C.: Impact of transport model errors on the global and regional methane emissions estimated by inverse modelling, *Atmos. Chem. Phys.*, 13, 9917–9937, <https://doi.org/10.5194/acp-13-9917-2013>, 2013.
- Loh, Z. M., R. M. Law, T. Ziehn, M. V. van der Schoot, P. B. Krummel, L. P. Steele, D. M. Etheridge, D. A. Spencer, R. L. Gregory, R. L. Langenfelds, A. R. Stavert, D. P. Thornton: The Australian Greenhouse Gas Observation Network: Current status and vision for the future. 10th International Carbon Dioxide Conference (ICDC10), 21-25 August 2017, Interlaken, Switzerland, [www.icdc10.unibe.ch/unibe/portal/fak\\_naturwis/micro\\_icdc10/content/e342182/e604227/e604229/files623284/Loh\\_Zoe.pdf](http://www.icdc10.unibe.ch/unibe/portal/fak_naturwis/micro_icdc10/content/e342182/e604227/e604229/files623284/Loh_Zoe.pdf), 2017.
- Lopez, M., M. Schmidt, M. Ramonet, J.-L. Bonne, A. Colomb, V. Kazan, P. Laj, and J.-M. Pichon, A gas chromatograph system for semi-continuous greenhouse gas measurements at Puy de Dome station, Central France, *Atmos. Meas. Tech. Discuss.*, 8, 3121-3170, 2015.
- Lu, R., R.P. Turco, Air pollutant transport in a coastal environment. Part I: Two dimensional simulations of sea-breeze and mountain effects, *J. Atmos. Sci.*, Vol. 51, No. 15, 2285-2308, 1994.
- Malardel, S., Wedi, N., Deconinck, W., Diamantakis, M., Kühnlein, C., Mozdzyński, G., Hamrud, M., Smolarkiewicz, P.: A new grid for the IFS, ECMWF Newsletter No. 146, <https://www.ecmwf.int/sites/default/files/elibrary/2016/15041-newsletter-no-146-winter-201516.pdf>, 2016.
- Massart, S., Agustí-Panareda, A., Heymann, J., Buchwitz, M., Chevallier, F., Reuter, M., Hilker, M., Burrows, J. P., Deutscher, N. M., Feist, D. G., Hase, F., Sussmann, R., Desmet, F., Dubey, M. K., Griffith, D. W. T., Kivi, R., Petri, C., Schneider, M., and Velasco, V. A.: Ability of the 4-D-Var analysis of the GOSAT BESD XCO<sub>2</sub> retrievals to characterize atmospheric CO<sub>2</sub> at large and synoptic scales, *Atmos. Chem. Phys.*, 16, 1653-1671, <https://doi.org/10.5194/acp-16-1653-2016>, 2016.
- Miller, C.E., D. Crisp, P.L. DeCola, S.C. Olsen, J.T. Randerson, A.M. Michalak, A. Alkhaled, P. Rayner, D.J. Jacob, P. Suntharalingam, D.B.A. Jones, A.S. Denning, M.E. Nicholls, S.C. Doney, S. Pawson, H. Boesch, B.J. Connor, I.Y. Fung, D.O'Brien, R.J. Salawitch, S.P. Sander, B. Sen, P. Tans, G.C. Toon, P.O. Wennberg, S.C. Wofsy, Y.L. Yung, R.M. Law: Precision requirements for space-based XCO<sub>2</sub> data, *J. Geophys. Res.*, 112, D10314, <https://doi.org/10.1029/2006JD007659>, 2007.
- Morcrette, J.-J., Boucher, O., Jones, L., Salmond, D., Bechtold, P., Beljaars, A., Benedetti, A., Bonet, A., Kaiser, J., Razinger, M., Schulz, M., Serrar, S., Simmons, A., Sofiev, M., Suttie, M., Tompkins, A., and Untch, A.: Aerosol analysis and forecast in the European Centre for Medium-Range Weather Forecasts Integrated Forecast System: forward modeling, *J. Geophys. Res.*, 114, D06206, <https://doi.org/10.1029/2008JD011235>, 2009.
- Morguí, J.A., A. Àgueda, O. Batet, R. Curcoll, M. Ealo, C. Grossi, P. Occhipinti, L. Sanchez-Garcia, R. Arias, and X. Rodo: ClimaDat: A long-term network to study at different scales climatic processes and interactions between climatic compartments, *Geophysical Research Abstract*, Vol. 15, page 10265, 2013.
- Morguí, J.A., R. Curcoll, A. Agustí-Panareda: Using the CLIMADAT atmospheric CO<sub>2</sub> dataset to evaluate (CAM5) the performance of a transport model over the Iberian Peninsula. 10th International Carbon Dioxide Conference (ICDC10) Theme 1.2: The contemporary carbon cycle – Emerging approaches and novel observation techniques, 21-25 August 2017, Interlaken, Switzerland, [www.icdc10.unibe.ch/unibe/portal/fak\\_naturwis/micro\\_icdc10/content/e342182/e588294/e591299/ICDC10\\_Abstracts\\_14082017.pdf](http://www.icdc10.unibe.ch/unibe/portal/fak_naturwis/micro_icdc10/content/e342182/e588294/e591299/ICDC10_Abstracts_14082017.pdf), 2017.
- Morino, I., N. Yokozeki, T. Matsumoto, A. Shishime. TCCON data from Rikubetsu, Hokkaido, Japan, Release GGG2014R1. TCCON data archive, hosted by CaltechDATA, California Institute of Technology, Pasadena, CA, U.S.A. <https://doi.org/10.14291/tcon.ggg2014.rikubetsu01.R1/1242265>, 2017.
- Morino, I., T. Matsumoto, A. Shishime. TCCON data from Tsukuba, Ibaraki, Japan, 125HR, Release GGG2014R1. TCCON data archive, hosted by CaltechDATA, California Institute of Technology, Pasadena, CA, U.S.A. <https://doi.org/10.14291/tcon.ggg2014.tsukuba02.R1/1241486>, 2014.

- Newman, S., Jeong, S., Fischer, M. L., Xu, X., Haman, C. L., Lefer, B., Alvarez, S., Rappenglueck, B., Kort, E. A., Andrews, A. E., Peischl, J., Gurney, K. R., Miller, C. E., and Yung, Y. L.: Diurnal tracking of anthropogenic CO<sub>2</sub> emissions in the Los Angeles basin megacity during spring 2010, *Atmos. Chem. Phys.*, 13, 4359-4372, <https://doi.org/10.5194/acp-13-4359-2013>, 2013.
- Newman, S., Xu, X., Gurney, K. R., Hsu, Y. K., Li, K. F., Jiang, X., Keeling, R., Feng, S., O’Keefe, D., Patarasuk, R., Wong, K. W., Rao, P., Fischer, M. L., and Yung, Y. L.: Toward consistency between trends in bottom-up CO<sub>2</sub> emissions and top-down atmospheric measurements in the Los Angeles megacity, *Atmos. Chem. Phys.*, 16, 3843-3863, <https://doi.org/10.5194/acp-16-3843-2016>, 2016.
- Notholt, J., C. Petri, T. Warneke, N. Deutscher, M. Buschmann, C. Weinzierl, R. Macatangay, P. Grupe. TCCON data from Bremen, Germany, Release GGG2014R0. TCCON data archive, hosted by CaltechDATA, California Institute of Technology, Pasadena, CA, U.S.A. <https://doi.org/10.14291/tcon.ggg2014.bremen01.R0/1149275>, 2014.
- 10 ObsPack (2015), Cooperative Global Atmospheric Data Integration Project; (2015): Multi-laboratory compilation of atmospheric carbon dioxide data for the period 1968-2014; `obspack_co2_1_GLOBALVIEWplus_v1.0_2015-07-30`; NOAA Earth System Research Laboratory, Global Monitoring Division. <http://dx.doi.org/10.15138/G3RP42>, 2015.
- O’Dell, C. W., Connor, B., Bösch, H., O’Brien, D., Frankenberg, C., Castano, R., Christi, M., Eldering, D., Fisher, B., Gunson, M., McDuffie, J., Miller, C. E., Natraj, V., Oyafuso, F., Polonsky, I., Smyth, M., Taylor, T., Toon, G. C., Wennberg, P. O., and Wunch, D.: The ACOS CO<sub>2</sub> retrieval algorithm – Part 1: Description and validation against synthetic observations, *Atmos. Meas. Tech.*, 5, 99–121, <https://doi.org/10.5194/amt-5-99-2012>, 2012.
- 15 Olivier and G. Janssens-Maenhout, CO<sub>2</sub> Emissions from Fuel Combustion – 2012 Edition, IEA CO<sub>2</sub> report 2012, Part III, Greenhouse-Gas Emissions, ISBN 978-92-64-17475-7. [http://edgar.jrc.ec.europa.eu/news\\_docs/jrc-2015-trends-in-global-CO2-emissions-2015-report-98184.pdf](http://edgar.jrc.ec.europa.eu/news_docs/jrc-2015-trends-in-global-CO2-emissions-2015-report-98184.pdf), 2015.
- 20 Olsen, S. C., and J. T. Randerson, Differences between surface and column atmospheric CO<sub>2</sub> and implications for carbon cycle research, *J. Geophys. Res.*, 109, D02301, <https://doi.org/10.1029/2003JD003968>, 2004.
- Ott, L.E., S. Pawson, G.J. Collatz, W.W. Gregg, D. Menemenlis, H. Brix, C.S. Rousseaux, K.W. Bowman, J. Liu, A. Eldering, M.R. Gunson, S.R. Kawa, Assessing the magnitude of CO<sub>2</sub> flux uncertainty in atmospheric CO<sub>2</sub> records using products from NASA’s Carbon Monitoring Flux Pilot Project, *J. Geophys. Res. Atmos.*, 120, 734–765, doi:10.1002/2014JD022411.
- 25 Parazoo, N. C., A. S. Denning, J. A. Berry, A. Wolf, D. A. Randall, S. R. Kawa, O. Pauluis, and S. C. Doney, Moist synoptic transport of CO<sub>2</sub> along the mid-latitude storm track, *Geophys. Res. Lett.*, 38, L09804, <https://doi.org/10.1029/2011GL047238>, 2011.
- Patra, P. K., Law, R. M., Peters, W., Rödenbeck, C., Takigawa, M. and co-authors: Transcom model simulations of hourly atmospheric CO<sub>2</sub> : analysis of synoptic scale variations for the period 2002-2003. *Global Biogeochem. Cycles* 22, GB4013, <https://doi.org/10.1029/2007GB003081>, 2008.
- 30 Peterson, J.T., W.D. Komhyr, L.S. Waterman, R.H. Gammon, K.W. Thoning, and T.J. Conway, Atmospheric CO<sub>2</sub> variations at Barrow, Alaska, 1973 1982, *J. Atmos. Chem.*, 4, 491 510, 1986.
- Pillai, D., Gerbig, C., Marshall, J., Ahmadov, R., Kretschmer, R., Koch, T., and Karstens, U.: High resolution modeling of CO<sub>2</sub> over Europe: implications for representation errors of satellite retrievals, *Atmos. Chem. Phys.*, 10, 83-94, <https://doi.org/10.5194/acp-10-83-2010>, 2010.
- Pillai, D., Gerbig, C., Ahmadov, R., Rödenbeck, C., Kretschmer, R., Koch, T., Thompson, R., Neining, B., and Lavrié, J. V.: High-resolution simulations of atmospheric CO<sub>2</sub> over complex terrain – representing the Ochsenkopf mountain tall tower, *Atmos. Chem. Phys.*, 11, 7445-7464, <https://doi.org/10.5194/acp-11-7445-2011>, 2011.

- Polavarapu, S., Neish, M., Tanguay, M., Girard, C., Granpré, J. D., Semeniuk, K., Gravel, S., Ren, S., Roche, S., Chan, D., and Strong, K. Greenhouse gas simulations with a coupled meteorological and transport model: the predictability of CO<sub>2</sub>, *Atmos. Chem. Phys.*, 16, 12005-12038, <https://doi.org/10.5194/acp-16-12005-2016>, 2016.
- Michael J. Prather, Xin Zhu, Susan E. Strahan, Stephen D. Steenrod, Jose M. Rodriguez: Quantifying errors in trace species transport modeling. *Proceedings of the National Academy of Sciences*, 105 (50) 19617-19621; <https://doi.org/10.1073/pnas.0806541106>, 2008.
- Rabier, F., Järvinen, H., Klinker, E., Mahfouf, J.-F., Simmons, A.: The ECMWF operational implementation of four-dimensional variational assimilation. part I: Experimental results with simplified physics, *Q. J. Roy. Meteor. Soc.*, 126, 1143–1170, 2000.
- Ramonet, M., P. Ciais, T. Aalto, C. Aulagnier, F. Chevallier, D. Cipriano, T.J. Conway, L. Haszpra, V. Kazan, F. Meinhardt, J.-D. Paris, M. Schmidt, P. Simmonds, I. Xueref-Remy, and J. Necki, A recent build-up of atmospheric CO<sub>2</sub> over Europe. Part I: observed signals and possible explanations, *Tellus B*, <https://doi.org/10.1111/j.1600-0889.2009.00442>, 2010.
- Rayner, P. J., Scholze, M., Knorr, W., Kaminski, T., Giering, R., Widmann, H.: Two decades of terrestrial carbon fluxes from a carbon cycle data assimilation system (CCDAS), *Glob. Biogeochem. Cycle* 19, GB2026, <https://doi.org/10.1029/2004GB002254>, 2005.
- Remaud, M., Chevallier, F., Cozic, A., Lin, X., and Bousquet, P.: On the impact of recent developments of an atmospheric general circulation model on the simulation of CO<sub>2</sub> transport, *Geosci. Model Dev. Discuss.*, <https://doi.org/10.5194/gmd-2018-164>, in review, 2018.
- 15 Rozanski, K., Zimnoch, M., Korus, A., Lasa, J., Graul, R., Levin, I. Six-year record of atmospheric carbon dioxide and methane at a high-altitude mountain site in Poland. *Tellus*, 55B: 94-104, 2003.
- Rozanski K., Necki J., Chmura L., Sliwka I., Zimnoch M., Bielewski J., Galkowski M., Bartyzel J., Rosiek J. Anthropogenic changes of CO<sub>2</sub>, CH<sub>4</sub>, N<sub>2</sub>O, CFC1<sub>3</sub>, CF<sub>2</sub>Cl<sub>2</sub>, CCl<sub>2</sub>FCClF<sub>2</sub>, CHCl<sub>3</sub>, CH<sub>3</sub>CCl<sub>3</sub>, CCl<sub>4</sub>, SF<sub>6</sub> and SF<sub>5</sub>CF<sub>3</sub> mixing ratios in the atmosphere over southern Poland. *Geological Quarterly*, Vol 58, No 4 673-684, 2014.
- 20 Sandu, I., Beljaars, A., Bechtold, P., Mauritsen, T., and Balsamo, G.: Why is it so difficult to represent stably stratified conditions in numerical weather prediction (NWP) models?, *Journal of Advances in Modeling Earth Systems*, 5, 1–17, <https://doi.org/10.1002/jame.20013>, 2013.
- Schibig, M. F., Steinbacher, M., Buchmann, B., van der Laan-Luijkx, I. T., van der Laan, S., Ranjan, S., and Leuenberger, M. C.: Comparison of continuous in situ CO<sub>2</sub> observations at Jungfraujoch using two different measurement techniques, *Atmos. Meas. Tech.*, 8, 57-68, <https://doi.org/10.5194/amt-8-57-2015>, 2015.
- 25 Schmidt, M., Graul, R., Sartorius, H., and Levin, L.: The Schauinsland CO<sub>2</sub> record: 30 years of continental observations and their implications for the variability of the European CO<sub>2</sub> budget, *J. Geophys. Res.-Atmos.*, 108, 4619-4626, 2003.
- Sekiyama, T., Kunii, M., Kajino, M., Shimbori, T. (2015). Horizontal Resolution Dependence of Atmospheric Simulations of the Fukushima Nuclear Accident Using 15-km, 3-km, and 500-m Grid Models. *Journal of the Meteorological Society of Japan. Ser. II.* 93. 49-64, <https://doi.org/10.2151/jmsj.2015-002>.
- 30 Sherlock, V., B. Connor, J. Robinson, H. Shiona, D. Smale, D. Pollard. TCCON data from Lauder, New Zealand, 120HR, Release GGG2014R0. TCCON data archive, hosted by CaltechDATA, California Institute of Technology, Pasadena, CA, U.S.A. <https://doi.org/10.14291/tcon.ggg2014.lauder01.R0/1149293>, 2014.
- Shiomi, K., Kawakami, S., H. Ohyama, K. Arai, H. Okumura, C. Taura, T. Fukamachi, M. Sakashita. TCCON data from Saga, Japan, Release GGG2014R0. TCCON data archive, hosted by CaltechDATA, California Institute of Technology, Pasadena, CA, U.S.A. <https://doi.org/10.14291/tcon.ggg2014.saga01.R0/1149283>, 2014.
- 35 Stavert, A. R., Law, R. M., van der Schoot, M., Langenfelds, R. L., Spencer, D. A., Krummel, P. B., Chambers, S. D., Williams, A. G., Werczynski, S., Francey, R. J., and Howden, R. T.: The Macquarie Island (LoFlo2G) high-precision continuous atmospheric carbon dioxide record, *Atmos. Meas. Tech.*, 12, 1103-1121, <https://doi.org/10.5194/amt-12-1103-2019>, 2019.

- Stephens, B.B., Miles, N.L., Richardson, S.J., Watt, S., Davis, K.J.: Atmospheric CO<sub>2</sub> monitoring with single-cell NDIR-based analyzers, *Atmos. Meas. Tech.*, 4, 2737-2748, <https://doi.org/10.5194/amt-4-2737-2011>, 2011.
- Sussmann, R., M. Rettinger. TCCON data from Garmisch, Germany, Release GGG2014R0. TCCON data archive, hosted by CaltechDATA, California Institute of Technology, Pasadena, CA, U.S.A.<https://doi.org/10.14291/tccon.ggg2014.garmisch01.R0/1149299>, 2014.
- 5 Takahashi, T., S. C. Sutherland, R. Wanninkhof, C. Sweeney, R. A. Feely, D. W. Chipman, B. Hales, G. Friederich, F. Chavez, A. Watson, D. C. E. Bakker, U. Schuster, N. Metzl, H. Yoshikawa-Inoue, M. Ishii, T. Midorikawa, Y. Nojiri, C. Sabine, J. Olafsson, Th. S. Arnarson, B. Tilbrook, T. Johannessen, A. Olsen, Richard Bellerby, A. Körtzinger, T. Steinhoff, M. Hoppema, H. J. W. de Baar, C. S. Wong, Bruno Delille and N. R. Bates. Climatological mean and decadal changes in surface ocean pCO<sub>2</sub>, and net sea-air CO<sub>2</sub> flux over the global oceans. *Deep-Sea Res. II*, 56, 554-577, 2009.
- 10 Tang, W., Arellano, A. F., DiGangi, J. P., Choi, Y., Diskin, G. S., Agustí-Panareda, A., Parrington, M., Massart, S., Gaubert, B., Lee, Y., Kim, D., Jung, J., Hong, J., Hong, J.-W., Kanaya, Y., Lee, M., Stauffer, R. M., Thompson, A. M., Flynn, J. H., and Woo, J.-H.: Evaluating high-resolution forecasts of atmospheric CO and CO<sub>2</sub> from a global prediction system during KORUS-AQ field campaign, *Atmos. Chem. Phys.*, 18, 11007-11030, <https://doi.org/10.5194/acp-18-11007-2018>, 2018.
- Temperton, C., Hortal, M., and Simmons, A.: A two-time-level semi-Lagrangian global spectral model, *Q.J.R. Meteorol. Soc.*, 127, 111–126,  
15 2001.
- Thoning, K.W., P.P. Tans, and W.D. Komhyr, Atmospheric carbon dioxide at Mauna Loa Observatory, 2. Analysis of the NOAA/GMCC data, 1974 1985., *J. Geophys. Res.*, 94, 8549 8565, 1989.
- Tiedtke, M.: A comprehensive mass flux scheme for cumulus parameterization in large-scale models, *Mon. Wea. Rev.*, 117, 1779–1800, 1989.
- 20 Tolk, L. F., Meesters, A. G. C. A., Dolman, A. J., and Peters, W.: Modelling representation errors of atmospheric CO<sub>2</sub> mixing ratios at a regional scale, *Atmos. Chem. Phys.*, 8, 6587–6596, 2008, [www.atmos-chem-phys.net/8/6587/2008/](http://www.atmos-chem-phys.net/8/6587/2008/).
- Tsutsumi, Y., H. Matsueda, S. Nishioka, Consistency of the CO<sub>2</sub> primary standards in JMA, 12th WMO/IAEA meeting of experts on carbon dioxide concentration and related tracers measurement techniques (Toronto, Canada, 15-18 September 2003), *Global Atmosphere Watch Report No. 161 (WMO/TD-No.1275)*, 23-31, 2005.
- 25 van der Molen, M. K., and A. J. Dolman, Regional carbon fluxes and the effect of topography on the variability of atmospheric CO<sub>2</sub>, *J. Geophys. Res.*, 112, D01104, <https://doi.org/10.1029/2006JD007649>, 2007.
- Verhulst, K. R., Karion, A., Kim, J., Salameh, P. K., Keeling, R. F., Newman, S., Miller, J., Sloop, C., Pongetti, T., Rao, P., Wong, C., Hopkins, F. M., Yadav, V., Weiss, R. F., Duren, R. M. and Miller, C. E.: Carbon dioxide and methane measurements from the Los Angeles Megacity Carbon Project – Part 1: calibration, urban enhancements, and uncertainty estimates, *Atmos. Chem. Phys.*, 17(13), 8313–8341,  
30 <https://doi.org/10.5194/acp-17-8313-2017>, 2017.
- Vermeulen, A. T., Hensen, A., Popa, M. E., van den Bulk, W. C. M., and Jongejan, P. A. C.: Greenhouse gas observations from Cabauw Tall Tower (1992-2010), *Atmos. Meas. Tech.*, 4, 617-644, <https://doi.org/10.5194/amt-4-617-2011>, 2011.
- Vogel, F.R., Thiruchittampalam, B., Theloke, J., Kretschmer, R., Gerbig, C., Hammer, S. and Levin, I.: Can we assess a fine-grained emission model using high-resolution atmospheric transport modeling and regional fossil fuel CO<sub>2</sub> observations? *Tellus 65B*,  
35 18681,<https://doi.org/10.3402/tellusb.v65i0.18681>, 2013.
- Wang, J. S., Kawa, S. R., Collatz, G. J., Sasakawa, M., Gatti, L. V., Machida, T., Liu, Y., and Manyin, M. E.: A global synthesis inversion analysis of recent variability in CO<sub>2</sub> fluxes using GOSAT and in situ observations, *Atmos. Chem. Phys.*, 18, 11097-11124, <https://doi.org/10.5194/acp-18-11097-2018>, 2018.

- Warneke, T., J. Messerschmidt, J. Notholt, C. Weinzierl, N. Deutscher, C. Petri, P. Grupe, C. Vuillemin, F. Truong, M. Schmidt, M. Ramonet, E. Parmentier: TCCON data from Orleans, France, Release GGG2014R0. TCCON data archive, hosted by CaltechDATA, California Institute of Technology, Pasadena, CA, U.S.A. <https://doi.org/10.14291/tccon.ggg2014.orleans01.R0/1149276>, 2014.
- Wedi N.P.: Increasing horizontal resolution in numerical weather prediction and climate simulations: illusion or panacea? *Phil. Trans. R. Soc. A* 372: 20130289. <https://doi.org/10.1098/rsta.2013.0289>, 2014.
- 5 Wennberg, P. O., D. Wunch, C. Roehl, J.-F. Blavier, G. C. Toon, N. Allen, P. Dowell, K. Teske, C. Martin, J. Martin: TCCON data from Lamont, Oklahoma, USA, Release GGG2014R1. TCCON data archive, hosted by CaltechDATA, California Institute of Technology, Pasadena, CA, U.S.A. <https://doi.org/10.14291/tccon.ggg2014.lamont01.R1/1255070>, 2016.
- Wennberg, P. O., D. Wunch, C. Roehl, J.-F. Blavier, G. C. Toon, N. Allen: TCCON data from California Institute of Technology, Pasadena, California, USA, Release GGG2014R1. TCCON data archive, hosted by CaltechDATA, California Institute of Technology, Pasadena, CA, U.S.A. <https://doi.org/10.14291/tccon.ggg2014.pasadena01.R1/1182415>, 2014.
- 10 Wennberg, P. O., C. Roehl, D. Wunch, G. C. Toon, J.-F. Blavier, R. Washenfelder, G. Keppel-Aleks, N. Allen, J. Ayers: TCCON data from Park Falls, Wisconsin, USA, Release GGG2014R1. TCCON data archive, hosted by CaltechDATA, California Institute of Technology, Pasadena, CA, U.S.A. <https://doi.org/10.14291/tccon.ggg2014.parkfalls01.R0/1149161>, 2014.
- 15 Wilson, P. A., Insight into the Carbon Cycle from Continuous Measurements of Oxygen and Carbon Dioxide at Weybourne Atmospheric Observatory, UK, Ph.D. thesis, University of East Anglia, Norwich, U.K., 2013.
- Worthy, D.E., K.Higuchi, and D. Chan: North American influence on atmospheric carbon dioxide data collected at Sable Island, Canada. *Tellus* 55B, 105-114, 2003.
- Wunch, D., P. O. Wennberg, G. C. Toon, G. Keppel-Aleks, and Y. G. Yavin: Emissions of greenhouse gases from a North American megacity, *Geophys. Res. Lett.*, 36, L15810, <https://doi.org/10.1029/2009GL039825>, 2009.
- 20 Wunch, D., Toon, G. C., Blavier, J.-F. L., Washenfelder, R. A., Notholt, J., Connor, B., Griffith, D. W. T., Sherlock, V., , and Wennberg, P. O.: The total carbon column observing network, *Phil. Trans. R. Soc. A*, 369, 2087–2112, <https://doi.org/10.1098/rsta.2010.0240>, 2011.
- Wunch D., Wennberg P. O., Osterman G., Fisher B., Naylor B., Roehl C. M., O'Dell C., Mandrake L., Viatte C., Kiel M., Griffith D. W. T., Deutscher N. M., Velazco V. A., Notholt J., Warneke T., Petri C., De Maziere M., Sha M. K., Sussmann R., Rettinger M., Pollard D.,
- 25 Robinson J., Morino I., Uchino O., Hase F., Blumenstock T., Feist D. G., Arnold S. G., Strong K., Mendonca J., Kivi R., Heikkinen P., Iraci L., Podolske J., Hillyard P. W., Kawakami S., Dubey M. K., Parker H. A., Sepulveda E., García O. E., Te Y., Jeseck P., Gunson M. R., Crisp D., Eldering A, Comparisons of the Orbiting Carbon Observatory-2 (OCO-2) XCO<sub>2</sub> measurements with TCCON, *Atmos. Meas. Tech.*, 10, 2209–2238, <https://doi.org/10.5194/amt-10-2209-2017>, 2017.
- Xueref-Remy, I., Dieudonné, E., Vuillemin, C., Lopez, M., Lac, C., Schmidt, M., Delmotte, M., Chevallier, F., Ravetta, F., Perrussel, O.,
- 30 Ciais, P., Bréon, F.-M., Broquet, G., Ramonet, M., Spain, T. G., and Ampe, C.: Diurnal, synoptic and seasonal variability of atmospheric CO<sub>2</sub> in the Paris megacity area, *Atmos. Chem. Phys.*, 18, 3335-3362, <https://doi.org/10.5194/acp-18-3335-2018>, 2018.
- Yang, D. X., Y. Liu, Z. N. Cai, X. Chen, L. Yao, and D. R. Lu: First global carbon dioxide maps produced from TanSat measurements. *Adv. Atmos. Sci.*, 35(6), 621–623, <https://doi.org/10.1007/s00376-018-7312-6>, 2018.
- Ye, X., Lauvaux, T., Kort, E. A., Oda, T., Feng, S., Lin, J. C., Yang, E., and Wu, D.: Constraining fossil fuel CO<sub>2</sub> emissions from urban area using OCO-2 observations of total column CO<sub>2</sub>, *Atmos. Chem. Phys. Discuss.*, <https://doi.org/10.5194/acp-2017-1022>, in review, 2017.
- 35 Yu, K., Keller, C. A., Jacob, D. J., Molod, A. M., Eastham, S. D., and Long, M. S.: Errors and improvements in the use of archived meteorological data for chemical transport modeling: an analysis using GEOS-Chem v11-01 driven by GEOS-5 meteorology, *Geosci. Model Dev.*, 11, 305-319, <https://doi.org/10.5194/gmd-11-305-2018>, 2018.

## Supplementary Material

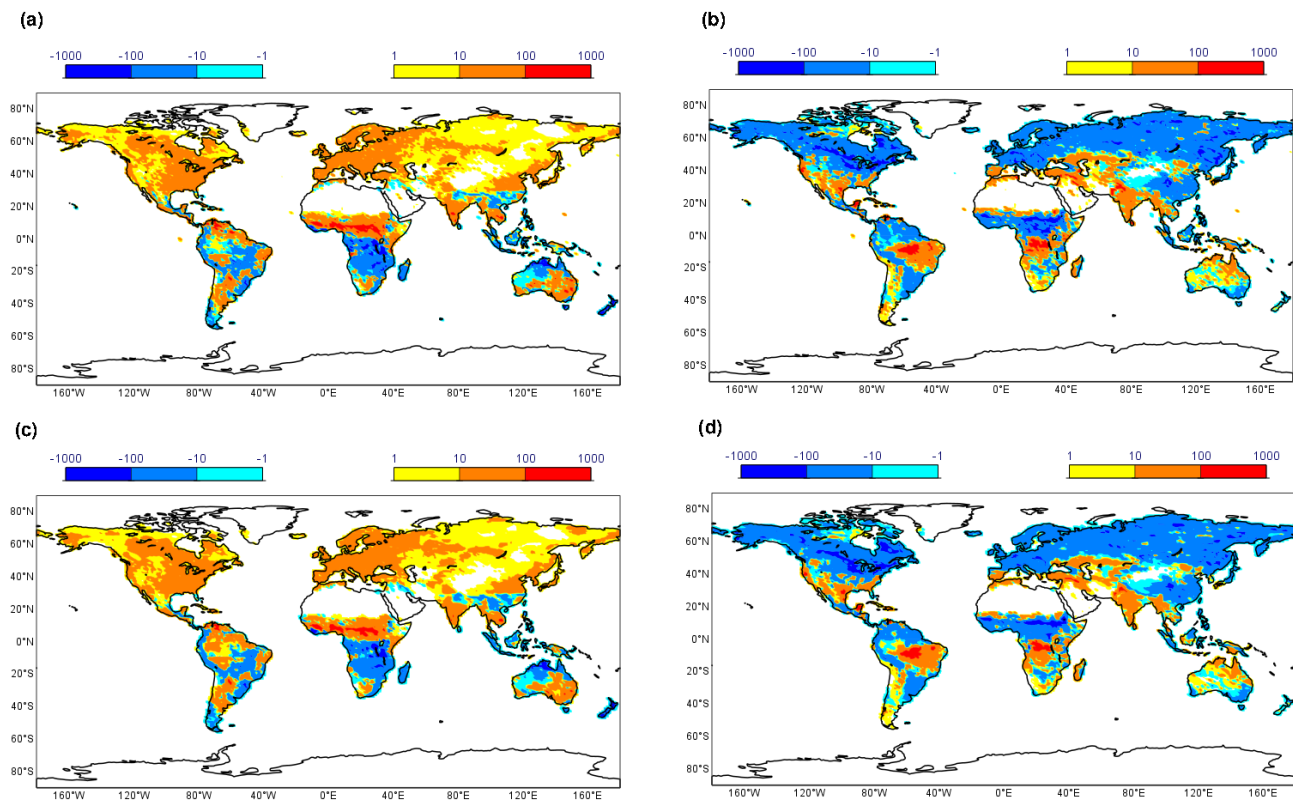


**Figure S1.** Monthly mean NEE [ $\text{g m}^{-2} \text{day}^{-1}$ ] from the 9km-EXP (upper panels) and the 80km-EXP (lower panels) simulations in January (a,c) and August (b,d). The difference between the NEE global budget of 9km-EXP and 80km-EXP is less than 1 %.

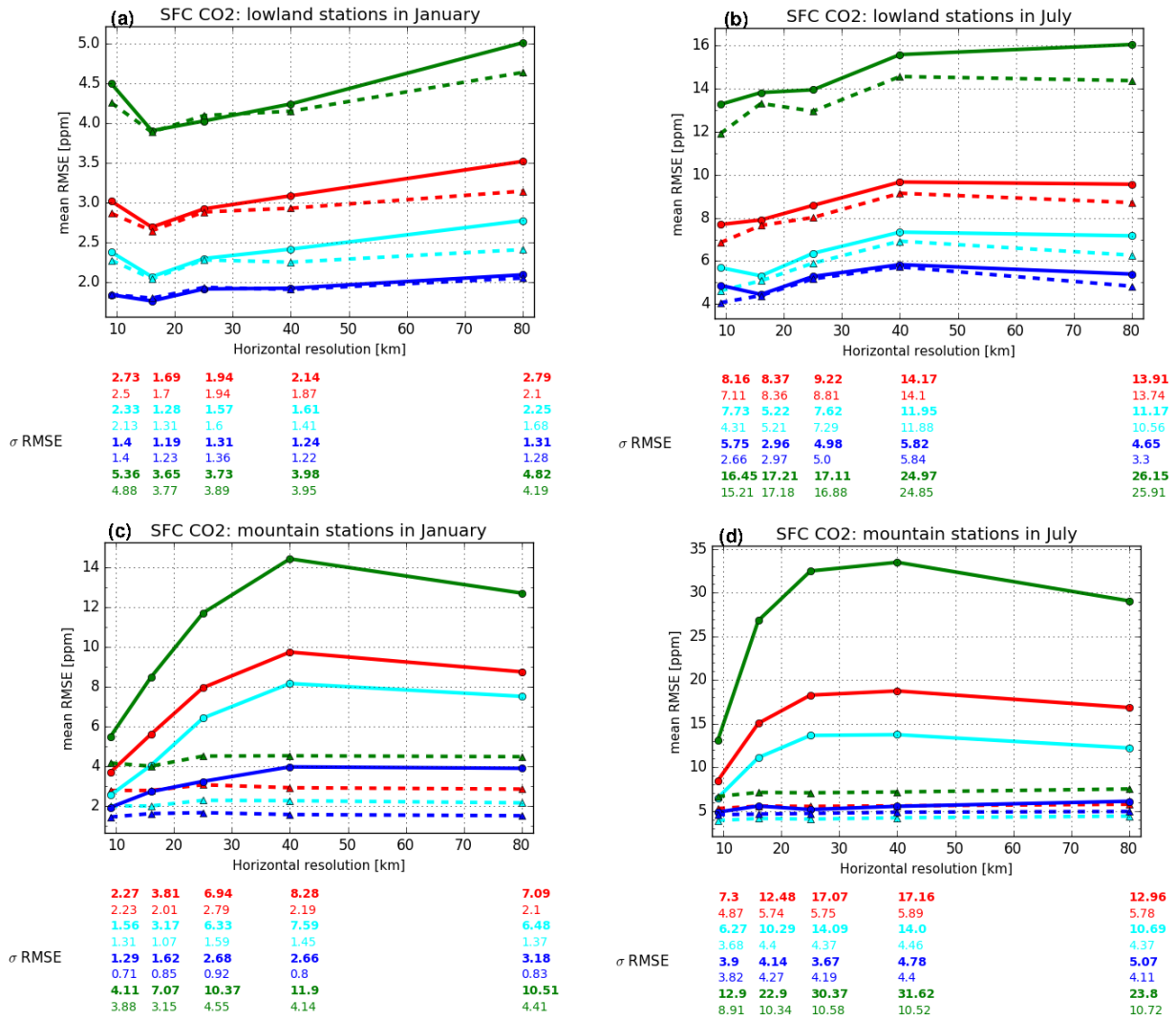


**Figure S2.** As in Fig. 6, using the different vertical sampling of the model with height above ground (solid lines) and height above mean sea level (dash lines). The standard deviation of the RMSE from each station is shown by the numbers below are in bold/non-bold for the height above ground/height above mean sea level. Note that different scales are used in each panel.

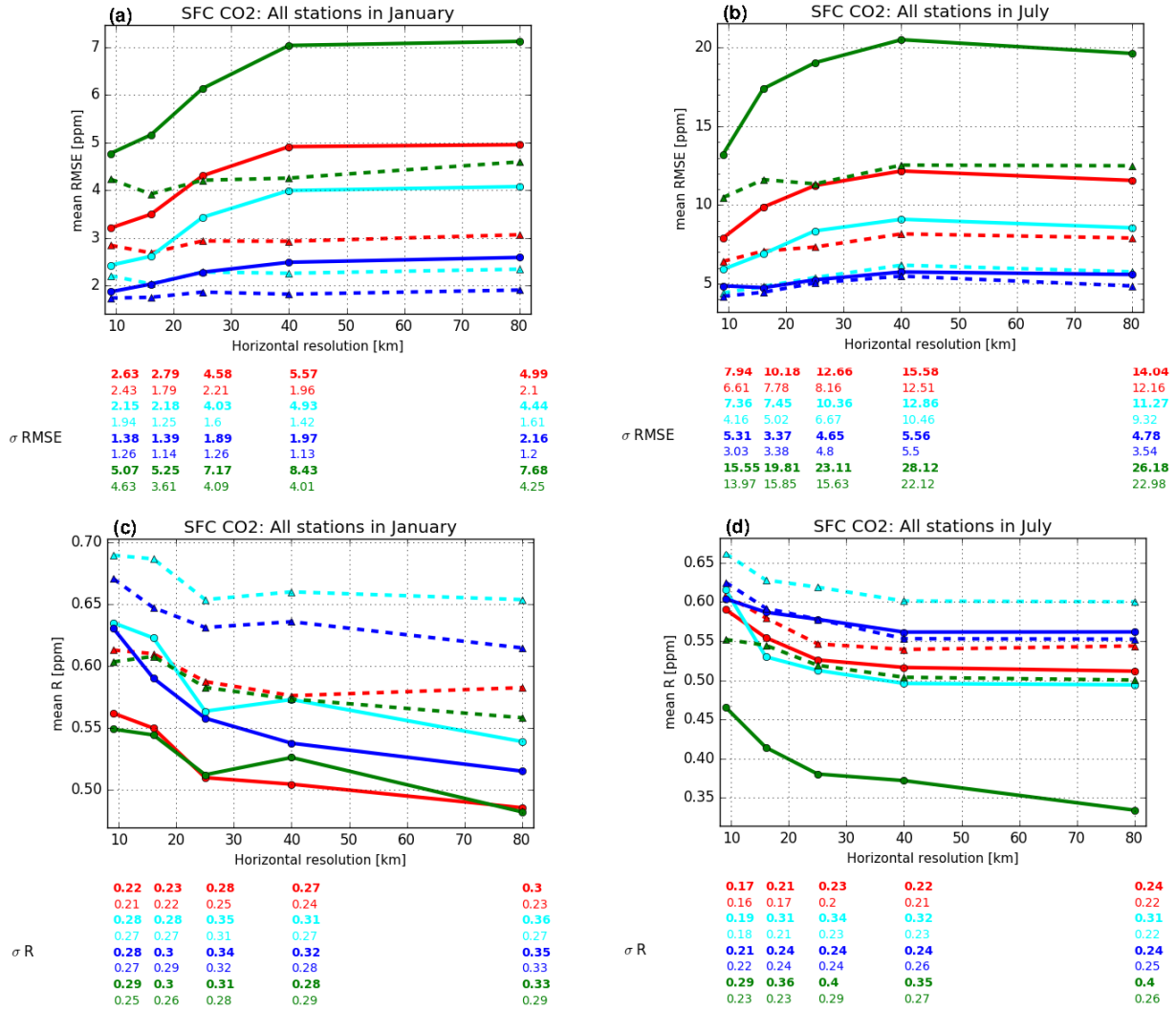


**Figure S3.** As in Fig. 5, using different vertical sampling of the model with height above ground (solid lines) and height above mean sea level (dash lines). The standard deviation of the RMSE from each station is shown by the numbers below are in bold/non-bold for the height above ground/height above mean sea level. Note that different scales are used in each panel.

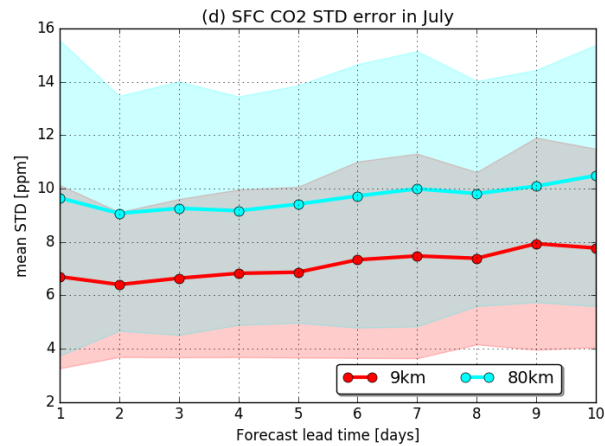
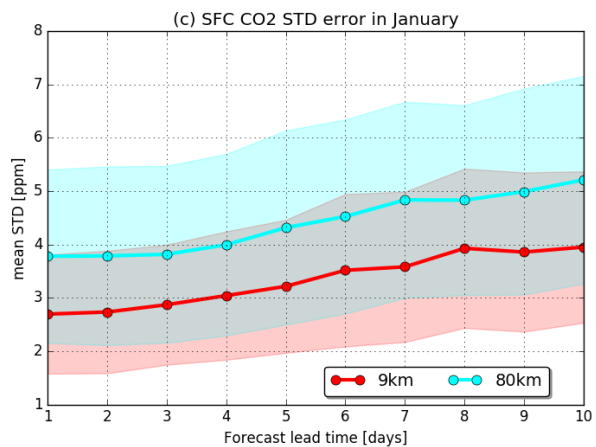
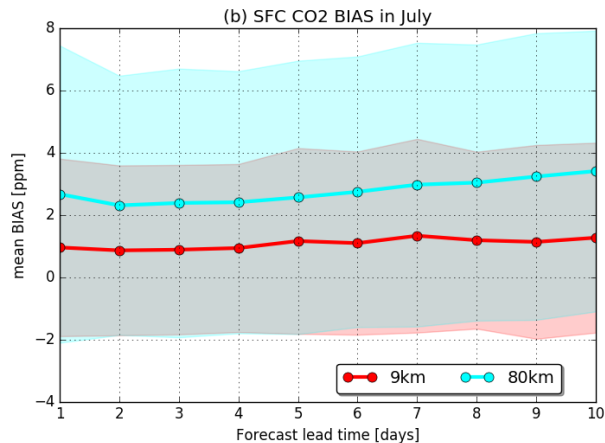
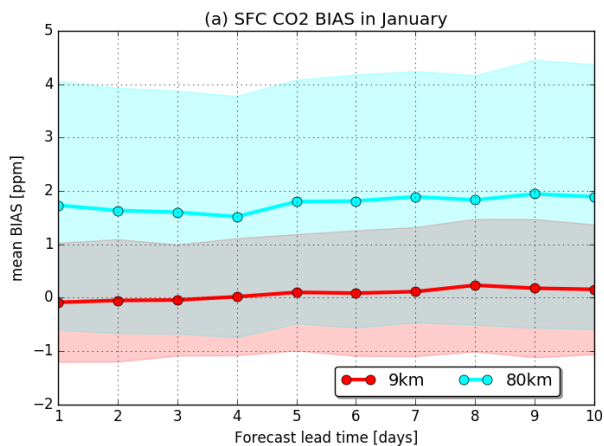


**Figure S4.** (a,b) Mean bias and (c,d) standard error of near-surface CO<sub>2</sub> at different forecast lead times for 9km-EXP (red) and 80km-EXP (blue) in (a,c,d) January and (b,d,f) July. The errors are computed with respect to continuous in situ surface measurements from 51 stations (see Tab A1). The error standard deviation between the different stations is shown with the shaded area. Note that different scales are used in each panel.

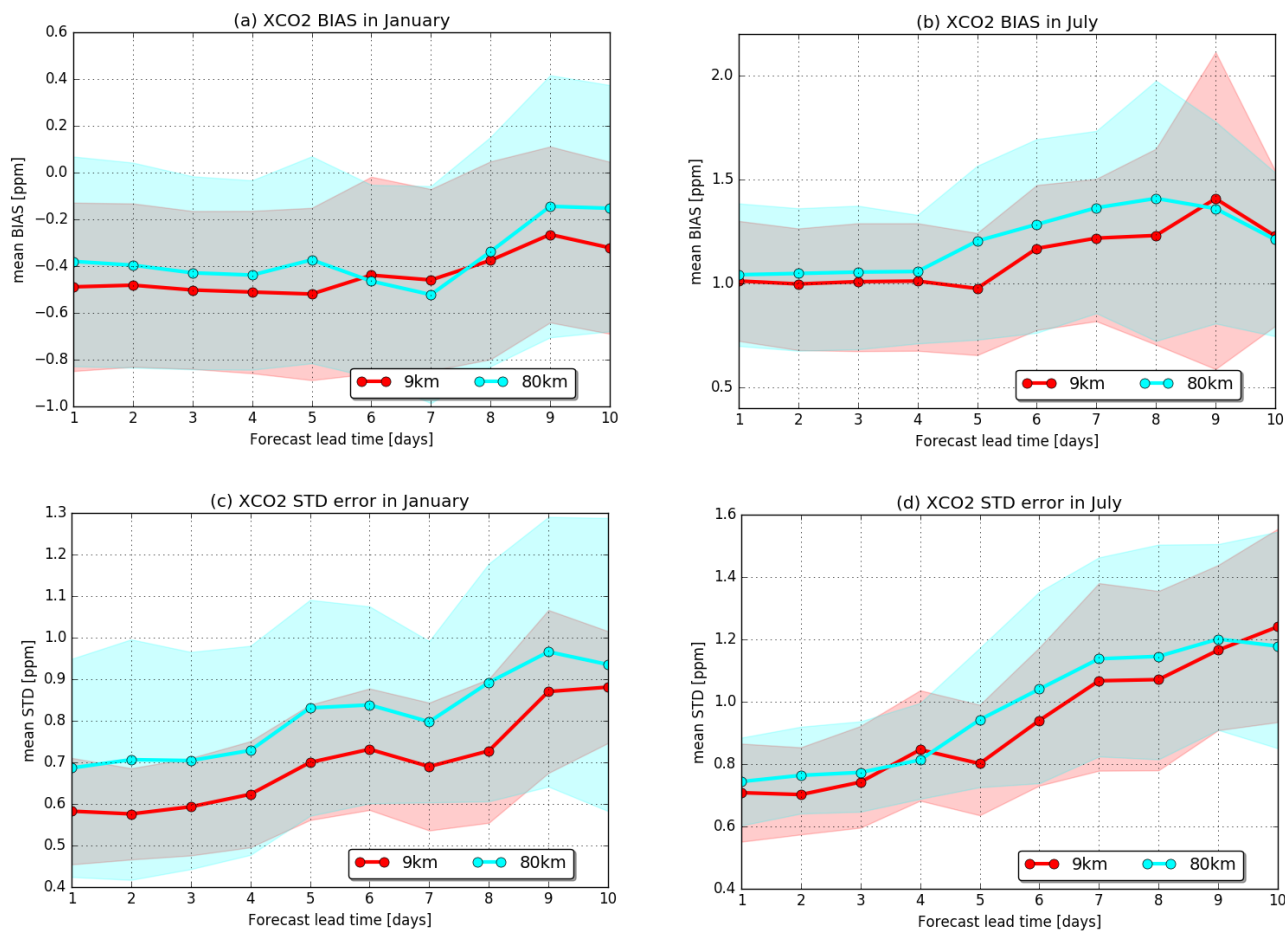


**Figure S5.** (a,b) Mean bias and (c,d) standard error of XCO<sub>2</sub> at different forecast lead times for 9km-EXP (red) and 80km-EXP (blue) in (a,c,d) January and (b,d,f) July. The errors are computed with respect to TCCON observations from 18 TCCON stations (see Tab. A3). The error standard deviation between the different stations is shown with the shaded area. Note that different scales are used in each panel.

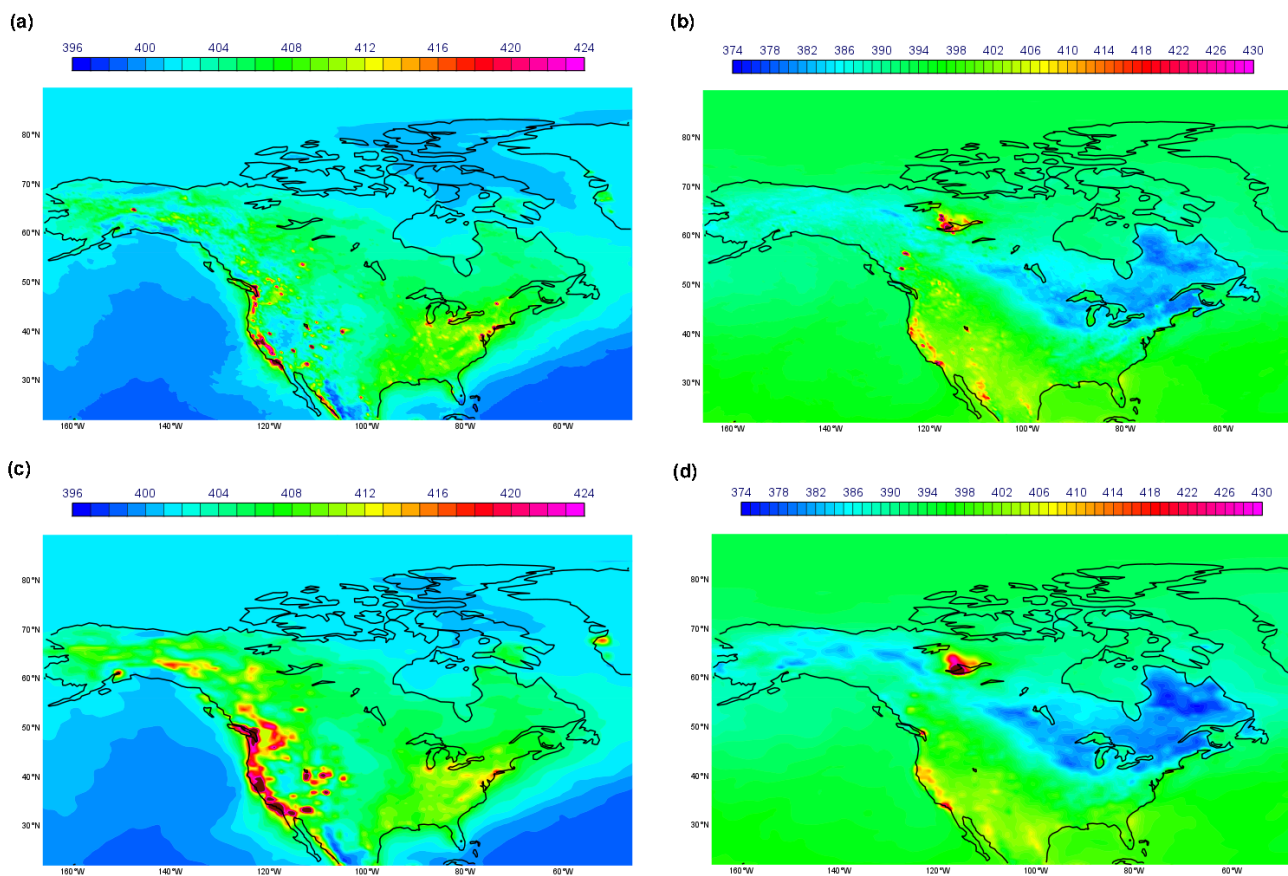


**Figure S6. Monthly mean surface CO<sub>2</sub> [ppm] from 9km-EXP (a,b) and 80km-EXP (c,d) simulations over North America at 18 UTC in January (left panels) and July (right panels). Values larger than 424 ppm and 430 ppm in winter and summer respectively are shown in brown.**

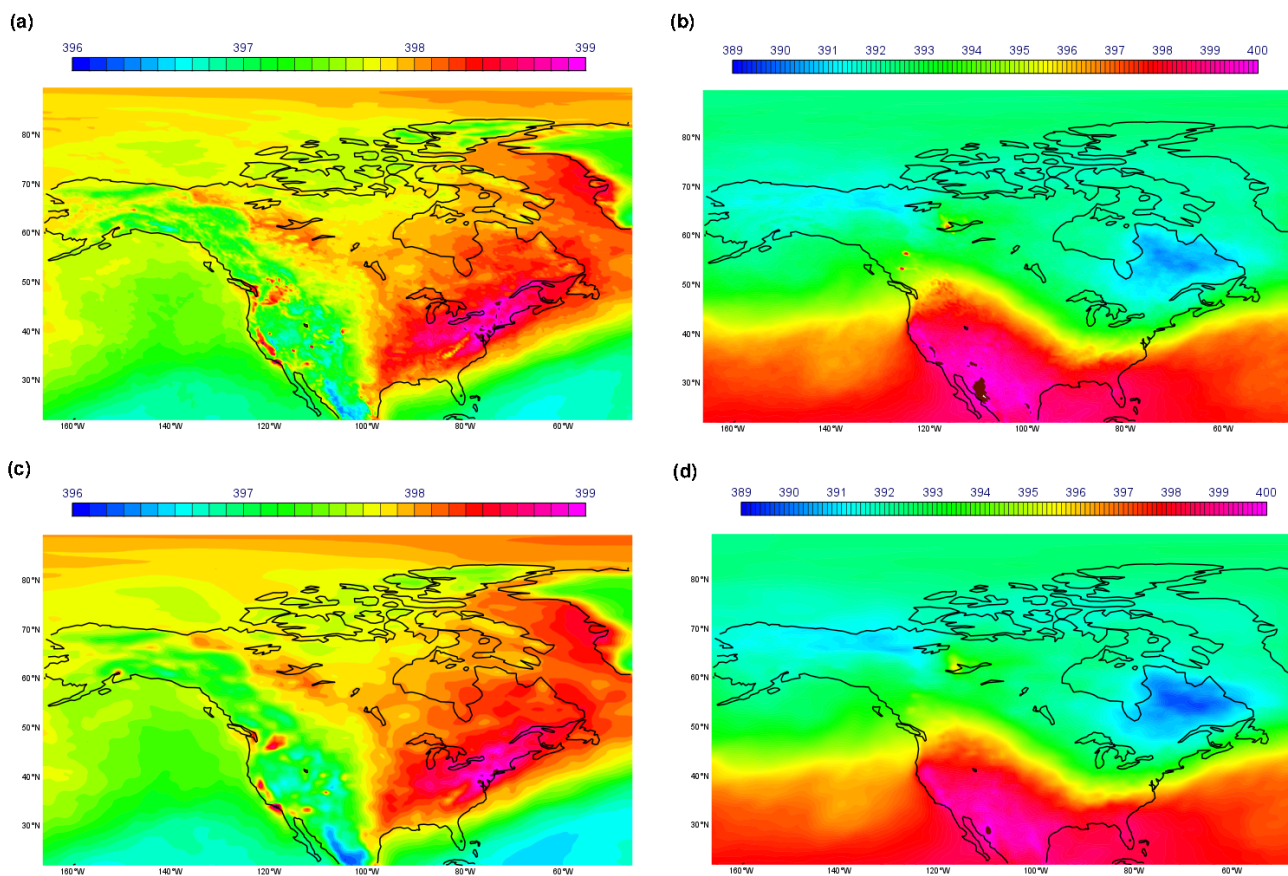


**Figure S7.** Monthly mean XCO<sub>2</sub> [ppm] at the surface from 9km-EXP (a,b) and 80km-EXP (c,d) simulations over North America at 18 UTC in January (left panels) and July (right panels). Values larger than 399 ppm and 400 ppm in winter and summer respectively are shown in brown.

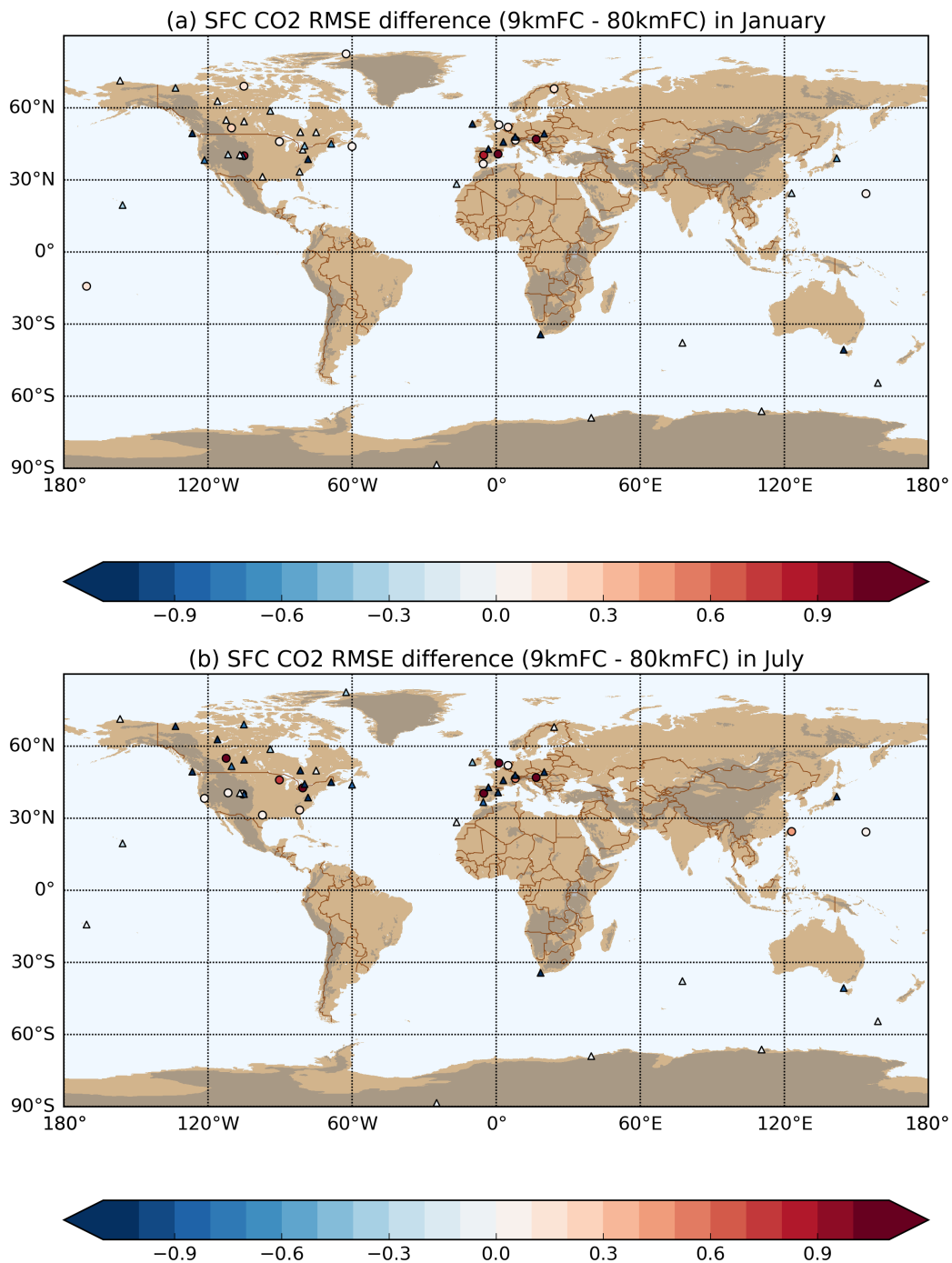


**Figure S8.** Difference in near-surface CO<sub>2</sub> RMSE [ppm] between highest and lowest resolution simulations (9km-EXP – 80km-EXP) in (a) January and (b) July at surface stations. Triangles indicate an RMSE reduction (blue colours) and circles an RMSE increase (red colours) as shown by the colour bar. Mountain regions with elevation > 1000 m above sea level are shaded in grey. The statistics for each station are listed Tabs S1 and S2 for January and July respectively.

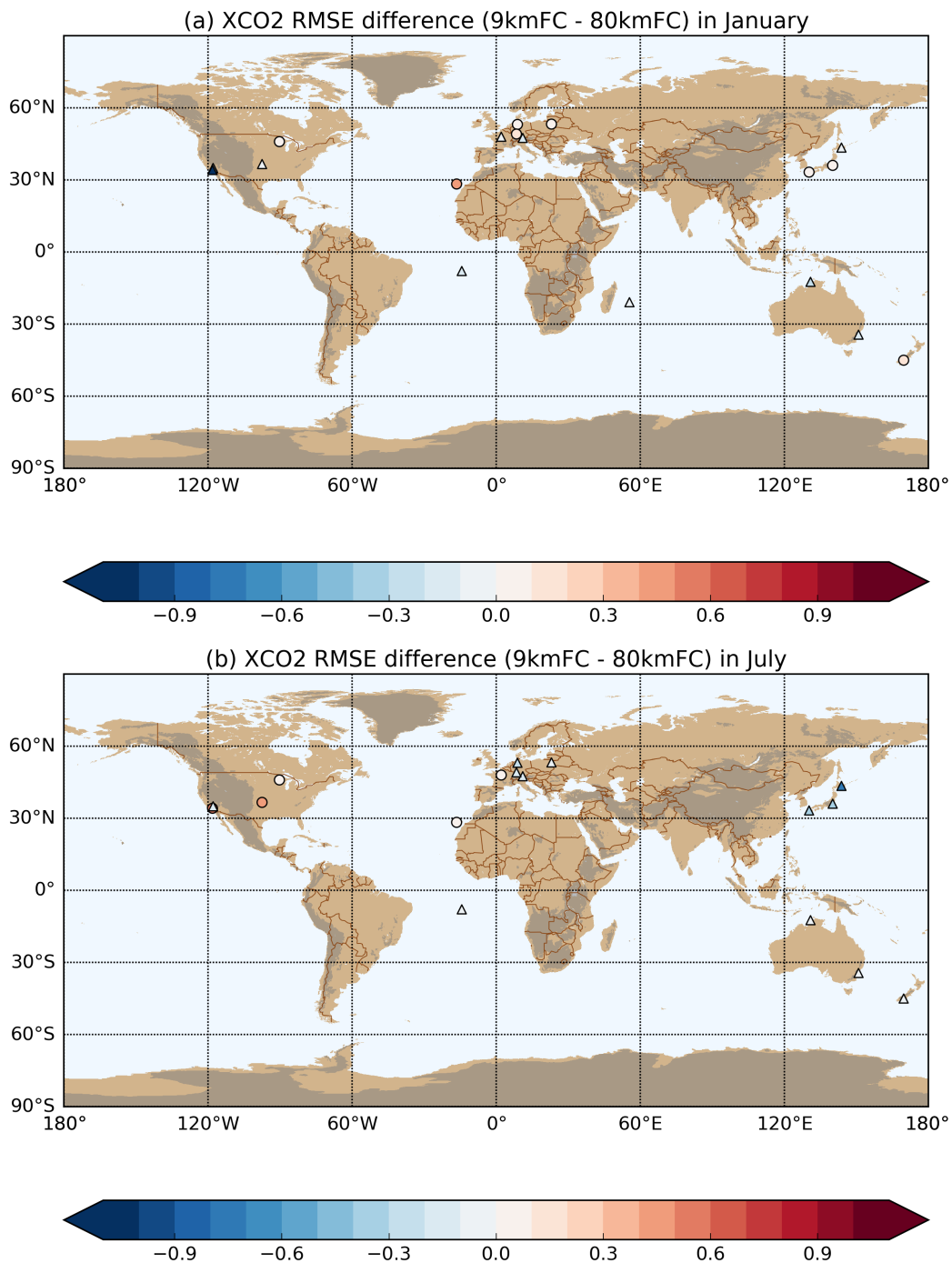


**Figure S9.** Difference in XCO<sub>2</sub> RMSE [ppm] between highest and lowest resolution simulations (9km-EXP – 80km-EXP) in (a) January and (b) July at TCCON stations. Mountain regions with elevation > 1000 m above sea level are shaded in grey. The statistics for each station are listed Tabs S3 and S4 for January and July respectively.

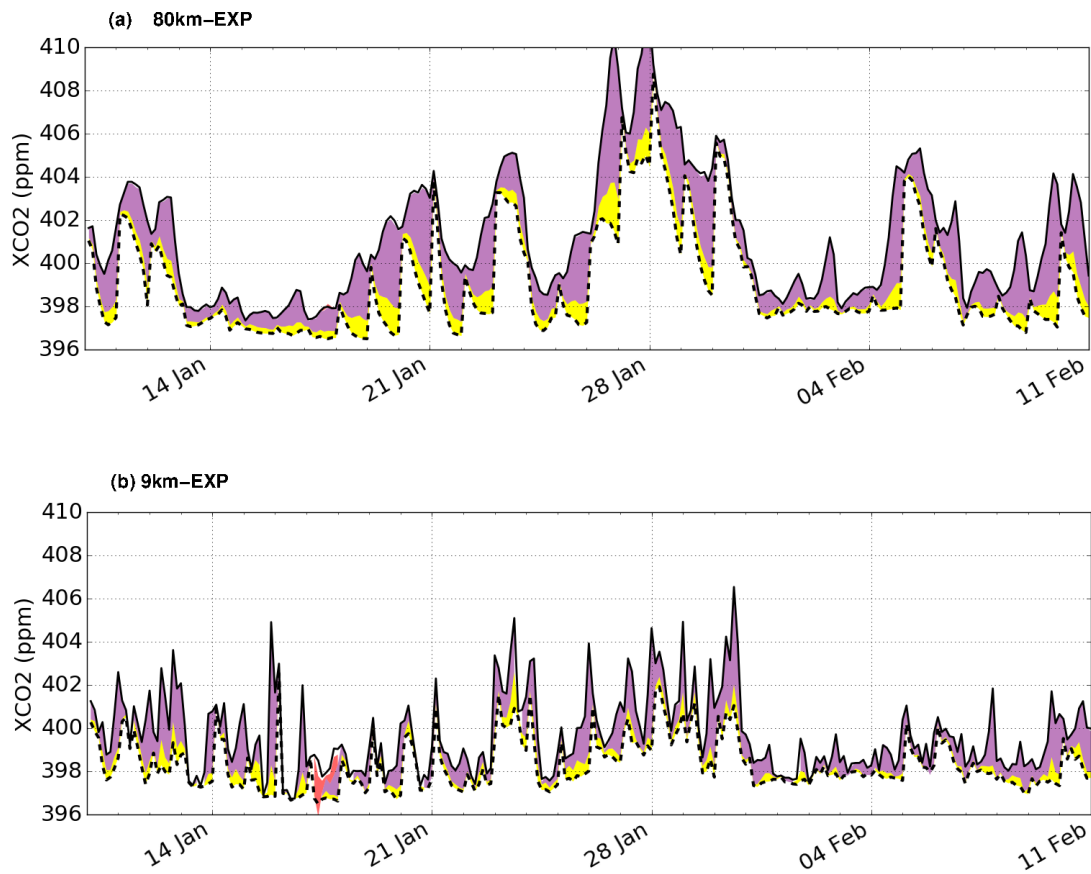


**Figure S10.** Modelled XCO<sub>2</sub> [ppm] from (a) 80km-EXP and (b) 9km-EXP simulations at the TCCON site of Pasadena (Tab.A3) responding to atmospheric transport and fluxes (solid line) and to only atmospheric transport (dash line). The XCO<sub>2</sub> enhancement associated with the different fluxes is coloured in purple (for anthropogenic emissions), yellow (for biogenic emissions) and red (for fires).

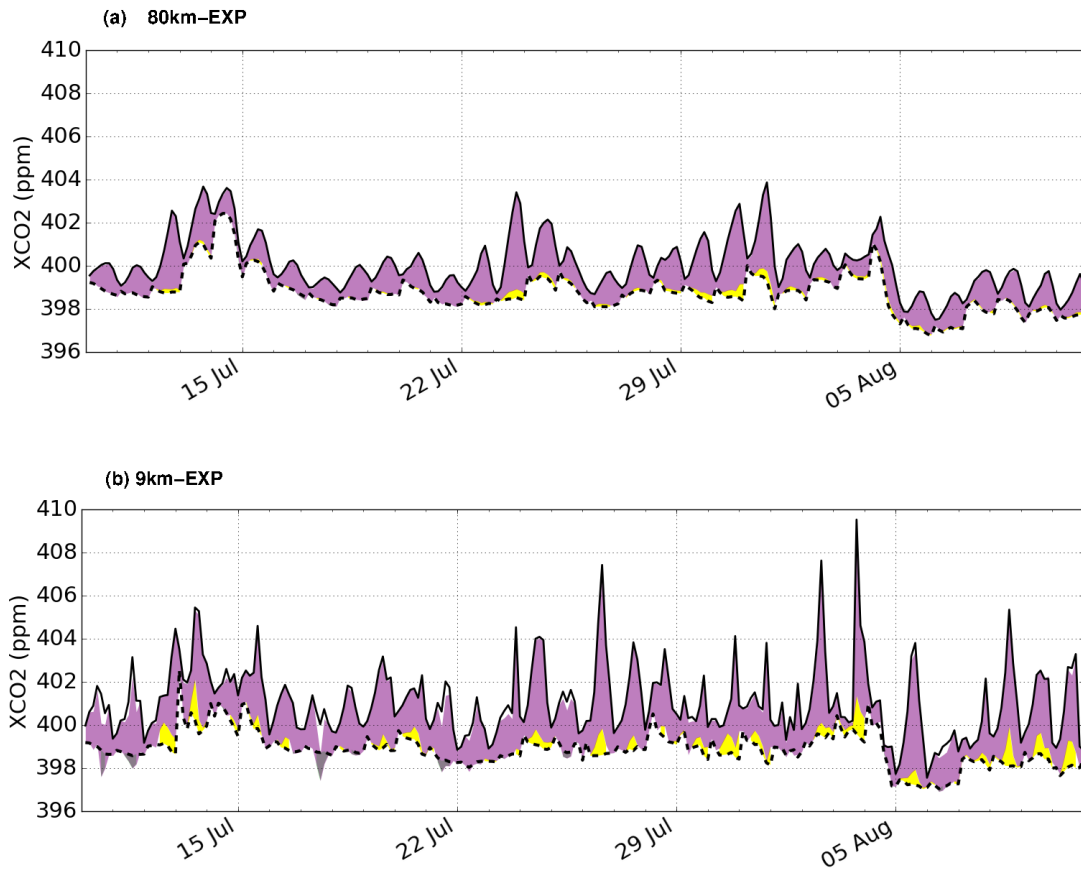
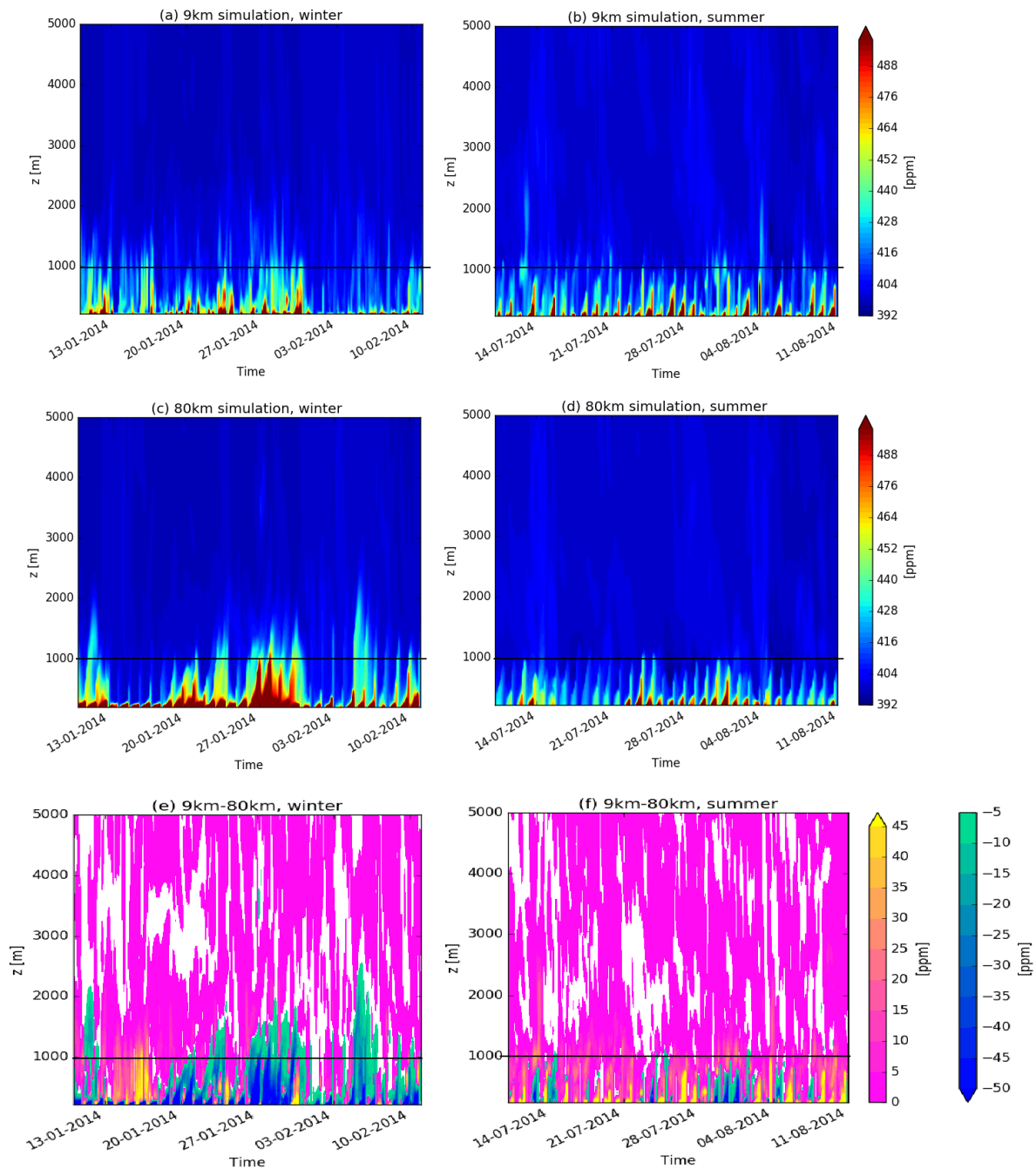


Figure S11. Same as Fig. ?? in July.



**Figure S12.** Modelled atmospheric CO<sub>2</sub> profile [ppm] showing 137 model levels at Pasadena from the 9-km resolution simulation and the 80-km resolution simulation. The horizontal black line shows the level approximately corresponding to 1000 m above the surface. In winter, the high CO<sub>2</sub> values are trapped below 1000 m in the boundary layer, except for certain synoptic episodes where boundary layer is ventilated as seen by high values (larger than 420 ppm) crossing the 1000 m line. While in summer the sea breeze circulation ventilates the boundary layer on a daily basis.

Table S1: January statistics of atmospheric CO<sub>2</sub> [ppm] from 9km-EXP and 80km-EXP simulations with respect to continuous in situ stations (surface and tower). The differences between the two simulations (9km-EXP – 80km-EXP) are shown in the last three columns. The location and reference of each station can be found in Tab. A1.

Station	Bias	Bias	STDE	STDE	RMSE	RMSE	N	$\Delta$ STDE	$\Delta$  Bias	$\Delta$ RMSE
	9kmEXP	80kmEXP	9kmEXP	80kmEXP	9kmEXP	80kmEXP				
alt	-2.14	-2.09	0.61	0.61	2.23	2.18	679	0.05	0.00	0.05
brw	-1.45	-1.55	1.19	1.14	1.88	1.92	727	-0.10	0.05	-0.04
cby	-1.51	-1.30	0.58	0.56	1.62	1.42	298	0.21	0.02	0.2
inu	0.50	0.36	2.04	2.45	2.11	2.47	702	0.14	-0.41	-0.36
pal-nonlocal	-0.89	0.32	2.13	3.44	2.31	3.46	595	0.57	-1.31	-1.15
bck	0.93	1.21	1.45	1.37	1.73	1.83	768	-0.28	0.08	-0.1
chl	0.50	0.68	1.70	1.91	1.77	2.02	465	0.18	-0.21	-0.25
llb	-1.77	-1.59	3.19	3.32	3.65	3.69	699	0.18	-0.13	-0.04
etl	-0.67	-0.17	1.53	1.71	1.68	1.72	695	0.5	-0.17	-0.04
mhd	-1.11	2.34	4.75	1.03	1.52	5.30	759	-1.23	3.72	-3.78
wao	-0.68	-0.01	3.24	3.26	3.31	3.26	92	0.67	-0.02	0.05
ces-200magl	-2.39	-1.27	4.41	4.71	5.02	4.88	679	1.12	-0.30	0.14
est	-1.20	-1.08	2.09	1.93	2.41	2.21	762	0.12	0.16	0.2
fsd	-0.73	-0.40	1.24	1.29	1.44	1.35	768	0.33	-0.05	0.09
cps	-0.58	0.06	1.32	1.49	1.44	1.49	697	0.52	-0.17	-0.05
esp	1.01	4.43	3.71	4.93	3.84	6.62	753	-3.42	-1.22	-2.78
kas	0.67	8.45	4.39	6.57	4.44	10.71	503	-7.78	-2.18	-6.27
ssl	3.21	18.72	4.87	15.00	5.83	23.99	739	-15.51	-10.13	-18.16
hun-115magl	-6.58	-2.68	5.52	5.64	8.59	6.24	751	3.90	-0.12	2.35
jfj	0.08	12.47	2.53	9.29	2.53	15.55	720	-12.39	-6.76	-13.02
lef-396magl	-0.78	-0.49	1.47	1.51	1.67	1.59	765	0.29	-0.04	0.08
puy	2.39	6.11	3.91	8.29	4.58	10.30	752	-3.72	-4.38	-5.72
amt-107magl	0.01	-0.50	2.68	2.77	2.68	2.81	741	-0.49	-0.09	-0.13
egb	-1.13	-1.66	5.14	5.33	5.26	5.58	726	-0.53	-0.19	-0.32
wsa	-1.24	-0.82	1.22	1.43	1.74	1.65	766	0.38	-0.21	0.09
vac	-0.13	1.82	1.10	1.82	1.10	2.28	161	-1.69	-0.72	-1.82
tpd	-0.01	0.81	3.11	3.20	3.11	3.30	768	-0.8	-0.09	-0.19

Continued on next page

**Table S1 – continued from previous page**

Station	Bias		STDE		RMSE		N	$\Delta$ STDE	$\Delta$  Bias	$\Delta$ RMSE
	9kmEXP	80kmEXP	9kmEXP	80kmEXP	9kmEXP	80kmEXP				
dec	11.13	7.43	11.42	7.31	15.95	10.42	588	3.70	4.11	5.53
hdp	1.48	16.83	2.73	10.25	3.10	19.71	668	-15.35	-7.52	-16.61
spl	2.28	2.72	3.23	3.50	3.95	4.43	682	-0.44	-0.27	-0.48
gic	-1.88	1.69	5.28	4.43	5.60	4.74	765	0.19	0.85	0.86
nwr	0.76	1.56	1.45	3.40	1.64	3.74	730	-0.80	-1.95	-2.1
bao-300magl	0.34	-2.20	9.43	8.19	9.43	8.48	760	-1.86	1.24	0.95
ryo	3.05	3.88	4.99	6.05	5.84	7.19	432	-0.83	-1.06	-1.35
snp-17magl	3.05	9.66	3.97	10.87	5.01	14.54	768	-6.61	-6.90	-9.53
wgc-483magl	-0.58	-0.60	4.92	5.71	4.95	5.74	768	-0.02	-0.79	-0.79
sgc	1.31	10.31	5.61	9.62	5.76	14.10	652	-9.00	-4.01	-8.34
sct-305magl	-0.13	0.42	3.61	3.83	3.62	3.85	762	-0.29	-0.22	-0.23
wkt-457magl	0.06	0.22	2.34	2.38	2.34	2.39	733	-0.16	0.04	-0.05
izo	0.01	0.63	2.80	0.98	2.80	1.16	722	-0.62	1.82	1.64
yon	-0.40	-0.62	1.22	1.43	1.28	1.56	579	-0.22	-0.21	-0.28
mnm	-0.34	-0.25	0.77	0.71	0.84	0.76	680	0.09	0.06	0.08
mlo	-0.35	0.68	0.78	1.05	0.85	1.25	736	-0.33	-0.27	-0.4
smo	-1.10	-0.81	0.93	0.97	1.44	1.26	683	0.29	-0.04	0.18
cpt-marine	-1.11	1.86	0.60	6.02	1.26	6.30	618	-0.75	-5.42	-5.04
ams	-1.20	-1.27	0.26	0.27	1.22	1.30	116	-0.07	-0.01	-0.08
cgo	-0.69	-1.39	2.46	4.25	2.56	4.47	768	-0.70	-1.79	-1.91
mqa	-1.11	-1.26	0.65	0.66	1.29	1.43	618	-0.15	-0.01	-0.14
cya	-1.14	-1.14	0.36	0.36	1.19	1.19	693	0.00	0.00	0.00
syo	-1.09	-1.15	0.14	0.15	1.10	1.16	32	-0.06	-0.01	-0.06
spo	-1.10	-1.10	0.18	0.19	1.12	1.12	736	0.00	-0.01	0.00

Table S2: July statistics of atmospheric CO<sub>2</sub> [ppm] from 9km-EXP and 80km-EXP simulations with respect to continuous in situ stations (surface and tower). The differences between the two simulations (9km-EXP – 80km-EXP) are shown in the last three columns. The location and reference of each station can be found in Tab. A1.

Station	Bias	Bias	STDE	STDE	RMSE	RMSE	N	$\Delta$ STDE	$\Delta$  Bias	$\Delta$ RMSE
	9kmEXP	80kmEXP	9kmEXP	80kmEXP	9kmEXP	80kmEXP				
alt	-0.93	-1.36	1.05	1.17	1.40	1.80	623	-0.43	-0.12	-0.4
brw	-0.85	-0.68	2.06	2.20	2.23	2.31	738	0.17	-0.14	-0.08
cby	-0.67	-1.83	3.07	3.50	3.15	3.95	754	-1.16	-0.43	-0.8
inu	-1.40	-2.54	3.98	5.07	4.22	5.67	765	-1.14	-1.09	-1.45
pal-nonlocal	2.03	4.40	6.13	10.86	6.45	11.72	345	-2.37	-4.73	-5.27
bck	10.36	34.84	38.58	79.33	39.95	86.65	757	-24.48	-40.75	-46.7
chl	-0.09	-0.77	4.45	4.61	4.45	4.67	768	-0.68	-0.16	-0.22
llb	-10.09	-7.88	14.30	13.39	17.50	15.53	352	2.21	0.91	1.97
etl	-3.59	-4.90	7.02	7.48	7.88	8.94	549	-1.31	-0.46	-1.06
mhd	-2.27	-0.40	5.63	6.52	6.07	6.53	703	1.87	-0.89	-0.46
wao	-4.01	-3.44	8.33	7.12	9.24	7.91	568	0.57	1.21	1.33
ces-200magl	-3.49	-2.93	7.76	7.97	8.51	8.50	668	0.56	-0.21	0.01
est	0.35	0.50	8.62	9.37	8.63	9.38	79	-0.15	-0.75	-0.75
fsd	-3.51	-4.59	8.96	9.23	9.62	10.31	768	-1.08	-0.27	-0.69
cps	-2.98	-3.85	7.03	7.52	7.64	8.45	760	-0.87	-0.49	-0.81
esp	0.28	-6.53	5.69	10.09	5.70	12.01	318	-6.25	-4.40	-6.31
kas	-1.01	7.42	4.17	15.93	4.29	17.57	558	-6.41	-11.76	-13.28
ssl	-0.11	9.63	8.99	18.56	8.99	20.91	761	-9.52	-9.57	-11.92
hun-115magl	-6.61	-5.61	7.87	7.43	10.28	9.32	768	1.0	0.44	0.96
jfj	-5.23	-5.48	3.60	10.60	6.35	11.93	109	-0.25	-7.0	-5.58
lef-396magl	3.88	2.53	6.22	6.05	7.33	6.56	744	1.35	0.17	0.77
puy	0.75	4.88	7.19	12.36	7.23	13.29	752	-4.13	-5.17	-6.06
amt-107magl	2.60	-0.94	8.24	7.95	8.64	8.00	768	1.66	0.29	0.64
egb	-1.24	-6.52	13.31	15.61	13.37	16.92	632	-5.28	-2.30	-3.55
wsa	0.95	0.41	4.66	5.60	4.76	5.62	768	0.54	-0.94	-0.86
vac	2.85	6.98	5.22	12.04	5.95	13.91	764	-4.13	-6.82	-7.96
tpd	-1.20	-2.44	14.31	13.12	14.37	13.34	767	-1.24	1.19	1.03

Continued on next page

**Table S2 – continued from previous page**

Station	Bias	Bias	STDE	STDE	RMSE	RMSE	N	$\Delta$ STDE	$\Delta$  Bias	$\Delta$ RMSE
	9kmEXP	80kmEXP	9kmEXP	80kmEXP	9kmEXP	80kmEXP				
dec	7.78	11.01	10.37	11.97	12.96	16.26	619	-3.23	-1.60	-3.3
hdp	4.11	27.16	4.36	25.67	5.99	37.37	551	-23.05	-21.31	-31.38
spl	8.73	20.16	6.34	16.93	10.79	26.32	493	-11.43	-10.59	-15.53
gic	-10.88	-6.14	17.13	14.08	20.30	15.36	147	4.74	3.05	4.94
nwr	3.63	11.03	3.68	15.20	5.17	18.78	399	-7.40	-11.52	-13.61
bao-300magl	1.05	-1.43	5.69	6.55	5.79	6.70	743	-0.38	-0.86	-0.91
ryo	18.51	10.77	27.89	17.28	33.48	20.36	170	7.74	10.61	13.12
snp-17magl	24.15	37.81	16.55	30.11	29.28	48.33	768	-13.66	-13.56	-19.05
wgc-483magl	1.57	1.37	2.75	2.81	3.17	3.13	384	0.20	-0.06	0.04
sgc	5.74	14.61	5.71	12.54	8.09	19.25	719	-8.87	-6.83	-11.16
sct-305magl	3.90	4.21	7.82	7.31	8.73	8.43	767	-0.31	0.51	0.3
wkt-457magl	4.75	4.90	4.32	3.93	6.42	6.28	666	-0.15	0.39	0.14
izo	4.65	-1.84	3.82	2.22	6.01	2.88	746	2.81	1.60	3.13
yon	0.61	0.26	1.98	1.58	2.07	1.60	522	0.35	0.40	0.47
mnm	0.33	0.27	0.98	0.97	1.04	1.00	647	0.06	0.01	0.04
mlo	0.83	-0.52	1.22	1.60	1.47	1.68	612	0.31	-0.38	-0.21
sno	-0.26	-0.34	0.80	0.87	0.84	0.93	695	-0.08	-0.07	-0.09
cpt-36-marine	-0.12	-0.82	0.93	5.91	0.94	5.97	536	-0.7	-4.98	-5.03
ams	-0.90	-1.03	0.28	0.29	0.94	1.07	306	-0.13	-0.01	-0.13
cgo	-0.55	-0.41	1.56	2.42	1.66	2.45	758	0.14	-0.86	-0.79
mqa	-0.84	-0.94	0.40	0.40	0.93	1.02	692	-0.10	0.0	-0.09
cya	-0.95	-1.01	0.29	0.29	0.99	1.05	760	-0.06	0.0	-0.06
syo	-0.92	-0.97	0.14	0.13	0.93	0.98	32	-0.05	0.01	-0.05
spo	-0.83	-0.88	0.16	0.15	0.85	0.89	737	-0.05	0.01	-0.04

Table S3: January statistics of XCO<sub>2</sub> [ppm] from 9km-EXP and 80km-EXP simulations with respect to TCCON stations. The differences between the two simulations (9km-EXP – 80km-EXP) are shown in the last three columns. The location of the station and their associated reference are provided in Tab A3.

Station	Bias	Bias	STDE	STDE	RMSE	RMSE	N	Δ STDE	Δ  Bias	Δ RMSE
	9kmEXP	80kmEXP	9kmEXP	80kmEXP	9kmEXP	80kmEXP	data			
bialystok01	-1.28	-1.20	0.29	0.33	1.32	1.24	15	0.08	-0.04	0.08
bremen01	0.22	0.12	0.73	0.70	0.77	0.71	8	0.10	0.03	-0.06
karlsruhe01	0.11	-0.12	0.69	0.54	0.70	0.55	33	-0.01	0.15	0.15
orleans01	-0.25	-0.26	0.45	0.48	0.52	0.54	67	-0.01	-0.03	-0.02
garmisch01	-0.53	-0.73	0.55	0.60	0.76	0.94	33	-0.20	-0.05	-0.18
parkfalls01	-1.42	-1.38	0.37	0.36	1.46	1.42	28	0.04	0.01	0.04
rikubetsu01	-1.74	-1.74	0.14	0.17	1.74	1.75	21	0.00	-0.03	-0.01
lamont01	-0.98	-1.03	0.64	0.66	1.17	1.22	129	-0.05	-0.02	-0.05
tsukuba02	0.37	0.36	1.02	0.97	1.08	1.03	111	0.01	0.05	0.05
edwards01	0.42	0.05	0.47	0.64	0.63	0.65	191	0.35	-0.17	-0.02
pasadena01	0.32	2.03	1.24	2.68	1.28	3.36	160	-1.71	-1.44	-2.08
saga01	-1.30	-1.36	0.78	0.64	1.52	1.50	30	-0.06	0.14	0.02
izana01	-0.85	-0.36	0.39	0.29	0.93	0.46	18	0.49	0.10	0.47
ascension01	0.69	0.89	0.71	0.72	0.99	1.15	153	-0.20	-0.01	-0.16
darwin01	-1.04	-1.17	0.49	0.76	1.15	1.39	34	-0.13	-0.27	-0.24
reunion01	-0.10	0.01	0.34	0.36	0.35	0.36	150	0.09	-0.02	-0.01
wollongong01	-0.45	-0.19	0.63	0.89	0.78	0.91	157	0.26	-0.26	-0.13
lauder02	-1.00	-0.77	0.55	0.56	1.14	0.95	104	0.23	-0.01	0.19

Table S4: July statistics of XCO<sub>2</sub> [ppm] from 9km-EXP and 80km-EXP simulations with respect to TCCON stations. The differences between the two simulations (9km-EXP – 80km-EXP) are shown in the last three columns. The location of the station and their associated DOI are provided in Tab A3.

Station	Bias	Bias	STDE	STDE	RMSE	RMSE	N	$\Delta$ STDE	$\Delta$  Bias	$\Delta$ RMSE
	9kmEXP	80kmEXP	9kmEXP	80kmEXP	9kmEXP	80kmEXP				
bialystok01	0.97	1.01	1.06	1.17	1.44	1.54	68	-0.04	-0.11	-0.1
bremen01	1.18	1.36	0.67	0.77	1.36	1.57	44	-0.18	-0.10	-0.21
karlsruhe01	1.25	1.44	0.77	0.81	1.47	1.65	90	-0.19	-0.04	-0.18
orleans01	1.38	1.36	0.66	0.66	1.53	1.51	16	0.02	0.00	0.02
garmisch01	0.92	1.03	0.66	0.74	1.14	1.27	90	-0.11	-0.08	-0.13
parkfalls01	0.56	0.49	1.09	1.07	1.23	1.18	168	0.07	0.02	0.05
rikubetsu01	2.21	2.92	0.55	0.64	2.27	2.99	9	-0.71	-0.09	-0.72
lamont01	2.00	1.48	1.32	1.25	2.40	1.94	299	0.52	0.07	0.46
tsukuba02	1.21	1.52	0.95	1.06	1.54	1.85	120	-0.31	-0.11	-0.31
edwards01	1.28	1.40	0.76	0.79	1.49	1.61	316	-0.12	-0.03	-0.12
pasadena01	1.23	0.57	1.30	1.09	1.79	1.23	302	0.66	0.21	0.56
saga01	0.80	1.20	0.57	0.66	0.98	1.37	30	-0.40	-0.09	-0.39
izana01	0.45	0.11	0.36	0.49	0.58	0.50	43	0.34	-0.13	0.08
ascension01	0.08	0.18	0.45	0.47	0.46	0.51	158	-0.10	-0.02	-0.05
darwin01	1.54	1.55	0.33	0.35	1.58	1.59	264	-0.01	-0.02	-0.01
reunion01	0.81	0.79	0.33	0.36	0.87	0.87	136	0.02	-0.03	0.0
wollongong01	0.23	0.22	0.64	0.69	0.68	0.73	96	0.01	-0.05	-0.05
lauder02	0.10	0.11	0.27	0.31	0.29	0.33	86	-0.01	-0.04	-0.04